UNIVERSITY OF TEXAS AT ARLINGTON

DOCTORAL THESIS

Boundaries and Currents of the Dayside Magnetosphere: MHD Simulations and Observations

---

Author:

Pauline M. DREDGER

Supervisor:

Dr. Ramon E. LOPEZ

A thesis submitted in fulfillment of the requirements

for the degree of Doctor of Philosphy in Physics and Applied Physics

in the

Department of Physics

May 1, 2023

Declaration of Authorship

I, Pauline M. DREDGER, declare that this thesis titled, "Boundaries and Currents of the Dayside Magnetosphere: MHD Simulations and Observations" and the work presented in it are my own. I confirm that:

- This work was done wholly or mainly while in candidature for a research degree at this University.
- Where any part of this thesis has previously been submitted for a degree or any other qualification at this University or any other institution, this has been clearly stated.
- Where I have consulted the published work of others, this is always clearly attributed.
- Where I have quoted from the work of others, the source is always given. With the exception of such quotations, this thesis is entirely my own work.
- I have acknowledged all main sources of help.
- Where the thesis is based on work done by myself jointly with others, I have made clear exactly what was done by others and what I have contributed myself.

Signed:

_____

Date:

_____

UNIVERSITY OF TEXAS AT ARLINGTON

Abstract

Department of Physics

Doctor of Philosphy in Physics and Applied Physics

Boundaries and Currents of the Dayside Magnetosphere: MHD Simulations and Observations

by Pauline M. DREDGER

The solar wind streams through space at supersonic speeds, carrying plasma and the interplanetary magnetic field (IMF) from the sun. Earth's magnetosphere presents a magnetosonic obstacle to the solar wind flow, which slows down suddenly, creating a bow shock. Between the bow shock and Earth's magnetic field is the region of space called the magnetosheath, which contains the dense plasma and turbulent IMF of the shocked solar wind. The magnetopause is the boundary between the magnetosheath and the region of near-Earth space dominated by the terrestrial magnetic field; its location is determined by the competing pressures of the plasma in the magnetosheath and the magnetic pressure from inside the magnetosphere. Magnetopause position thus varies with the incoming solar wind conditions, which can affect the pressure from both regions. Because of the different magnetic field strengths and orientations on either side of both the bow shock and the magnetopause, the resulting magnetic shears give rise to currents on both boundaries, called the bow shock current and the magnetopause current.

The location of the magnetopause is important from a space weather perspective, since satellites can find themselves in either the magnetosphere or the magnetosheath as the magnetopause moves in response to the changing solar wind. To predict magnetopause motion, satellite operators often use one of several physics-based numerical models. We present our investigation of the abilities of four magnetohydrodynamic (MHD) models to accurately predict magnetopause location, comparing simulation results to spacecraft data. We find that two of the models tend to overpredict magnetopause motion, while the other

two tend to underpredict, to a greater or lesser degree. We also find that, overall, the models do better when magnetopause motion is driven primarily by a plasma density increase in the magnetopause. Finally, we compare the performance of two of the models when coupled to an inner magnetosphere model, which includes the physics describing the toroidal current flowing around the earth called the ring current. The ring current, which is prominent during geomagnetic storms, affects the location of the magnetopause both directly, by an outward pressure, and indirectly, by its connection to currents flowing on magnetic field lines into the ionosphere.

Several currents in the magnetosphere close on the Chapman-Ferraro current, including the ionospheric field-aligned currents and the bow shock current. We present a case study investigating the relationship of these three current systems, using observations from both the magnetosphere and the ionosphere as well as an MHD simulation of the event. We find that, under certain solar wind conditions, a significant fraction of the bow shock current may close directly into the ionosphere on open field lines, bypassing the magnetopause current.

Acknowledgements

We acknowledge the support of the US National Science Foundation (NSF) under grant 1916604. We also acknowledge the support of the National Aeronautics and Space Administration (NASA) under grants 80NSSC19K1670 and 80NSSC20K0606 (The Center for the Unified Study of Interhemispheric Asymmetries (CUSIA)). M. Hamrin was supported by the Swedish National Space Agency and the Swedish Research Council.

Simulation results have been provided by the Community Coordinated Modeling Center at Goddard Space Flight Center through their public Runs on Request system (http://ccmc.gsfc.nasa.gov). The LFM Model was developed by John Lyon et al. at Dartmouth College/NCAR-HAO/JHU-APL/CISM. OpenGGCM was developed by Joachim Raeder and Timothy Fuller-Rowell at the Space Science Center, University of New Hampshire. GUMICS was developed by Pekka Janhunnen et al. at the Finnish Meteorological Institute. This work was carried out using the SWMF and BATS-R-US tools developed at the University of Michigan's Center for Space Environment Modeling (CSEM). The modeling tools described in this publication are available online through the University of Michigan for download and are available for use at the Community Coordinated Modeling Center (CCMC).

GOES data were provided by NOAA (https://satdat.ngdc.noaa.gov/).

OMNI (Papitashvili & King, 2020) and THEMIS data were provided at CDAWeb (NASA CDAWeb Development Team, 2019). We acknowledge NASA contract NAS5-02099 and V. Angelopoulos for use of data from the THEMIS Mission, specifically: K. H. Glassmeier, U. Auster and W. Baumjohann for the use of FGM

data provided under the lead of the Technical University of Braunschweig and with financial support through the German Ministry for Economy and Technology and the German Center for Aviation and Space (DLR) under contract 50 OC 0302; C. W. Carlson and J. P. McFadden for use of ESA data.

Orbit plots were provided by SSCWeb (https://sscweb.gsfc.nasa.gov/cgi-bin/Locator_graphics.cgi).

We thank the AMPERE team and the AMPERE Science Center for providing the Iridium derived data products (http://ampere.jhuapl.edu/).

The DMSP SSJ/4 particle detectors were designed by Dave Hardy of AFRL. Those data and the plots that show the data were obtained from JHU/APL at http://sd-www.jhuapl.edu/Aurora/spectrogram/. The DMSP plasma drift and magnetometer data were obtained from http://cedar.openmadrigal.org.

We thank the MMS Science Data Center and the MMS teams, especially the magnetic field and the ion teams, for producing high quality data. We also acknowledge NASA's National Space Science Data Center and Space Physics Data Facility. MMS data are available at https://lasp.colorado.edu/mms/sdc/public/.

We thank Dr. Patricia Doherty for conversations concerning the DMSP plasma drift and magnetometer data. We also thank Dr. Kevin Pham for assistance in running the LFM model.

Throughout my academic career, I have been fortunate to have strong support from my family, friends and colleagues. I must first of all thank two high school teachers, without whom I probably would not have set off down the

path of a physics degree; these are Shannon (Timmons) Awerkamp, my Algebra 1 teacher, and Aimee Maddeford, from whom I learned high school chemistry. These two classes taught me that I liked math and that I was interested in physics, since chemistry was really based on particle physics. Next I would like to thank all of my undergraduate professors at Saint Mary's College and Kansas State University, as well as the many good friends I made at both institutions. In particular, I am grateful to Dr. Debra Dandaneau, my academic advisor, and Dr. Eleanor Sayre, who encouraged me to apply to REU programs. Through these REUs I learned how to conduct research and grew as a person, meeting more friends along the way. The next thanks, therefore, go to my REU advisors, especially Dr. Brianna Mount (Black Hills State University) and Dr. Frederick Wilder (at the time CU Boulder LASP, now UTA). Through my time working with Rick, I discovered the field of magnetospheric physics and decided to choose a graduate program in which I could continue studying space physics.

In graduate school, I am very grateful to my professors who supported me academically and to all the mentors who helped me in my research and gave me career advice. Special mention goes to my NASA mentor, Dr. Yaireska Collado-Vega, my Newkirk Fellowship mentors at HAO, Dr. Kevin Pham and Dr. William Lotko, and my coauthor Dr. Maria Hamrin. I must also thank my classmates Nicholas Byrnes and Benjamin Smithers for their friendship over the years, as well as the many other grad students in the physics department whom I count among my friends. In particular I must express my gratitude to my group members Dr. Fatima Bagheri, Dr. Elizabeth Vandegriff, Dr. Christian Bagby-Wright, Dr. Tre'Shunda James, Espen Frederick, and Rushikesh Patil. Outside

UTA, I have also been fortunate enough to have good friends and colleagues, especially Dr. Agnit Mukhopadhyay, who has been a close friend and peer mentor since early in my graduate years. My committee members were chosen not simply because they were the space physics faculty at UTA but because they have all been mentors to me in some capacity, for which I am immensely grateful: Dr. Daniel Welling, Dr. Frederick Wilder, Dr. Benjamin Jones, and Dr. Yue Deng. The biggest thanks of all must of course go to my Ph.D. advisor Dr. Ramon Lopez, who has been a tremendous support to me in terms of research as well as personally. I really would not have made it through grad school without such an outstanding mentor.

Finally, I have relied heavily on my support network from back home in Kansas, especially during the COVID years. I would like to mention in particular Dr. Emilie (Jordan) Jackson and Steve Jackson, my roommate and roommate-in-law, Isabella Childs, my St. Mary's friend away from St. Mary's, and my childhood best friends Bernadette Maddeford and Christianna Tamburelli, who have literally been there since the beginning of my academic career in first grade. My family members have always supported me, especially my grandparents Diane and Raymond Engell and my uncle and godfather Dr. John Dredger. My siblings have always been there for me: Ellen, Mary, Julianna, Catherine, Bridget, James, Susan, and Anne. I am especially grateful to Ellen for visiting me frequently in my time in Texas and Colorado. Lastly, I must express my deepest love and gratitude for my parents, William and Jeanine Dredger, for raising me, supporting me, educating me, and giving me the life that I have. God has truly given me a family on which I can rely in any circumstance, in any place.

Contents

List of Figures

List of Tables

Dedicated to my father and my uncle, William and John Dredger, my academic heroes.

Chapter 1

Introduction

1.1 Coordinate Systems

This study primarily uses the geocentric solar ecliptic (GSE) coordinate system. In GSE coordinates, X points along the Earth-sun line and Z is perpendicular to the ecliptic plane, where positive Z points northward. Y completes the right-handed coordinate system, with positive Y in the duskward direction. The units of GSE coordinates are Earth radii, or R_E. R_E is the most commonly used unit of length in magnetospheric physics because of the enormous distances over which the relevant phenomena occur.

1.2 The Solar Wind

The solar system is full of plasma and magnetic field expanding outward from the sun, which together make up the solar wind. The magnetic field of the solar wind, called the interplanetary magnetic field (IMF), is simply the solar magnetic field; any magnetic field lines observed in the solar wind are connected on

either end to the sun. The solar wind flow varies both spatially and temporally: spatially, depending on the location on the sun from which it originated, and temporally, because the sun is highly dynamic. The sun is also rotating with a period of 24 days at its equator, creating a sort of "lawn sprinkler" effect with the sun being the sprinkler and the solar wind being the ejected water. This rotation, which generates the so-called "Parker spiral," (named after Eugene Parker, who initially suggested it) contributes to both the spatial and the temporal variations. Plasma parameters, such as density and bulk velocity, and IMF strength and orientation can thus vary drastically from hour to hour and from location to location, as the solar wind travels throughout the solar system (e.g. Parker, 1965; Parker, 1958).

The solar wind plasma is a quasi-neutral, electrically conducting fluid, which means that, although it contains particles of positive or negative charge, for distances greater than the Debye length the charges cancel out. The fluid approximation is valid because, throughout most of the solar system, the solar wind plasma is collisionless and any resistive effects can be ignored (e.g. Hundhausen, 1968). The plasma and IMF travel together because of the frozen-in flux theorem, which states that, in the limit of a large magnetic Reynolds number, the magnetic topology of an electrically conducting fluid is preserved. The magnetic Reynolds number is large when the velocity and length scales are large compared to the magnetic diffusivity and induction dominates over diffusion. Where the conditions for the frozen-in flux theorem are no longer met, reconnection of magnetic field lines can occur. During reconnection, two magnetic field lines with anti-parallel components break from their original configuration and

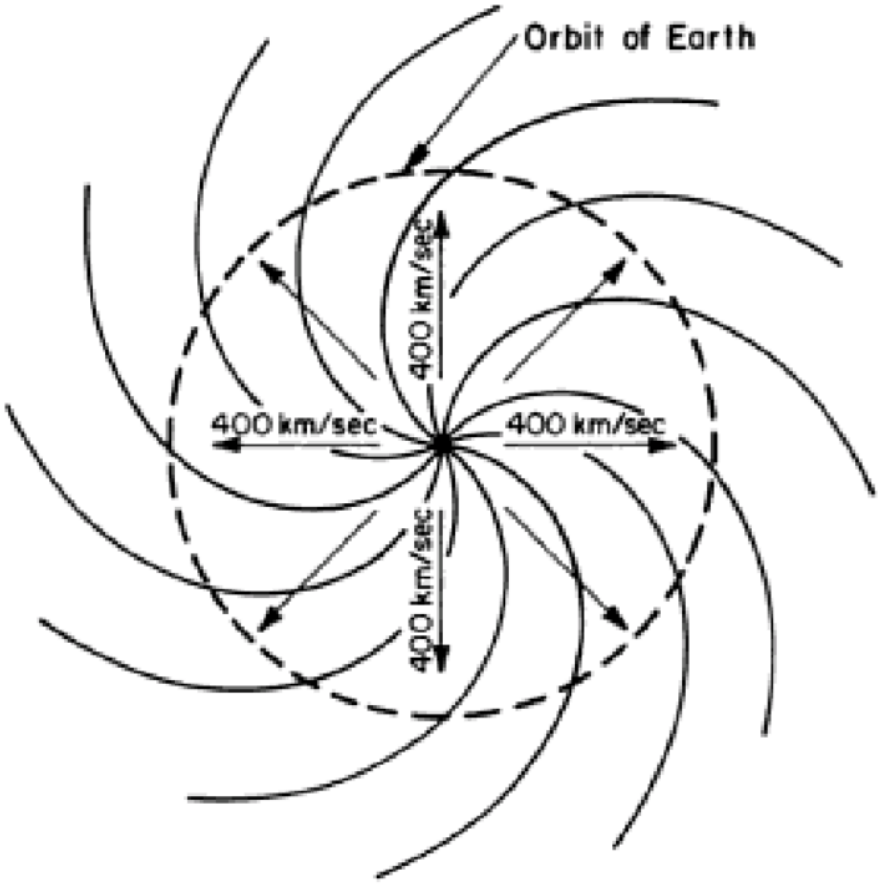

FIGURE 1.1: The Parker spiral, which results from the rotation of the sun. The curved lines represent magnetic field lines. (Plot from Kivelson and Russell (1995))

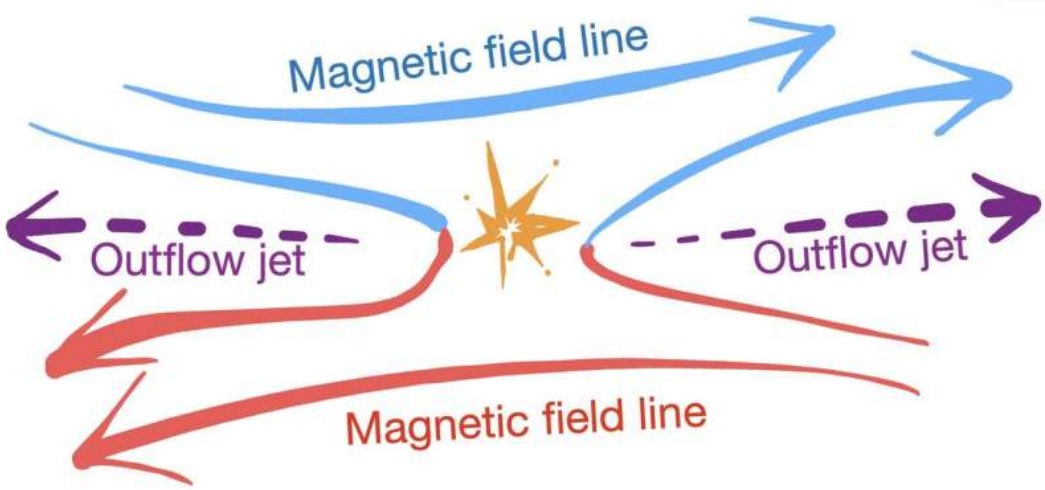

FIGURE 1.2: A cartoon of the process of magnetic reconnection. (Image credit: Yi-Hsin Liu/Dartmouth College)

form two new field lines of different orientations. The process of reconnection converts energy stored in the magnetic field into kinetic energy of the associated plasma, creating outflow jets. Without this process, the energy in the magnetic field must build up to infinity, since it cannot be released if the topology of the field lines is conserved. Magnetic reconnection therefore plays a crucial role in the transfer of energy and the topology of Earth's magnetosphere (e.g. Kivelson & Russell, 1995).

Space plasmas like those of the solar wind are governed by the physics of magnetohydrodynamics (MHD), a combination of fluid dynamics and electromagnetism. MHD and magnetic reconnection are treated more mathematically in Section 1.9.

The solar wind is the primary driver of space weather at Earth. Consequently, continuous solar wind observations are vital both for operational space weather predictions and for research purposes. Several spacecraft monitor solar

wind conditions in orbit around the first Lagrange point (L1) of Earth and the sun, roughly one million miles upstream of Earth in the solar wind flow. Spacecraft orbiting L1 are generally considered close enough to the Earth-Sun line that their observations represent, to a great degree, the solar wind conditions that impact the magnetosphere. Other solar wind observations are periodically available from Earth-orbiting satellites whose trajectories carry them out of the magnetosphere near apogee. These observations are superior to the L1 observations in the sense that they are closer to Earth, but they are not continuous like those at L1.

1.3 The Bow Shock and the Magnetosheath

As the solar wind travels away from the sun, it moves at supersonic speeds (e.g. Parker, 1965). Supersonic here means at a speed greater than that of the fast mode of a magnetoacoustic wave, a type of linear magnetohydrodynamic wave. Because the plasma and IMF are moving faster than the speed of information, a bow shock is formed in space when the solar wind meets a magnetosonic obstacle, such as Earth's magnetic field. Earth's bow shock is therefore the first boundary through which the incoming solar wind passes on its way to interacting with the magnetosphere (e.g. Kivelson & Russell, 1995).

The physics of the bow shock is governed by the Rankine-Hugoniot equations for MHD, which use conservation of mass, momentum, and energy across the shock to calculate the downstream state from the upstream state as a function of the magnetosonic Mach number M_{ms}. The magnetosonic Mach number is

the ratio of the plasma flow velocity and the magnetosonic velocity. When M_{ms} is high, downstream of the shock the plasma pressure dominates the pressure from the magnetic field, and when M_{ms} is low the magnetic pressure dominates over the plasma pressure (e.g. Lopez et al., 2010).

The bow shock's shape and location vary depending on solar wind conditions, particularly the direction of the solar wind flow, the density of the plasma, and the strength of the IMF. On average, the front part of the bow shock is located at around 15 Earth radii away from the center of the earth. Downstream of Earth, the bow shock disappears as it becomes parallel to the solar wind flow (e.g. Kivelson & Russell, 1995; Spreiter et al., 1966).

The compression of the IMF across the shock is associated with a curl of the magnetic field $\vec{B}$, and therefore, by Ampere's law, an electric current flows on the shock. Ampere's law can be stated in the following manner:

$$\nabla \times \vec{B} = \mu_0 \vec{J} \tag{1.1}$$

This bow shock current is always present, regardless of solar wind conditions, although its direction is dictated by the IMF orientation, as seen in Equation 1.1. The closure of this current is not well-understood, although it has implications for energy transfer throughout the magnetosphere (Lopez, 2018). The bow shock current exerts a $\vec{J} \times \vec{B}$ force against the incoming flow, extracting solar wind mechanical energy and transferring it to the magnetic field. For any IMF direction, the $\vec{J} \times \vec{B}$ force always points outward into the solar wind, so that the bow shock current is always a dynamo or generator current. A current is called a dynamo

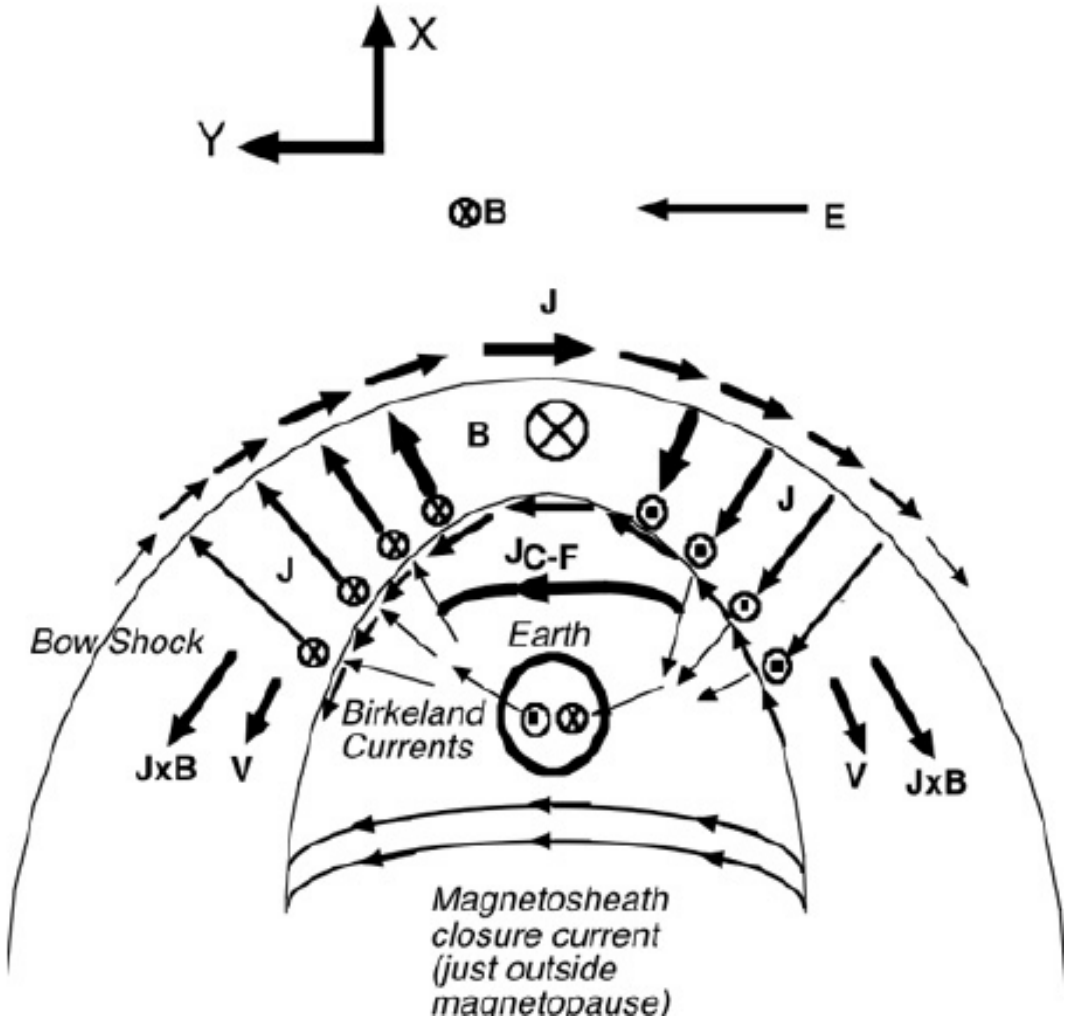

FIGURE 1.3: Bow shock current in relation to other current systems in the magnetosphere, for southward IMF conditions. For descriptions of the magnetopause, the Birkeland currents, and the Chapman-Ferraro currents see Sections 1.5 and 1.7. (Plot from Lopez et al. (2011))

current if $\vec{J} \cdot \vec{E} < 0$, where $\vec{E}$ is the electric field, and a load has $\vec{J} \cdot \vec{E} > 0$. The bow shock current is always oriented in such a way relative to the electric field that $\vec{J} \cdot \vec{E} < 0$ (Lopez et al., 2011).

The solar wind plasma is also compressed across the shock, creating a pressure gradient force that does work against the solar wind. This gradient force extracts mechanical energy from the flow and converts it to thermal energy. As discussed by Lopez et al. (2010), when the magnetosonic Mach number is high, the pressure gradient force dominates and solar wind energy at the shock is primarily converted to thermal energy; on the other hand, when M_{ms} is low, the $\vec{J} \times \vec{B}$ force dominates, and the energy extracted from the solar wind flow is dominated by magnetic energy downstream of the shock.

The compression of the solar wind plasma and IMF across the bow shock creates a region called the magnetosheath. In this region, the shocked solar wind is turbulent, containing many transient phenomena such as fast flows and plasma bubbles. The plasma is much denser and the compressed IMF much stronger than out in the solar wind flow.

Certain Earth-orbiting satellites regularly pass through the magnetosheath and cross the bow shock. An example of a bow shock crossing is shown in Figures 1.4 and 1.5 which contain plasma and magnetic field measurements, respectively. The spacecraft crosses from the magnetosheath into the solar wind at 21:22:00 UT and back again right after 21:26:30 UT, as shown by the sharp discontinuities in all measured parameters. The ion density and pressure, shown in the top and middle panels of Figure A, are significantly higher when the spacecraft is in the magnetosheath than in the solar wind. The plasma velocity in the

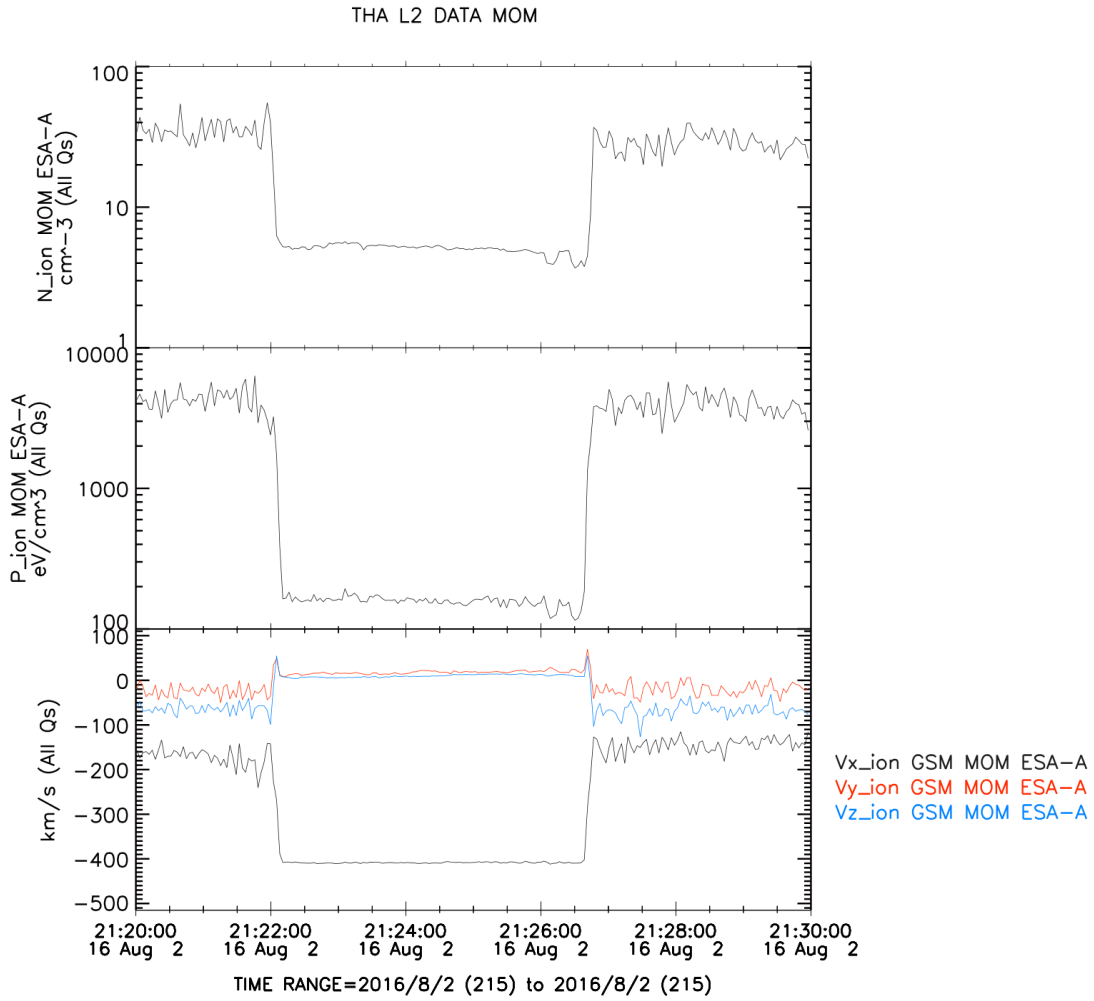

FIGURE 1.4: THEMIS A onboard moment data, showing two bow shock crossings. From the top are shown the ion density, the ion pressure, and the three GSE components of the ion velocity. (Plot from CDAWeb)

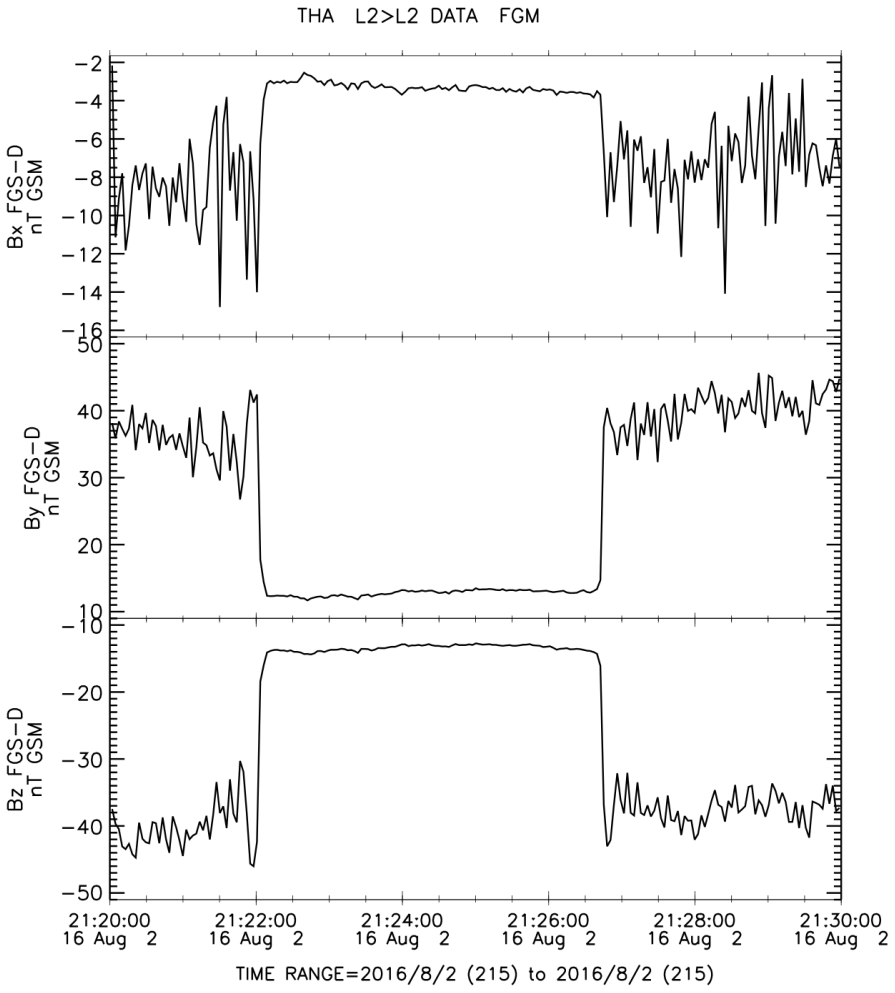

FIGURE 1.5: THEMIS A FGM data, showing two bow shock crossings. From the top are shown the X, Y, and Z components in GSE coordinates of the magnetic field. (Plot from CDAWeb)

solar wind is about 400 km/s in the X direction, while the magnetosheath velocity is at least half as slow. All of the solar wind plasma parameters shown in Figure A are typical values for geomagnetically quiet periods. The magnetic field observations in Figure B show the compression of the IMF across the shock, with stronger magnetosheath values in all three components of $\vec{B}$ than the unshocked IMF in the solar wind, which is moderately strong. The strength and direction of the bow shock current can be calculated using Ampere's law from the measurement of the change in magnetic field.

In both plasma and magnetic field measurements, the values of all parameters vary rapidly in the magnetosheath, as a result of the turbulent nature of the shocked solar wind flow. The rapid variation of the magnetic field creates localized currents throughout the magnetosheath; whether or not these currents have any large-scale structure as a function of solar wind conditions is a topic of ongoing research.

1.4 Solar Wind-Magnetosphere Energy Transfer and the Structure of the Magnetosphere

Earth's magnetic field is approximately a dipole, although higher order moments of the field exist and are primarily important close to Earth's surface. The interaction of Earth's magnetic field with the solar wind, however, changes the shape of the magnetosphere from that of a dipole field into a comet-like shape. The nightside region of the magnetosphere is accordingly referred to as the magnetotail. The process by which the solar wind, in particular the IMF, reshapes

the magnetosphere is called the Dungey cyle, after the man who first proposed the mechanism (see Figure 1.6).

The slowed solar wind plasma and IMF pass through the magnetosheath and eventually reach the outer boundary of the magnetosphere, the magnetopause. Here the IMF encounters Earth's magnetic field, which points northward at the equator. If the incoming IMF has a component that is antiparallel to the dipole field, magnetic reconnection can occur here on the dayside: a field line from the IMF and a dipole field line reconnect to form two "open" field lines, each with one footpoint that connects to Earth. The term "open field line," commonly used to refer to this configuration, does not, of course, mean that the field line is truly open, which would require the existence of magnetic monopoles and the violation of Gauss's law for magnetic fields, written in its differential form as

$$\nabla \cdot \vec{B} = 0 \tag{1.2}$$

where $\vec{B}$ is the magnetic field. Rather, the newly reconnected field lines connect back to the sun, the origin of the IMF. Because part of each open field line reaches out through the magnetosheath past the bow shock, these field lines move in the direction of the solar wind flow and into the magnetotail, where they begin to pile up. The open field lines in the tail from the northern hemisphere are oriented in the opposite direction from the field lines in the southern hemisphere; where the two orientations meet, the resulting curl of the magnetic field forms a cross-tail current flowing dawn to dusk. Eventually, an open field line connected to one hemisphere can meet an oppositely directed field line connected

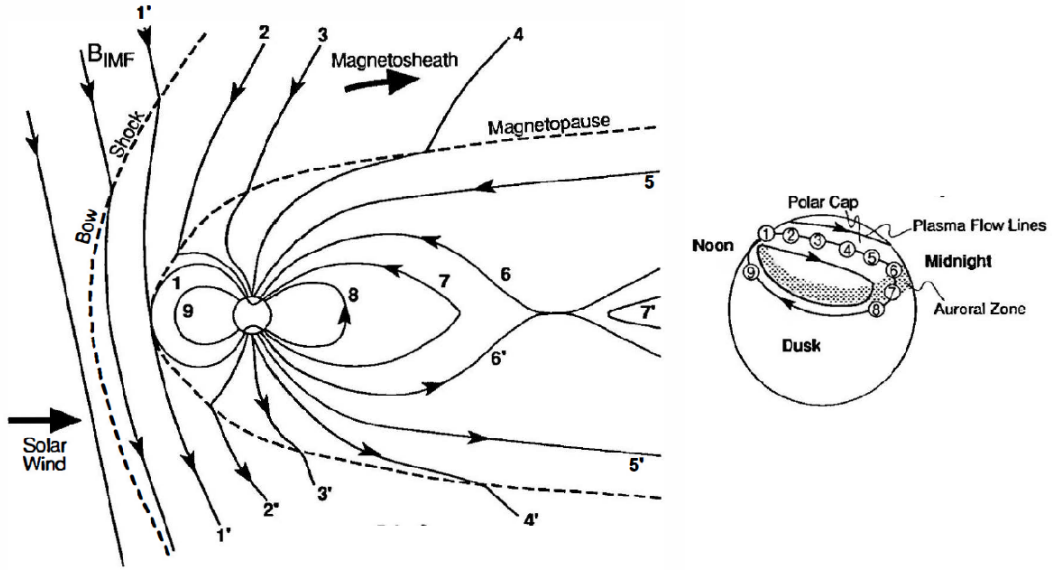

FIGURE 1.6: The Dungey cycle for southward IMF, in the magnetosphere on the left and in the polar ionosphere on the right. The numbers represent a progression in time. (Plot from Hughes (1995))

to the other hemisphere and reconnect once again, forming a "closed" field line, connected at both footpoints to Earth, and a new IMF line that continues down the magnetotail. The new closed field line moves back inward towards Earth, carrying with it the solar wind plasma that was traveling with the original IMF line. This plasma acts as an incompressible fluid and therefore must eventually flow back around to the dayside, dragging the associated field line with it and completing the cycle (Dungey, 1961).

As newly opened field lines are dragged from the dayside to the nightside, their footpoints in the polar cap also move tailward, carrying with them their associated ionospheric plasma. These resulting plasma flows combine with the return flow at lower latitudes described above, which are associated with the

closed field lines moving sunward from the tail, and form a dawn-dusk (east-west) symmetric two-cell plasma convection pattern. The lower latitude boundary of the pattern is called the convection reversal boundary, since an instrument inside the pattern would measure an opposite plasma velocity to the plasma outside. This boundary is often used as a proxy for the boundary between open and closed field lines, since the two boundaries roughly coincide (Dungey, 1961).

The rate of energy transfer from the solar wind to the magnetosphere is primarily governed by dayside reconnection. This process is most efficient when the IMF has a strong southward component, but solar wind energy is still transferred to the magnetosphere-ionosphere system when the IMF points northward, or has a positive IMF B_z component. In such a case, the IMF cannot reconnect with dipole field lines on the dayside magnetopause and the solar wind field lines drape over the front of the magnetosphere onto the nightside. Here reconnection can occur because the draped IMF lines are antiparallel to the dipole field lines as they point into the northern and out of the southern polar cap. Northward IMF reconnection creates more complicated magnetic topologies than southward IMF reconnection, such as open field lines draped around the dayside or open field lines in the tail that stretch across the equator into the opposite hemisphere from their footpoint. The ionospheric convection pattern generated by northward reconnection is similarly complex, with four cells instead of two, as the various types of field lines are dragged across the polar cap with their associated plasma (Bhattarai et al., 2012; Crooker, 1992; Li et al., 2005; Song et al., 2000).

The secondary mechanism that transfers energy from the solar wind to the

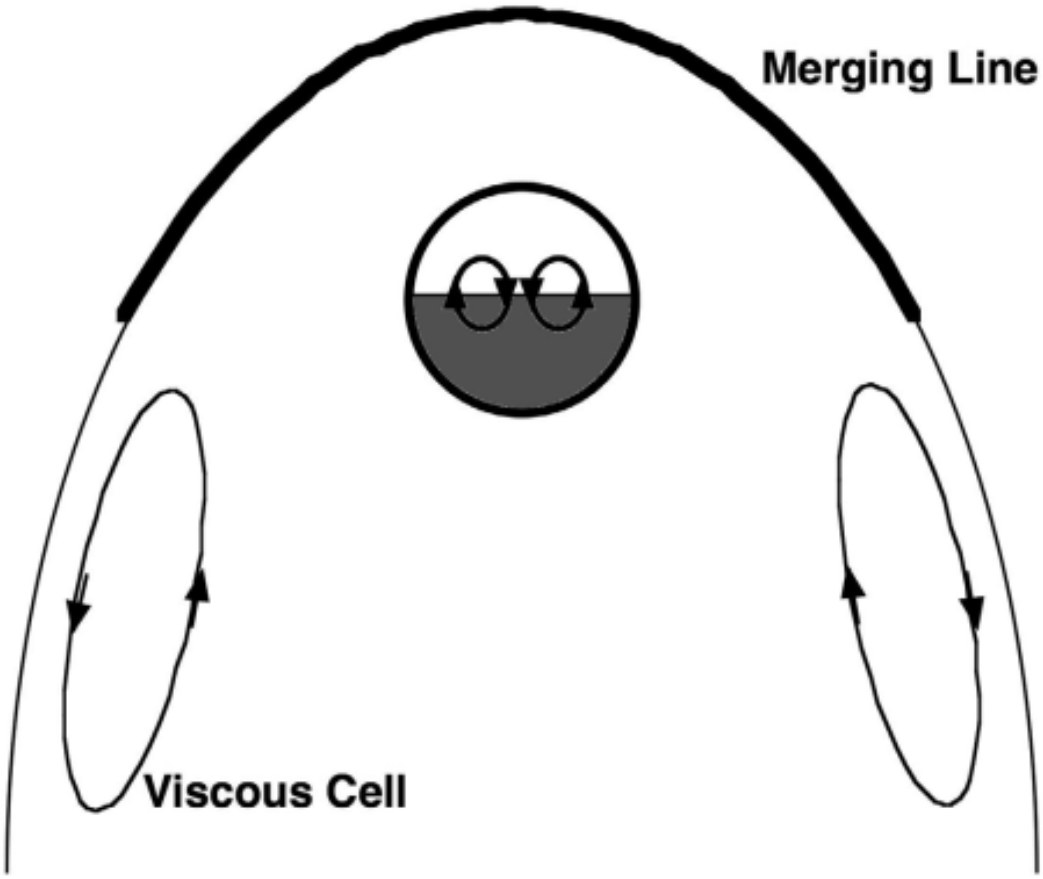

FIGURE 1.7: The circulation of plasma due to the viscous interaction, as well as the ionospheric plasma circulation for southward IMF, looking down on one of the poles with the sun at the top of the plot. (Plot from Lopez et al. (2010))

magnetosphere is called the viscous interaction. The viscous interaction is the process by which the mechanical transfer of momentum across the magnetopause from the solar wind flow entrains plasma on closed dipole field lines. This entrainment drags the plasma antisunward in parallel with the solar wind flow for a while, before it returns sunward further inside the magnetosphere (see Figure 1.7). The viscous convection cell plasma flows in the opposite sense to the two-cell convection pattern set up by southward reconnection, as described above (Axford & Hines, 1961). The viscous interaction is much less important than dayside reconnection but is present regardless of IMF orientation (e.g. Lopez et al., 2010, and references therein).

Solar wind plasma can only enter the magnetosphere on open field lines. The region of open field lines above the polar cap in each hemisphere is called the cusp. The overall shape and plasma properties of the cusp regions change with IMF strength and orientation, both of which determine the rate at which magnetic field lines are reconnected (Smith & Lockwood, 1996).

1.5 The Magnetopause

The magnetopause, the boundary between the magnetosphere and the shocked solar wind in the magnetosheath and the location of dayside reconnection, separates two regions of very different plasma and magnetic field conditions. In general, the magnetosheath is turbulent, with dense plasma and magnetic field that vary with the arrival of the solar wind, while inside the magnetosphere

Earth's magnetic field dominates and plasma densities are much lower. The balance of plasma pressure from the magnetosheath and magnetic pressure from the terrestrial magnetic field determines, in the most basic approximation, the instantaneous location of the magnetopause, which varies with the two pressures (Martyn, 1951). High solar wind dynamic pressure in the magnetosheath will force the boundary inward towards Earth from the outside. On the other hand, a strong southward IMF component will strengthen current systems inside the magnetosphere, i.e. the Region 1 field-aligned currents (described in Section 1.7) and the nightside cross-tail current. Increasing the strength of these currents creates fringe fields opposite to Earth's magnetic field and thus weakens it, which reduces the outward magnetic pressure from the inside and allows the magnetopause to move closer to Earth (Maltsev et al., 1996; Maltsev & Lyatsky, 1975; Sibeck et al., 1991; Wiltberger et al., 2003). During quiet time, the "nose" of the magnetopause is located at around 8 R_E in front of Earth, but during geomagnetic storms it can move in as far as geosynchronous orbit (6.6 R_E) or less.

Just as at the bow shock, the change in the magnetic field across the magnetopause, from shocked IMF to dipole field, gives rise to a current density, called the Chapman-Ferraro or magnetopause current. At low latitudes the current flows from dawn to dusk, while at higher latitudes the current reverses, based on the magnetic shear. The low-latitude current is a load, since it passes through the dayside reconnection region, and has been shown to connect to the bow shock dynamo (Siebert & Siscoe, 2002). The high-latitude magnetopause current, conversely, is a dynamo current under normal conditions. When M_{ms}

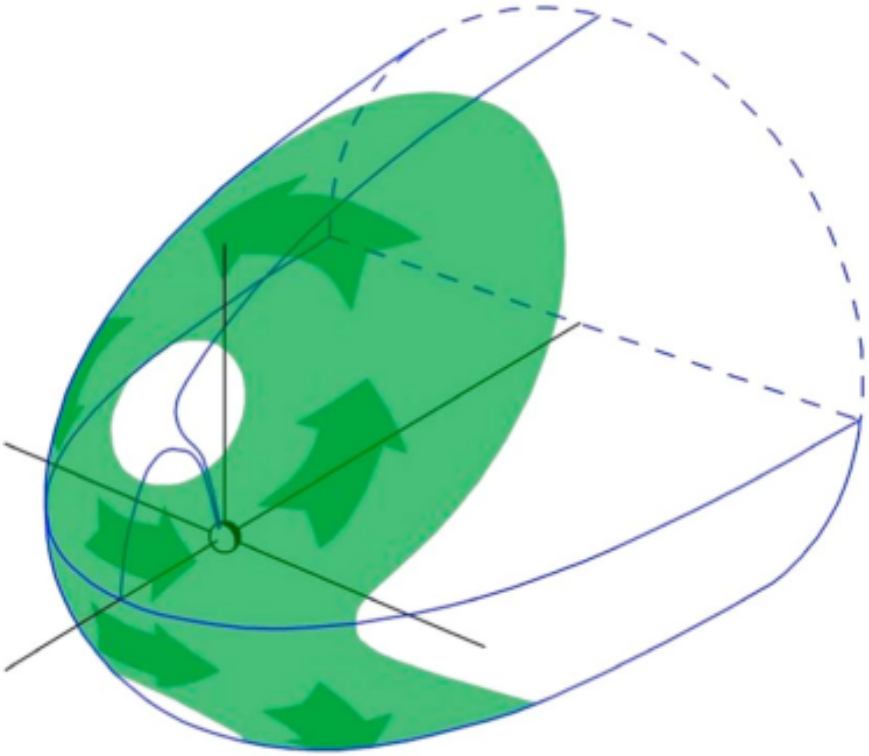

FIGURE 1.8: The Chapman-Ferraro current flowing on the magnetopause. The sun is at the lower left. (Plot from Ganushkina et al. (2018))

is high, the high latitude dynamo disappears, leaving the bow shock current as the primary generator in the system (Lopez et al., 2011).

The Chapman-Ferraro current flows on either side of the boundary, with an interior and an exterior portion. If the solar wind was not present outside the magnetosphere, the Chapman-Ferraro current would still exist, since magnetic field measurements would have to go to zero as the spacecraft instrument left the magnetosphere. The interior current, or "traditional" Chapman-Ferraro current, is due to the rotation of the magnetic field from dipole field values to zero (for a negative IMF B_z component), while the exterior current is caused by the change from zero to the shocked IMF values (Vasyliūnas, 2011). The interior and exterior currents are associated with $\vec{J} \times \vec{B}$ forces in the outward and inward directions, respectively. For typical solar wind conditions, when the solar wind magnetosonic Mach number is high, the outward force dominates and is the primary force standing off the solar wind from the magnetosphere (Lopez & Gonzalez, 2017).

Observations from an example crossing of the magnetopause by a spacecraft are shown in Figures C and D. Figure C contains the proton density and pressure, which decrease rapidly at 11:41:50 UT from high magnetosheath values to the characteristic low density and pressure of the magnetosphere just inside the boundary. The magnetic field observations in Figure D have the magnetopause crossing time marked by a vertical red line. During a period of southward IMF, such as the one shown in Figures C and D, the Z component of the magnetic field observed by the spacecraft can be used to identify the time of crossing. Because Earth's magnetic field always points northward, any measurements of

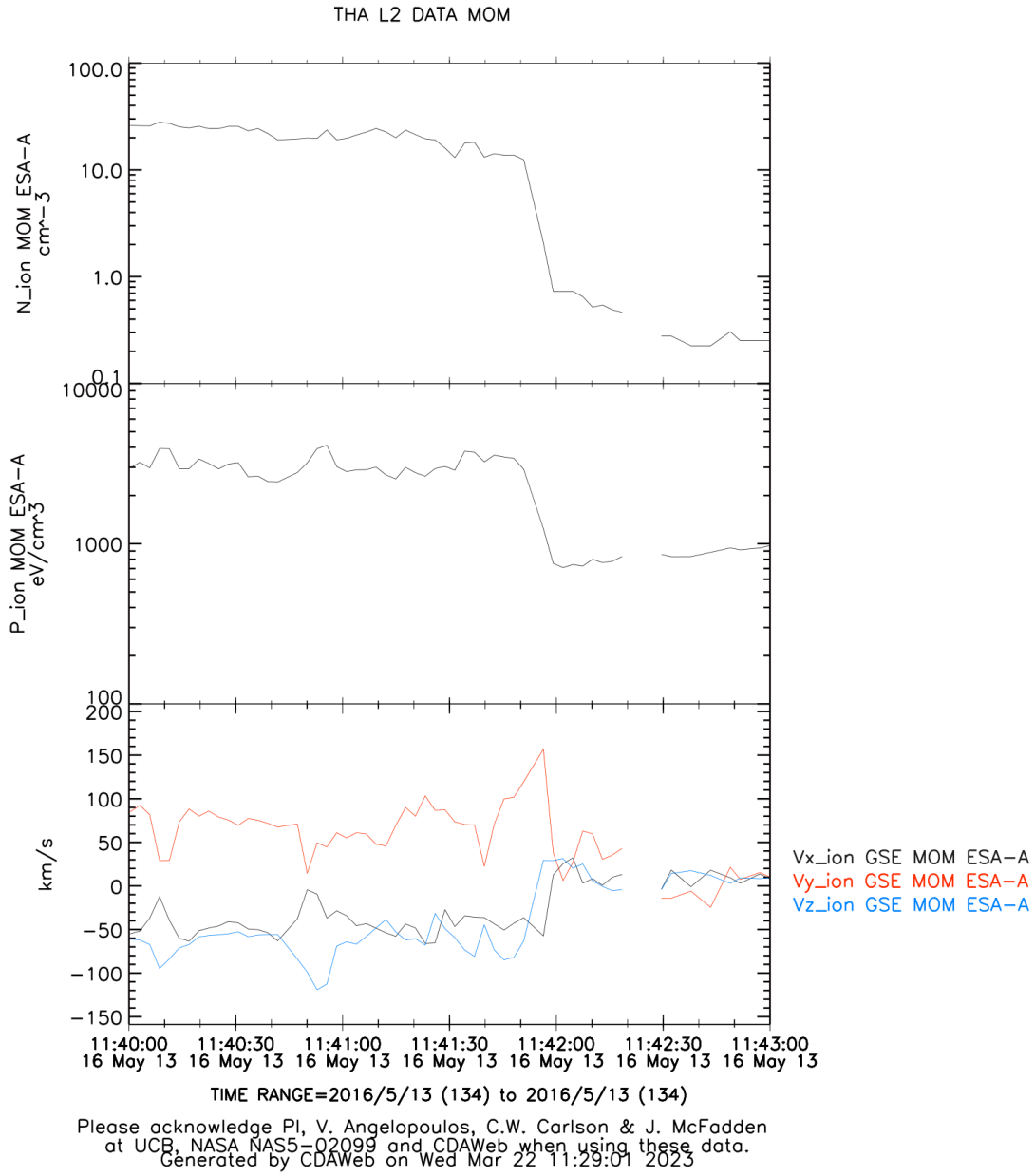

FIGURE 1.9: THEMIS A onboard moment data, showing a magnetopause crossing. The spacecraft is in the magnetosheath on the left of the plot and in the magnetosphere on the right. From the top are shown the ion density, the ion pressure, and the three GSE components of the ion velocity. (Plot from CDAWeb)

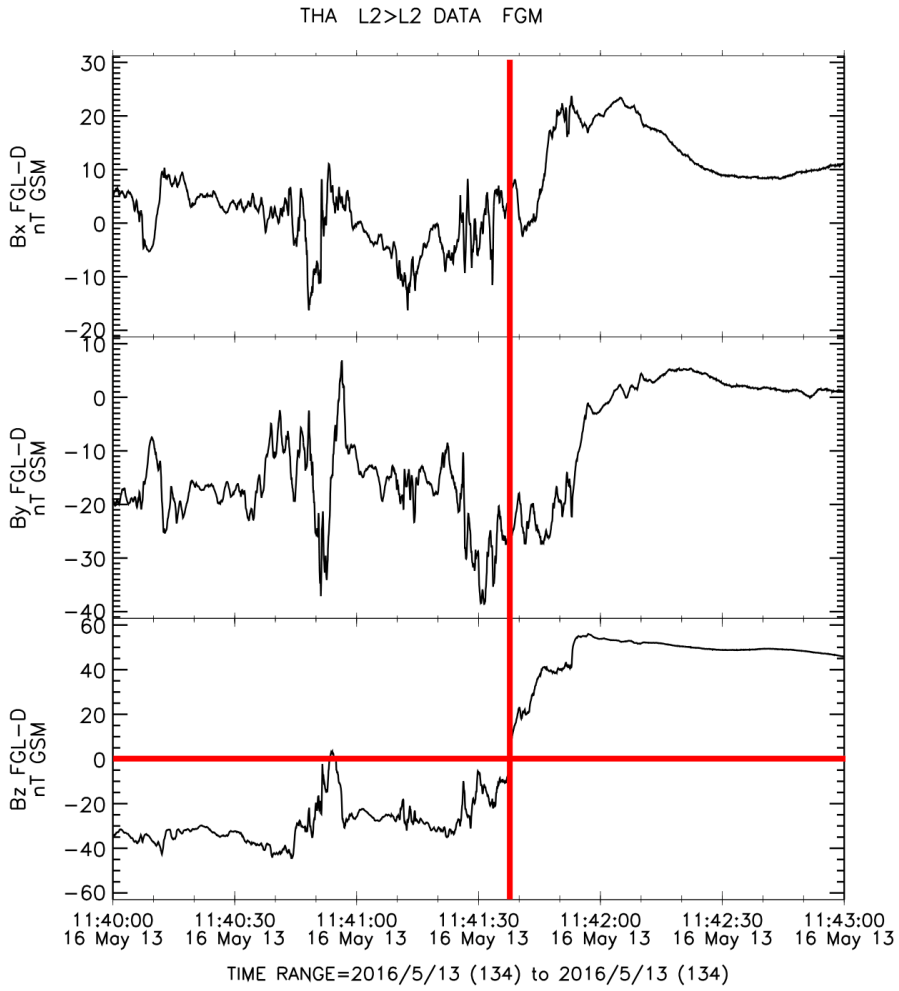

FIGURE 1.10: THEMIS A FGM data, showing a magnetopause crossing. The spacecraft is in the magnetosheath on the left of the plot and in the magnetosphere on the right. From the top are shown the X, Y, and Z components in GSE coordinates of the magnetic field. (Plot from CDAWeb)

southward B_z must be shocked IMF in the magnetosheath and the location of $B_z = 0$ is a good proxy for the magnetopause location. In the example here shown, the spacecraft crosses the boundary just before 11:41:40 UT, meaning that the change in the plasma parameters happens inside the magnetosphere. The rotation of the magnetic field shows the structure of the Chapman-Ferraro current during this period. From about 11:40:50 UT until the crossing time, the only magnetic field component showing a consistent rotation from the turbulent magnetosheath values to 0 nT is B_z. After the crossing, all three components rotate up to values consistent with a dipole field, which at this location has a B_x and a B_z component. The particular magnetic field components that rotate on either side of the boundary determine the directions of the interior and exterior Chapman-Ferraro current, according to Ampere's law.

1.6 The Inner Magnetosphere: The Ring Current During Storms

Closer to Earth is the region called the inner magnetosphere, which has three different plasma populations based on energy. The plasmasphere, an extension of the ionosphere, contains cold plasma with energies of about 1 eV. The radiation belts, whose structure and intensity vary greatly with solar wind conditions, are composed of relativistic ions and electrons, i.e. with energies greater than 500 keV. In the middle of these two energy ranges lies the energetic ring current population, with energies between 1 and 500 keV. The radiation belts and the ring

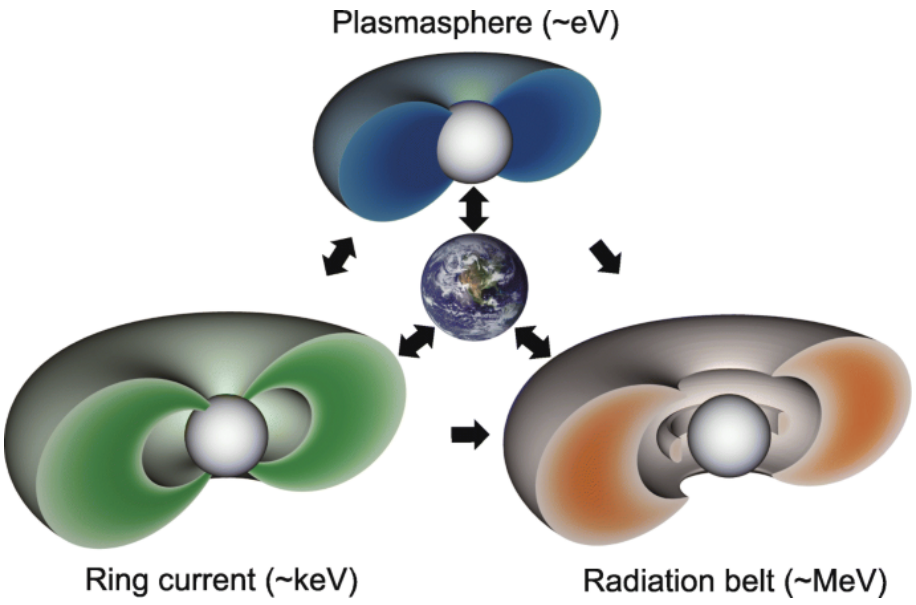

FIGURE 1.11: Inner magnetosphere plasma populations, including the ring current, the radiation belts, and the plasmasphere. (Plot from Ebihara (2019))

current are located generally in the same region of near-Earth space. All three of these plasma populations are highly coupled (Fok, 2020).

The energetic particle population of the inner magnetosphere becomes a current because of a charge-dependent gradient-curvature drift, which causes the energetic plasma particles to move perpendicularly across dipole field lines, electrons eastward and ions westward. The resulting ring current therefore flows around Earth in the equatorial plane. This toroidal current induces a magnetic field opposite to Earth's magnetic field, which can cause measureable weakening of the field at the surface of Earth. The Disturbance Storm Time (Dst) index measures how strongly the ring current affects the surface field and is calculated every hour using four ground magnetometer stations at near-equatorial latitudes (Sugiura, 1963). During quiet time, Dst (with units of nanoTeslas) is

around zero or slightly positive; however, during geomagnetic storms, when the ring current is stronger and causes a greater weakening of the surface field, Dst can reach values of -100 nT or less. Dst and related indices like SYM-H, which is calculated similarly to Dst but every minute instead of every hour, are used to measure the intensity of storms, since such periods are generally characterized by a strengthening of the ring current.

In the closed field line region, a charged particle can gyrate around a magnetic field line and travel from one magnetic footpoint to the other. The angle at which the particle travels with respect to the field line is called the pitch angle. Particles with pitch angles greater than a certain critical value are reflected back along the field line when they approach a magnetic footpoint, while particles with pitch angles smaller than the critical value can escape the bounce motion and precipitate into the ionosphere. The ring current population is also subject to drifts across magnetic field lines caused by electric and magnetic fields, the curvature of magnetic field lines, and plasma pressure gradients (e.g. Kivelson & Russell, 1995).

Although the ring current is always present, it is enhanced during storm time. The source of ring current particles is the plasma sheet, the region of the magnetotail containing recently reconnected field lines that carry plasma of solar wind origin (e.g. Moore et al., 2005). Storms are triggered by periods of strong southward IMF, for which dayside reconnection is most efficient, leading to an increased rate of reconnection in the tail and more plasma in the plasma sheet. More energetic particles are then injected into the inner magnetosphere and become part of the ring current, contributing to its intensity.

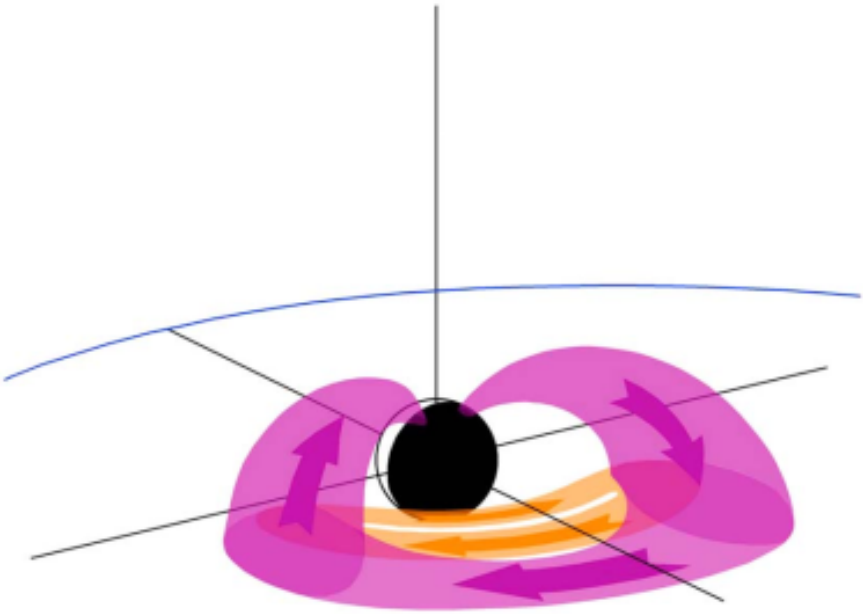

FIGURE 1.12: An example of Region 2 FACs, showing the connection with the ring current. The orange current is called the banana current, a part of the ring current system that is not discussed here. The sun is to the upper left. (Plot from Ganushkina et al. (2018))

The ring current couples to the ionosphere by means of Earth's magnetic field lines, which are lines of constant magnetic potential that pass through the inner magnetosphere to the ionosphere. These field lines are perfect conductors and electric currents can flow along them. Assuming conservation of current, which can be stated mathematically as $\nabla \cdot \vec{J} = 0$, any asymmetries in the ring current give rise to divergence of current out of the equatorial plane and along magnetic field lines. The field-aligned currents (FACs or Birkeland currents) that result from ring current divergence are called the Region 2 currents (e.g. Fok, 2020; Ganushkina et al., 2015, and references therein) (Region 1 currents will be discussed in Section 1.7). Region 2 currents flow into the high latitude ionosphere on the dusk side and out on the dawn side. Because of their connection to the ring current, Region 2 FACs are intensified during storms.

1.7 The Ionosphere

Inside the plasmasphere, within 3 R_E from the center of Earth, lies the ionosphere. The ionosphere and the upper part of the atmosphere (i.e. the thermosphere) are colocated in space but are composed of different populations: the ionosphere refers to charged particles, while the atmosphere refers to the neutrals. The latter population far outnumbers the former and the two are only weakly coupled, so that often the neutrals are ignored for simplicity. There are, however, important atmospheric effects that influence the ionosphere and are the topic of current research.

The ionosphere has vertical layers that vary in particle species and density,

based on the chemical processes that dominate at each altitude range. One of the most important processes that influence the structure of the ionosphere is solar photoionization, by which X-rays and extreme ultraviolet (EUV) rays from the sun ionize neutral atmospheric particles. Along with creation processes like photoionization, there are balancing loss processes, which dominate in the absence of solar radiation, such as recombination of charged particles into neutrals. These processes together give rise to a diurnal variation in ionospheric density for a given longitude and can even create layers that disappear as that part of the ionosphere rotates onto the nightside (e.g. Kivelson & Russell, 1995). There are also seasonal variations in the ionosphere due to the planet's tilt, which changes the amount of sunlight at each pole and hence the amount of localized photoionization.

In the polar regions, the ionosphere couples to the magnetosphere, since it contains the footpoints of magnetospheric field lines. As described in Section 1.4, as open field lines move with the solar wind, their footpoints are dragged across the polar cap, setting up plasma convection patterns in the ionosphere. There are also magnetospheric sources of plasma, such as plasma on open field lines and particles that precipitate into the ionosphere from the inner magnetosphere. The variation in ionization introduced by both internal ionospheric processes and external sources change the localized conductance of the ionosphere, which directly affects the primary coupling between the magnetosphere and the ionosphere, namely, the field-aligned currents (e.g. Kivelson & Russell, 1995).

Section 1.6 above describes the origin of the Region 2 currents, which flow

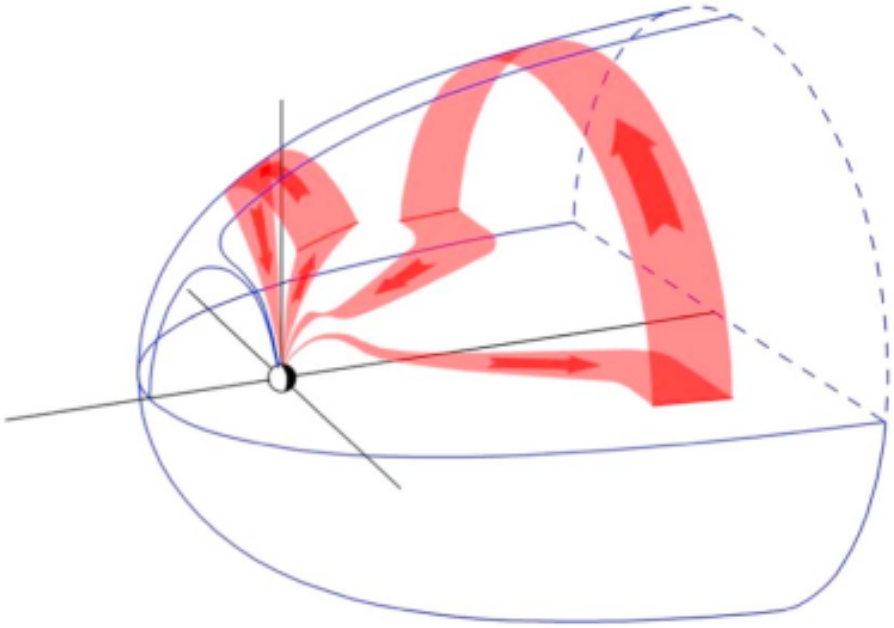

FIGURE 1.13: Region 1 FACs, showing two possible closure paths involving the magnetopause current and the far tail plasma sheet. The sun is to the left. (Plot from Ganushkina et al. (2018))

from the inner magnetosphere along closed field lines. Another type of Birkeland current, the Region 1 (R1) currents, close into the ionosphere at higher latitudes than the Region 2 currents and flow in the opposite sense, i.e. in on the dawn side and out on the dusk side. Unlike Region 2, currents with R1 polarity do not have one clear origin, coupling rather to several different regions of the magnetosphere. Region 1 currents are driven by pressure gradients and velocity shears on both the dayside and the nightside, including but not limited to instabilities in the plasma sheet, the velocity shear across the magnetopause, and divergence of current associated with tubes of magnetic flux in the magnetotail. Both open and closed field lines can be the path of R1 currents. The part of the Region 1 currents that flows on open field lines closes with the dayside magnetopause current, while current driven by other processes flows in on closed field lines and connects to the magnetopause current in the tail (e.g. Ganushkina et al., 2018; Ganushkina et al., 2015, and references therein).

The strength of both R1 and R2 currents depends on ionospheric conductivity and its variations. (N.B. In ionospheric physics, the terms "conductance" and "conductivity" are often used interchangeably.) The polar cap in the summer hemisphere, with its higher rate of photoionization, can carry stronger FACs than the winter hemisphere. The three-dimensional, anisotropic ionospheric conductance can be written as a tensor, adopting the coordinate system where $\hat{z}$ is parallel to the magnetic field, $\hat{x}$ is parallel to the component of the electric field perpendicular to the magnetic field, and $\hat{y}$ completes the right-handed system. The conductance tensor σ can be written $\begin{pmatrix} \sigma_P & -\sigma_H & 0 \\ \sigma_H & \sigma_P & 0 \\ 0 & 0 & \sigma_{||} \end{pmatrix}$, where σ_H and σ_P are the

Hall and Pedersen conductivities, respectively, and $\sigma_{||}$ is the parallel conductivity. The Pedersen conductivity is in the $\hat{x}$ direction and the Hall conductivity is in the $\hat{y}$ direction, both perpendicular to the magnetic field of the system, which is this case the dipole field of Earth. The parallel conductivity is so named because it is in the direction parallel to the magnetic field (e.g. Kivelson & Russell, 1995). Pedersen conductivity at altitudes relevant for field-aligned currents is usually significantly greater than Hall conductivity.

1.8 Observing the Magnetosphere

Observational data from spacecraft which fly through near-Earth space represent the backbone of most space physics research. All of the plasma and magnetic field data used to carry out the studies here presented come from one of two kinds of science instruments aboard a spacecraft: the fluxgate magnetometer and the electrostatic analyzer. The former measures the magnetic field in the region through which the spacecraft is passing, while the latter measures plasma parameters such as density and bulk velocity.

The fluxgate magnetometer has long been the instrument used by science missions to acquire magnetic field measurements, with the only real variations being the layout of the external electronics. The fundamental design of the sensor itself changes very little from spacecraft to spacecraft. Two ferromagnetic cores are first driven to magnetic saturation by means of wire wound about them. A second set of wire windings is then used to sense any time variations in the magnetic flux in the cores due to external magnetic fields (such as that

of Earth or the solar wind). The electronics unit drives current through a third set of wire windings, called the feedback coils, to cancel out the measured variations in the flux through the cores; the strength of the generated field needed to cancel the ambient magnetic field is what the instrument reports (e.g. Russell et al., 2016).

Plasma parameters are generally measured by means of an electrostatic analyzer. The geometry of individual electrostatic analyzers can vary dramatically, but the basic principle of the instrument remains the same. At the heart of the process is a pair of parallel plates at different potentials, often with one of the plates grounded. Charged particles in the region through which the spacecraft passes can enter the instrument and move between the two plates. Controlling the relative potential of the plates sets the strength of the electric field in the instrument and thus restricts the energy range of the plasma particles that can successfully pass through the detector, analogous to a filter. The instrument records counts of particles, so the resulting measurement of an electrostatic analyzer is a distribution in velocity space of a particular charged species in a certain energy range (e.g. Ogilvie et al., 1995). Some spacecraft spin as they travel and thus change the look angle of the detector; in this way the spinning instrument builds up the three-dimensional distribution as it takes measurements in different directions. The various plasma parameters are obtained by calculating moments of the observed distribution.

1.9 Modeling the Magnetosphere

The magnetosphere-ionosphere system covers an enormous area of near-Earth space, stretching out to 300 R_E in the magnetotail alone. Such a volume in which the phenomena of space physics occur imposes severe limitations on observational studies. Even with the current fleet of spacecraft taking measurements on the dayside, in the magnetotail, in the ionosphere, in the radiation belts, etc., it is simply impossible to obtain simultaneous observations of every region at all times. Further, for a moving spacecraft, the nature of a single point measurement can make it difficult to separate spatial and temporal effects. Numerical models therefore are valuable tools for research as well as for space weather forecasting.

The physics that affects each of the different regions of the system operates on a wide range of length scales. Certain assumptions which are valid in the outer magnetosphere may not hold in the inner magnetosphere or ionosphere and vice versa. Calculating equations of physics which operate on very small length scales requires smaller grid point spacing and becomes too computationally expensive to calculate over the entire magnetosphere, so it is common to use different numerical models for different regions. These various models are then coupled together by an exchange of information at their boundaries at designated timesteps of the simulation, with the temporal cadence chosen as appropriate to properly represent the physical processes and coupling between regions. The commonly separated domains are the magnetosphere and the upstream solar wind, the ionosphere and the thermosphere, and the inner magnetosphere with its different populations.

In the outer magnetosphere and the solar wind, the plasma is collisionless and can be treated as a fluid. The magnetosphere domain is modeled using the equations of ideal magnetohydrodynamics, which combine equations of fluid dynamics, the idealized Ohm's Law, and Maxwell's equations. The MHD equations can be stated thus:

$$\frac{\partial \rho}{\partial t} + \nabla \cdot (\rho \vec{u}) = 0 \tag{1.3}$$

$$\rho \frac{\partial \vec{u}}{\partial t} + \rho(\vec{u} \cdot \nabla)\vec{u} + \nabla p = \vec{J} \times \vec{B} \tag{1.4}$$

$$\frac{\partial \vec{B}}{\partial t} = \nabla \times (\vec{u} \times \vec{B}) + \eta \nabla^2 B \tag{1.5}$$

$$\nabla \times \vec{B} = \mu_0 \vec{J} \tag{1.6}$$

$$\vec{E} + \vec{v} \times \vec{B} = \eta \vec{J} \tag{1.7}$$

where ρ is the density of the plasma, $\vec{u}$ is the plasma bulk velocity, p is the plasma pressure, $\vec{J}$ is the current density, $\vec{B}$ is the magnetic field, and η is the magnetic diffusivity. In ideal MHD, $\eta = 0$, which, when inserted into Equation 1.7, gives rise to the "frozen-in flux" condition discussed in Section 1.2. The above equations represent, in order: the mass continuity equation (Eq. 1.3), the momentum equation or equation of motion (Eq. 1.4), Faraday's Law (Eq. 1.5), Ampere's Law (Eq. 1.6), and Ohm's Law (Eq. 1.7).

Certain models use the semi-conservative form of the MHD equations, which conserve plasma energy rather than requiring a strict conservation of total energy. This method is often chosen to avoid numerical instabilities in regions where the magnetic energy dominates the plasma energy (Lyon et al., 2004; Raeder et al., 2008). For semiconservative schemes, the energy conservation

equation is written

$$\frac{\partial e}{\partial t} + \nabla \cdot [(e + p)\vec{v}] = \vec{J} \cdot \vec{E} \tag{1.8}$$

where e is the plasma energy and $\vec{E}$ is the electric field, while for fully conservative schemes, the energy equation is written

$$\frac{\partial U}{\partial t} = -\nabla \cdot \left[(U + p - \frac{B^2}{2\mu_0})\vec{v} + \frac{1}{\mu_0}(\vec{B} \times \vec{v} \times \vec{B}) \right] \tag{1.9}$$

where U is the total energy, defined as $U = e + \frac{B^2}{2\mu_0}$ or the sum of the plasma energy and the magnetic energy.

MHD grid sizes are on the order of 1 R_E, with higher spatial resolution in regions of interest. In MHD models, magnetic reconnection, although a crucial magnetosphere process, is often not calculated from first principles; rather, reconnection occurs in the simulation as a result of the existence of a discrete number of grid cells. This numerical reconnection can happen when the oppositely directed magnetic field values in neighboring cells are averaged in an interposing cell, which results in a magnetic null point resembling those created by physical reconnection (e.g. Fedder et al., 1995). The rate of reconnection calculated in this way falls short of the rate of reconnection in the real magnetosphere (e.g. Welling, 2019). In spite of this, the MHD models seem to be able to reproduce the magnetosphere reasonably well, as validated by many studies.

Magnetosphere models are driven by solar wind observations, usually from satellites orbiting the first Lagrangian point, as described in Section 1.2, and propagated to a point closer to the magnetosphere such as a nominal bow shock location. The solar wind enters the simulation at the dayside boundary of the

grid, usually about 30 R_E upstream of Earth. Because these are observations of a single point in a vast region of inhomogenous solar wind flow, modelers must assume that the conditions observed at L1 represent a planar front that does not vary over the width and height of the simulation grid, which is not always the case (e.g. Borovsky, 2008). This assumption also presents problems for the requirement that $\nabla \cdot \vec{B} = 0$, a challenge which different models tackle in different ways. One method involves expressing the solar wind B_X component as a linear function of B_Y and B_z (Lyon et al., 2004), while another does not strictly require $\nabla \cdot \vec{B} = 0$, using a numerical process called elliptical cleaning to periodically find and remove any magnetic monopoles which may have been formed by the calculations (Tóth, 2000). Both methods have their drawbacks: for example, the former can make it difficult to accurately simulate periods of strong IMF B_X, while the latter may cause shock jump conditions not to be met. There are other, more mathematical reasons for dropping the $\nabla \cdot \vec{B} = 0$ source term in the derivations for the models: among other issues, the system without the source term is not Galilean invariant or symmetrizable (Powell et al., 1999). Modelers must make certain compromises and approximations for the sake of numerical stability, weighing the benefits and drawbacks of the available approaches.

All MHD models include an ionosphere model inside their inner boundary, which is generally between 2 and 3 R_E from the center of Earth, where the fluid description of the plasma starts to break down. The most basic models perform their calculations on a two-dimensional conducting spherical shell, taking the FACs calculated in the magnetosphere and mapping them down towards Earth along dipole field lines. Other, more physics-based models of the ionosphere

and the thermosphere exist and can be coupled to the magnetosphere at the same boundary (e.g. Dickinson et al., 1981; Raeder et al., 2009). Some part of the model or coupled models provides values for the ionospheric conductance, using it with the FACs to calculate the electric potential across the polar cap. The equation used for this calculation is

$$\nabla_{\perp} \cdot (\Sigma \cdot \nabla_{\perp} \Phi) = J_{||} / sin(I) \tag{1.10}$$

where Σ is the conductance, Φ is the electric potential, $J_{||}$ is the field-aligned current, and I is the angle of magnetic inclination. The right hand side represents the radial component of the FACs. Equation 1.10 follows from Ohm's Law, the current continuity equation, and the relation $\vec{E} = -\nabla_{\perp} \Phi$, the last of which requires that the ionosphere is electrostatic (e.g. Raeder et al., 2008; Ridley et al., 2004; Ridley et al., 2001; Wiltberger et al., 2009). Conductance is calculated either from first-principles, which must account for complex electron and ion processes, or using empirical relationships, which are based on limited datasets and have associated uncertainties (e.g. Mukhopadhyay et al., 2022; Mukhopadhyay et al., 2020; Ridley et al., 2004; Ridley et al., 2001). The simplest conductance model specifies constant values for the Pedersen and the Hall conductances, a tactic which is often used in numerical experiments to identify cause and effect for phenomena being studied.

Close to Earth but still in the magnetosphere, kinetic effects become important and it is necessary to couple the MHD models to specialized inner magnetosphere models. There are two main kinds of inner magnetosphere models,

namely, models that calculate the distribution function of the ring current population and models that describe the relativistic energies of the radiation belts. Ring current models are commonly used in global magnetosphere models for studies of geomagnetic storms and cover the region of closed field lines, where ion and electron drift physics dominates. For simplicity, some ring current models assume an isotropic pitch angle distribution, taking the magnetic field from the coupled MHD model at the boundary (e.g. Toffoletto et al., 2003; Wolf et al., 1982), while others can compute full pitch-angle distributions (e.g. Fok et al., 2001; Liemohn et al., 2004; Ridley & Liemohn, 2002). Ring current models compute Region 2 field-aligned currents self-consistently, passing these results to the coupled ionosphere and MHD models (e.g. Pembroke et al., 2012; Tóth et al., 2005). The MHD codes also receive the inner magnetosphere plasma pressures and densities, which nudge the corresponding MHD quantities towards more realistic values.

The standard configuration of the most commonly used MHD models treats the plasma as a fluid with a single species of charged particle, i.e. protons, but this approach ignores electrons and heavier ions. Multi-fluid versions of some of the codes have been and continue to be developed (e.g. Tóth et al., 2012; Wiltberger et al., 2010; Zhang et al., 2019). In addition, some models attempt to treat reconnection more physically by including resistive terms in the MHD equations or embedding particle-in-cell models within the MHD framework. Particle-in-cell (PIC) codes follow the trajectories of individual charged particles subject to both electromagnetic forces and kinetic effects. To run PIC codes over the volume of the magnetosphere is prohibitively expensive in terms of computing

resources, so the most common technique is to designate certain regions of interest and use a PIC model to describe the physics at those locations (e.g. Shou et al., 2021).

Despite its limitations, global MHD with its coupled models remains the standard approach in space physics research, both at Earth and for other magnetospheres. As shown by decades of studies comparing model results to data, the global MHD approach can reproduce the magnetosphere and many of its processes reasonably well. Ongoing work in model coupling and improvement continues to advance the state of magnetosphere simulation capability, while validation studies seek to identify strengths and weakness of the various available models. Such work is of especial interest if a model is being used for space weather prediction, as it relates to the level of confidence in the model results.

1.10 Description of Included Studies

The studies that make up the chapters of this work represent research that stretches in its phenomenology over several different regions of the geospace system. In particular, the research here presented focuses on dayside boundaries and currents and their connections to the ionosphere and inner magnetosphere, using data from a variety of sources and results from four global MHD models. The two chapters following this introduction discuss the ability of the MHD models to simulate the location and motion of the magnetopause from the point of view of event studies. First, a quantitative approach calculates metrics that measure the models' performance; second, an extended study that encompasses the

second and third chapters considers the reasons for model performance, investigating the effects of coupling a ring current model to the MHD code, varying the ionosphere models, increasing grid resolution, comparing solar wind observations from different sources, and categorizing types of solar wind drivers. The fourth chapter details a case study of the possibility of bow shock current closure into the ionosphere. This study includes observations at the bow shock and in the ionosphere and compares these data with the results from a global MHD model. The concluding chapter discusses future work regarding both the magnetopause predictions and the bow shock current.

Chapter 2

Magnetopause Location as Predicted by Four MHD Models

2.1 Abstract

During intense geomagnetic storms, the magnetopause can move in as far as geosynchronous orbit, leaving the satellites in that orbit out in the magnetosheath. Spacecraft operators turn to numerical models to predict the response of the magnetopause to solar wind conditions, but the predictions of the models are not always accurate. This study investigates four storms with a magnetopause crossing by at least one GOES satellite, using four magnetohydrodynamic models at NASA's Community Coordinated Modeling Center (CCMC) to simulate the events, and analyzes the results to investigate the reasons for errors in the predictions. Two main reasons can explain most of the erroneous predictions. Firstly, the solar wind input to the simulations often contains features measured near the L1 point that did not eventually arrive at Earth; incorrect predictions

during such periods are due to the solar wind input rather than to the models themselves. Secondly, while the models do well when the primary driver of magnetopause motion is a variation in the solar wind density, they tend to overpredict or underpredict the integrated Birkeland currents and their effects during times of strong negative IMF B_z, leading to poorer prediction capability. Coupling the MHD codes to a ring current model, when such a coupling is available, generally will improve the predictions but will not always entirely correct them. More work is needed to fully characterize the response of each code under strong southward IMF conditions as it relates to prediction of magnetopause location.

N.B. The text in this chapter is taken almost entirely, with the exception of Section 2.4, from the paper Dredger et al., 2023b, submitted to the journal Space Weather, *accepted on February 14, 2023, and awaiting publication. The work discussed in Section 2.4 is taken from the companion paper Collado-Vega et al., 2023, which is undergoing revisions for the same journal. The two articles will be published together.*

2.2 Introduction

As discussed in Section 1.5, the location of the magnetopause is determined by the balance of pressures from inside and outside the boundary, particularly solar wind dynamic pressure and the magnetic pressure of the dipole field. The dipole field can be weakened by the effects of fringe fields generated by the Region 1 FACs and the cross-tail current on the nightside, both of which grow in strength with increasing IMF B_y. The ring current, which is strongest during a

geomagnetic storm, can also affect the position of the magnetopause. As ions are injected from the tail into the inner magnetosphere, they join the ring current and drift clockwise around Earth (as seen from the north); because of the direction of the drift, more energetic particles are lost to the dawn sector magnetopause than to the dusk sector, and the ring current becomes asymmetrical. The resulting partial ring current closes along magnetic field lines as the Region 2 field-aligned current, flowing into the polar cap on the dusk side and out on the dawn side. The stronger thermal pressure from the ions in the partial ring current in the dusk sector causes the magnetopause to be farther away from Earth than it is in the dawn sector (Dmitriev et al., 2011).

During times of quiet solar wind, the magnetopause is several Earth radii away from geosynchronous orbit, where many commercial and scientific satellites are located, and so these spacecraft remain inside the magnetosphere. On the other hand, when the solar wind driver of a geomagnetic storm arrives at Earth, the location of the boundary is much more variable (Bonde et al., 2018). Operators of satellites orbiting near Earth rely on predictions of the magnetopause location to let them know if their spacecraft might cross the boundary, particularly if the spacecraft use magnetic torquing for attitude adjustments (Sibeck, 1995). Often to make these predictions, satellite operators use the magnetohydrodynamic (MHD) models available at the CCMC: the Lyon-Fedder-Mobarry simulation (LFM), the Space Weather Modeling Framework (SWMF), the Open Geospace General Circulation Model (OpenGGCM), and the Grand

Unified Magnetosphere-Ionosphere Circulation Model (GUMICS). While empirical models of magnetopause position exist, physics-based models can provide a better (if imperfect) prediction capability during extreme magnetic storms (Lopez et al., 2007).

Collado-Vega et al. (2023) conducted a companion study examining the performance of these four models in predicting magnetopause location for eight storms; specifically, the study looked for correctly simulated magnetopause encounters at the locations of GOES 13 and 15, both at geosynchronous orbit. We found that SWMF and GUMICS tended to underpredict magnetopause motion in response to strong solar wind conditions, while LFM and OpenGGCM predicted both correct and spurious magnetopause crossings. The results are summarized in more detail in Section 2.4 and are referred to as "Part 1" of the study.

In order to better understand the models' predictive capabilities, including under what conditions their use is appropriate, the main body ("Part 2") of this study investigates possible causes for their incorrect predictions. In particular, we examine the overpredictions of LFM and OpenGGCM by considering the four events in the Collado-Vega paper in which the GOES spacecraft actually crossed the magnetopause. Where Part 1 focuses on performance metrics of the MHD codes' predictive abilities, the analysis of Part 2 takes rather a qualitative than a quantitative approach, addressing underlying reasons for the MHD predictions on a model-by-model basis.

2.3 Methodology

To determine the time at which a satellite crosses the magnetopause, the following method was used. Earth's magnetic field points northward, so a magnetometer will always read a positive B_z while inside the magnetopause. If the incoming IMF has a negative Z-component, the compressed B_z in the sheath will be negative. Consequently, in magnetometer data, B_z will rotate from positive (negative) to negative (positive) as the spacecraft crosses the boundary into the magnetosheath (magnetosphere). We consider that the spacecraft encounters the magnetopause at the moment the magnetometer reads $B_z = 0$ nT. All the events in this study had strong southward IMF components, so magnetopause crossings in the relevant data were identified in this way, following Lopez et al. (2007). Technically speaking, however, the condition $B_z = 0$ nT is only a proxy for magnetopause location and we are investigating the models' ability to predict that condition.

For this study, events were chosen in which solar wind conditions pushed the magnetopause so far towards Earth that it approached geosynchronous orbit, where the GOES satellites fly. In Part 1, although the boundary was most likely close to geosynchronous orbit, in four out of the eight events considered there were no observed magnetopause crossings. In Part 2 we analyze the other four events, during which the magnetopause crossed over one or both of GOES 13 and 15. GOES 13 and 15 are part of NOAA's Geostationary Operational Environmental Satellite program and fly in geosynchronous orbits. During the events of this study, GOES 13 was located at 75 degrees West and GOES 15 was located at 135 degrees West, which means that GOES 13 was always four hours

ahead of GOES 15 in local time.

Each event was simulated using all four magnetospheric models at the CCMC, without a ring current and using the default auroral conductance in order to compare the models as fairly as possible, since the couplings available vary among the codes. After these initial runs, the simulations for certain events were repeated with the MHD codes coupled to a ring current model where such a coupling was available at the CCMC. The four models used in this study are the LFM model, the SWMF, OpenGGCM, and GUMICS. These are briefly described here with their various possible couplings, as available at the CCMC. The resolution of the models was in all cases the lowest available, which varies among the four models.

LFM solves the semi-conservative MHD equations on a stretched spherical grid and uses its Magnetosphere-Ionosphere Coupler/Solver (MIX) to model the ionosphere (Lyon et al., 2004). MIX takes the field-aligned currents calculated at the inner boundary of the MHD code and maps them down to the ionosphere grid, which extends in each hemisphere to 45^o latitude, using the currents with a given conductance to calculate the potential (Merkin & Lyon, 2010). LFM can also be two-way coupled with the Rice Convection Model (RCM), a bounce average drift kinetic model of the inner magnetosphere that adds ring current physics (Toffoletto et al., 2003; Wolf et al., 1982). LFM provides the magnetic field and plasma boundary conditions to RCM, which calculates the pressure and density of the ring current and returns these values to the MHD code. MIX passes its potential solution to both LFM and RCM (Pembroke et al., 2012). The

version of LFM-MIX coupled to RCM is available for use at the CCMC. The resolution of the runs in this study is 53x48x64 cells and the size of the cells at the GOES orbit, on the dayside, is about 0.4 R_E in each direction.

SWMF includes a number of modules that simulate various parts of the space weather system (Tóth et al., 2005; Tóth et al., 2012). The magnetosphere part of the framework (SWMF Global Magnetosphere or GM module) uses the Block-Adaptive-Tree-Solarwind-Roe-Upwind-Scheme (BATS-R-US), which solves the conservative MHD equations on a block-adaptive grid (Powell et al., 1999). RCM is coupled into the framework as the Inner Magnetosphere (IM) module and functions similarly to the way it is coupled to LFM, as described above. The IM component receives the magnetic field and plasma initial and boundary values from BATS-R-US and passes back corrected pressure values for the inner magnetosphere to the GM module (Zeeuw et al., 2004). The SWMF Ionosphere Electrodynamics (IE) module uses the field-aligned currents from BATS-R-US to calculate the ionospheric potential and conductance, returning the potential to the GM and IM modules (Ridley et al., 2004; Ridley et al., 2001; Ridley & Liemohn, 2002). The ionosphere grid is a complete sphere around Earth, but the auroral conductance model providing the conductance for the potential calculation only reaches 60^o magnetic latitude (Mukhopadhyay et al., 2020). SWMF request runs at the CCMC couple BATS-R-US with the two-dimensional IE potential solver and can include RCM. Runs in this study use the version of the code implemented on the website in 2014 and a one million cell overview grid. The size of the cells at the GOES locations for the events here presented is 0.25 R_E in each direction.

OpenGGCM solves the semi-conservative MHD equations on a stretched Cartesian grid and maps the field-aligned currents onto a sphere within the inner boundary to a convection potential solver. OpenGGCM can also be coupled to RCM, but this coupling was not used in this work (Cramer et al., 2017; Raeder et al., 2008; Raeder et al., 2001). The simulations in this study were run on a seven million cell overview grid, with cell sizes at the GOES locations of about 0.15 R_E in the X direction and 0.25 R_E in Y and Z.

GUMICS-4, the version of GUMICS used here, couples an MHD model of the magnetosphere to an ionosphere model. The magnetosphere part of the code solves the conservative MHD equations on a refined hierarchically adaptive octogrid with a locally varying time-step, while the simulation of the ionosphere is based on solving the height-integrated current continuity equation on a spherical surface with a prescribed grid point density highest in the auroral oval (Janhunen et al., 2012). GUMICS does not have the option for a ring current model coupling at the CCMC. GUMICS was run on a grid of 100,000 cells; the cell size at the GOES locations was 0.5 R_E along each axis.

2.4 Part 1: Metrics

There are various metrics used to measure the accuracy of a forecast. The ones used here all begin with a contingency table, which places an individual prediction into one of four categories: Yes when it should be Yes (hits), Yes when it should be No (false alarms), No when it should be Yes (misses), and No when

it should be No (correct negatives). A prediction that the satellite is in the magnetosheath when it was observed to be in the magnetosheath is a hit, while a prediction that the satellite is in the magnetosheath when it was observed to be in the magnetosphere is a false alarm. A miss is a prediction that the satellite was in the magnetosphere when it was actually in the magnetosheath, and a correct negative is a correct prediction that the satellite was in the magnetosphere.

TABLE 2.1: Contingency Table for GOES 13 magnetopause crossings observations predicted by LFM and SWMF on all the events.

Observations Model	**Yes** LFM	**No** LFM	**Total** LFM	**Yes** SWMF	**No** SWMF	**Total** SWMF
Forecast Yes	21	24	45	14	0	14
Forecast No	3	477	480	10	501	511
Total	24	501	525	24	501	525

TABLE 2.2: Contingency Table for GOES 13 magnetopause crossings observations predicted by OpenGGCM and GUMICS on all the events.

Observations Model	**Yes** OpenGGCM	**No** OpenGGCM	**Total** OpenGGCM	**Yes** GUMICS	**No** GUMICS	**Total** GUMICS
Forecast Yes	16	53	69	7	0	7
Forecast No	8	448	456	17	501	518
Total	24	501	525	24	501	525

The contingency tables for all four events are shown in Tables 2.1-2.4, separated by satellite. From the contingency tables, we calculate nine different skill scores, which are shown in Tables 2.5 and 2.6. These skill scores and their calculations are described in detail in Lopez et al. (2007), but they are briefly summarized here.

TABLE 2.3: Contingency Table for GOES 15 magnetopause crossings observations predicted by LFM and SWMF on all the events.

Observations Model	**Yes** LFM	**No** LFM	**Total** LFM	**Yes** SWMF	**No** SWMF	**Total** SWMF
Forecast Yes	19	38	57	14	0	14
Forecast No	9	459	468	14	497	511
Total	28	497	525	28	497	525

TABLE 2.4: Contingency Table for GOES 15 magnetopause crossings observations predicted by OpenGGCM and GUMICS on all the events.

Observations Model	**Yes** OpenGGCM	**No** OpenGGCM	**Total** OpenGGCM	**Yes** GUMICS	**No** GUMICS	**Total** GUMICS
Forecast Yes	17	53	70	12	0	12
Forecast No	11	444	455	16	497	513
Total	28	497	525	28	497	525

The first is Accuracy (A), which is simply the fraction of predictions that were correct, ranging from 0 to 1 with 1 being a perfect score. Used in this study, A can be heavily skewed by the large number of correct negatives, since the magnetopause is rarely either observed or predicted to be past geosynchronous orbit. Model Bias (B) measures how likely a model is to under forecast or over forecast by comparing the number of Yes predictions with the number of Yes observations. B ranges from 0 to infinity with 1 being a perfect score.

Probability of detection (POD) is the fraction of correctly predicted Yes events. POD ranges from 0 to 1 with 1 being a perfect score. The false alarm ratio (FAR) is the ratio of false alarms to Yes predictions, ranging from 0 to 1 with 0 being a perfect score and complementing the POD. The probability of false detection (POFD), the opposite of the POD, is the fraction of correctly predicted No events,

ranging from 0 to 1 with 0 being a perfect score.

More sophisticated scores include the critical success index (CSI), the true skill score (TSS), the modified true skill score, and the Heidke skill score. The CSI remedies the skew in A due to an abundance of correct negatives by calculating the ratio of hits to the total without the correct negatives; this score ranges from 0 to 1 with 1 being a perfect score. The TSS is the difference between the POD and the POFD, ranging from -1 to 1, with 1 being a perfect score and 0 indicating no skill. The MTSS is similar, but removes the potential for undue weighting of the POD for rare events like magnetopause crossings that is present in the TSS. The HSS represents the fraction of correct predictions compared to a forecast full of random predictions. It ranges from negative infinity to 1, with 0 indicating no skill and 1 being a perfect score. All of these metrics have greater or lesser weaknesses and should be considered together to better characterize a set of predictions.

TABLE 2.5: Skill Scores for every model prediction on all 8 events for GOES 13.

Scores	**LFM**	**SWMF**	**OpenGGCM**	**GUMICS**	**Perfect Score**
A	0.95	0.98	0.88	0.97	1
B	1.88	0.58	2.88	0.29	1
POD	0.88	0.58	0.67	0.29	1
FAR	0.53	0	0.77	0	0
POFD	0.05	0	0.11	0	0
CSI	0.44	0.58	0.21	0.29	1
TSS	0.83	0.58	0.56	0.29	1
MTSS	0.65	0.17	0.10	-0.42	1
HSS	0.58	0.73	0.30	0.44	1

TABLE 2.6: Skill Scores for every model prediction on all 8 events for GOES 15.

Scores	**LFM**	**SWMF**	**OpenGGCM**	**GUMICS**	**Perfect Score**
A	0.91	0.97	0.88	0.97	1
B	2.04	0.50	2.47	0.43	1
POD	0.68	0.50	0.61	0.43	1
FAR	0.67	0	0.75	0	0
POFD	0.08	0	0.11	0	0
CSI	0.29	0.50	0.21	0.43	1
TSS	0.60	0.50	0.50	0.43	1
MTSS	0.19	0	-0.02	-0.14	1
HSS	0.40	0.65	0.29	0.59	1

Across the eight events, all of the models score high for Accuracy. The SWMF and GUMICS show a tendency to under forecast, while LFM and OpenGGCM tend to over forecast. POD varies between the two satellites: GUMICS predicts a hit less than 50% of the time, LFM and OpenGGCM do better than 50%, and the SWMF is in the middle. The SWMF and GUMICS predict no false alarms while LFM and OpenGGCM predict many, with OpenGGCM predicting more. All four models score very well for POFD, especially the SWMF and GUMICS. The SWMF scores highest for the CSS and LFM has the highest TSS. The scores for the MTSS are difficult to interpret due to the differences between the two satellites. Finally, the SWMF has the highest HSS.

Overall, the different models seem to have strengths and weaknesses. OpenGGCM has a strong tendency to overpredict the inward motion of the magnetopause. LFM also predicts quite a few false magnetopause crossings (although fewer than OpenGGCM). Both models, however, usually reproduce real crossings more or less accurately, allowing for errors in the timing of the solar wind

input. The SWMF is more conservative, missing some real crossings but also avoiding any prediction of spurious crossings. GUMICS is even more likely to underpredict; only in one out of the eight events does GUMICS predict a magnetopause crossing by either satellite.

2.5 Part 2: Causes

2.5.1 Solar Wind Discrepancies

A closer examination of the individual events reveals that the solar wind input to the models may have caused some of the incorrect predictions. Because of the inhomogeneous nature of the solar wind, the conditions observed by a monitor at the first Lagrange point may differ significantly from the solar wind that actually impacts the magnetosphere. Comparisons between the OMNI dataset, which is composed of L1 observations from ACE and Wind propagated to a nominal bow shock position, and data from other spacecraft that were temporarily in the solar wind during the various events, reveal significant discrepancies between the datasets that explain several of the false positives in the model predictions. Although the L1 observations may not be inherently flawed, such data are not always appropriate for simulating downstream conditions.

The first event, 2011 August 5, contains a feature in the solar wind input that may have caused one of the models to predict a spurious magnetopause crossing by both GOES 13 and GOES 15. We see in Figure 2.1 the actual GOES observations and the model predictions plotted together. B_z from the model is plotted in GSE coordinates and the real data are in the cylindrical coordinate system used

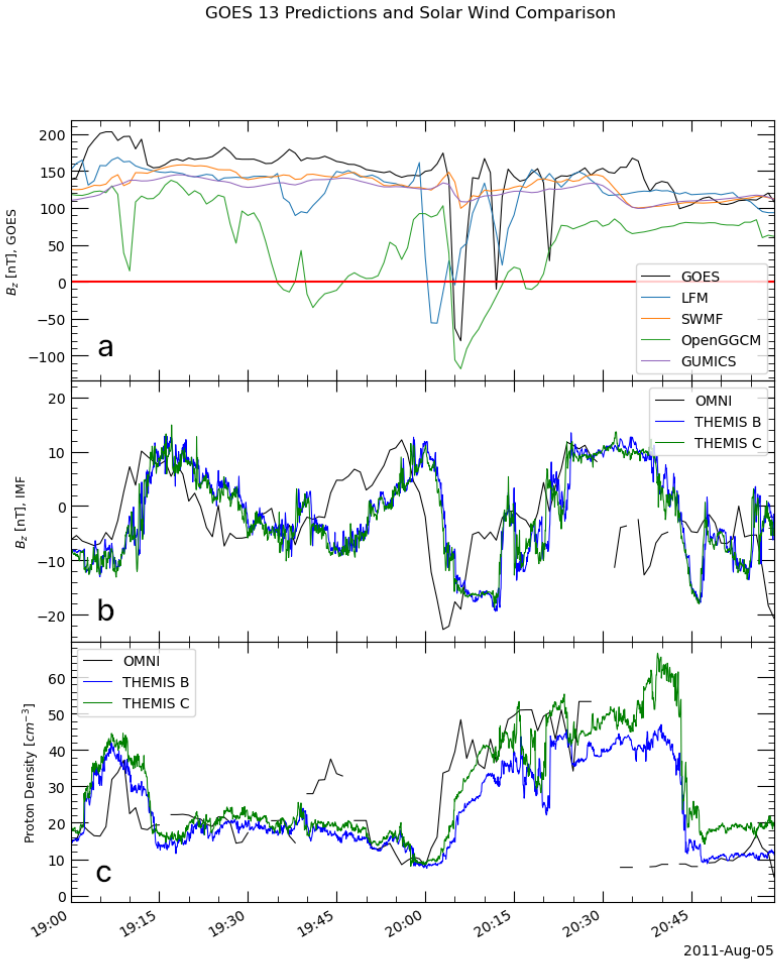

FIGURE 2.1: From top to bottom: (a) Observations of B_z from GOES 13 with predictions from LFM, SWMF, OpenGGCM, and GUMICS. The red horizontal line is included in this and any following GOES plots for ease of identifying magnetopause crossings, which occur at B_z = 0 nT under southward IMF conditions. (b) IMF B_z from OMNI compared with measurements from THEMIS B and C. Note that the propagation of OMNI data to a nominal bow shock does not necessarily correspond with the location of THEMIS B/C and so a shift in the time series is present. (c) Proton densities from OMNI and from THEMIS B/C.

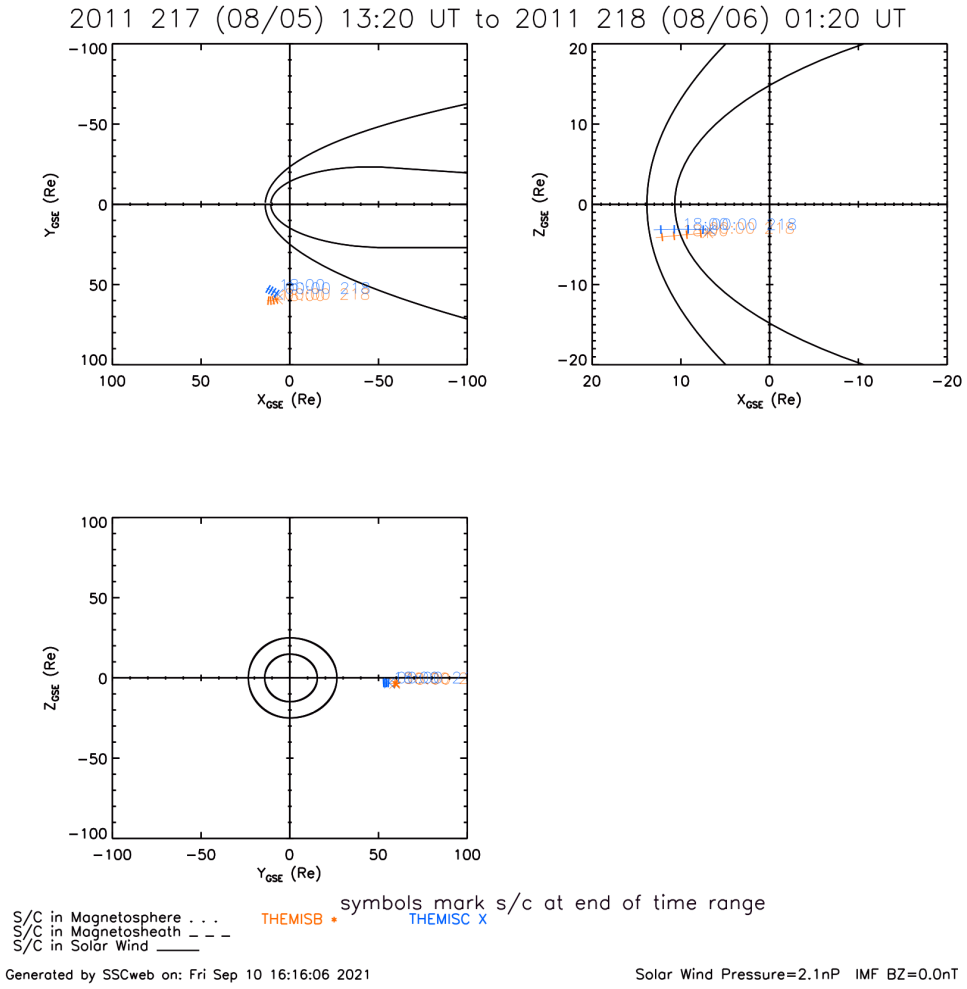

FIGURE 2.2: Locations of THEMIS B and C during the 2011 August 5 event. Although the two spacecraft are more than 50 R_E off the Earth-sun line, they are the only other source of solar wind observations for this event (plot from SSCWeb).

by GOES – the quantity plotted here is H_p, which is generally equivalent to B_z. Around 19:40 UT, B_z as predicted by OpenGGCM dips below 0 nT, indicating a magnetopause crossing by the satellite under consideration. LFM predicts an approach to the magnetopause around the same time but not a crossing. SWMF and GUMICS do not predict a change in B_z at this time. The solar wind from the OMNI dataset, which was provided by Wind during this event, shows a density pulse from about 20 cm^{-3} to 40 cm^{-3} that caused the simulated magnetopause to move inward over the locations of GOES 13 and 15. This density pulse, observed at L1, does not seem to have actually reached Earth. THEMIS B and C were in the solar wind at the time as shown in Figure 2.2, although they were between 50 and 60 R_E away from the Earth-Sun line. They did not record the increase in the solar wind density that Wind saw further upstream. The magnetometer and THEMIS observations, combined with the lack of a real magnetopause crossing at geosynchronous orbit, strongly suggest that the density pulse in the OMNI data at 19:40 UT did not impact the magnetopause. Thus, the erroneous predictions of magnetopause crossings were not necessarily due to issues with OpenGGCM but more likely the consequence of the wrong solar wind input.

A second event, 2011 September 26, tells a similar story. OpenGGCM predicts a magnetopause crossing at the location of GOES 13 shortly after 14:00 UT, in response to a southward turning of IMF B_z accompanied by high proton densities in the OMNI data, which was once again provided by Wind (Figure 2.3). LFM, SWMF, and GUMICS do not predict a magnetopause approach during the period shown in Figure 2.3. This time, THEMIS B and C were well-positioned

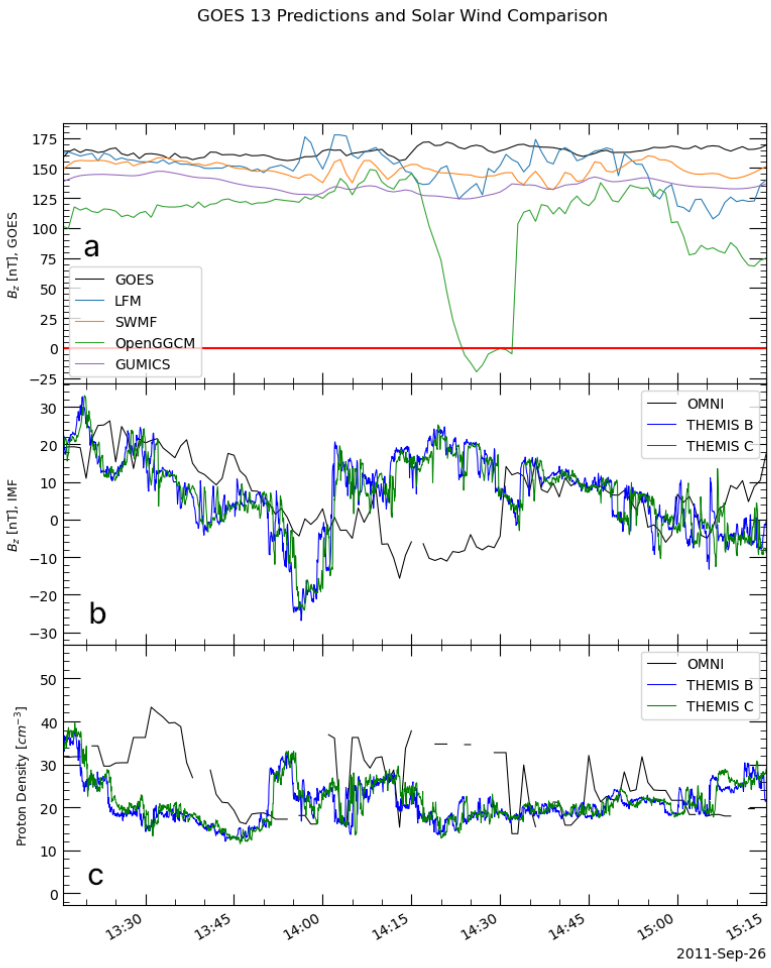

FIGURE 2.3: (a) GOES 13 observations and corresponding MHD predictions of B_z, along with (b) IMF B_z and (c) solar wind proton densities from OMNI and THEMIS B/C for 2011 September 26. Even taking into account potential timing issues with the OMNI propagation, there are still significant differences in the OMNI and THEMIS sets of solar wind observations.

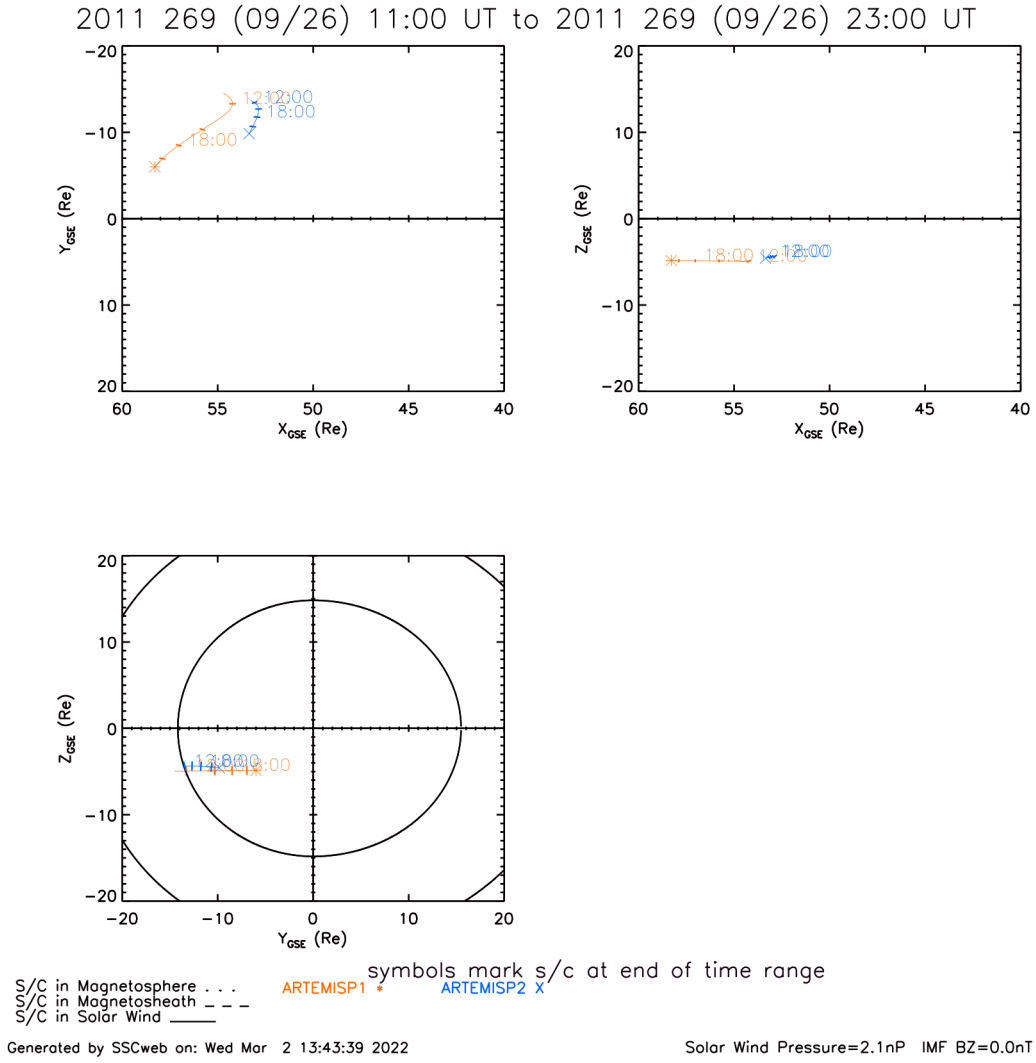

FIGURE 2.4: Locations of THEMIS B/C during the 2011 September 26 event. During this period, the two spacecraft were relatively close to the Earth-sun line and so their observations should be a good representation of the solar wind that impacted the bow shock (plot from SSCWeb).

(Figure 2.4) to provide solar wind observations 170 R_E closer to Earth than Wind, less than 20 R_E from the Earth-Sun line. B_z in the OMNI was southward, reaching around -10 nT between 14:10 and 14:30 UT, while the IMF B_z observed by THEMIS B and C was positive, with an overall difference of at least 20 nT between THEMIS and OMNI. Proton densities at THEMIS B and C were also much less than those in OMNI by roughly 15 cm^{-3} during the same period. This difference would have resulted in a simulated magnetopause located closer to Earth than in reality. The source of the solar wind input seems once again to explain the spurious crossing after 14:00 UT, although it is clearly not the only issue with the simulation results, given the other false crossings predicted later in the day by LFM and OpenGGCM (see discussion in Section 2.5.2).

In addition to predicting false crossings, the models can also miss real crossings because of problems with the solar wind input. GOES 15 crossed the magnetopause right after 23:00 UT on 2017 September 7, but none of the models reproduced that crossing (Figure 2.5). THEMIS A, D, and E were intermittently in the solar wind between 23:00 and 23:30 UT, all within 2 R_E of the nose of the bow shock (Figure 2.6), and observed a negative IMF B_z of -20 nT or stronger right after 23:00 UT, while the IMF B_z from OMNI (provided by Wind) was -10 nT or weaker. Thus, even the two models that predicted the crossings minutes later, i.e. LFM and OpenGGCM, did not capture the initial crossing, probably due at least in part to this discrepancy between the two sets of solar wind observations. Unfortunately, the THEMIS spacecraft were not in the solar wind for very long and cannot be used to confirm the OMNI data later in the event.

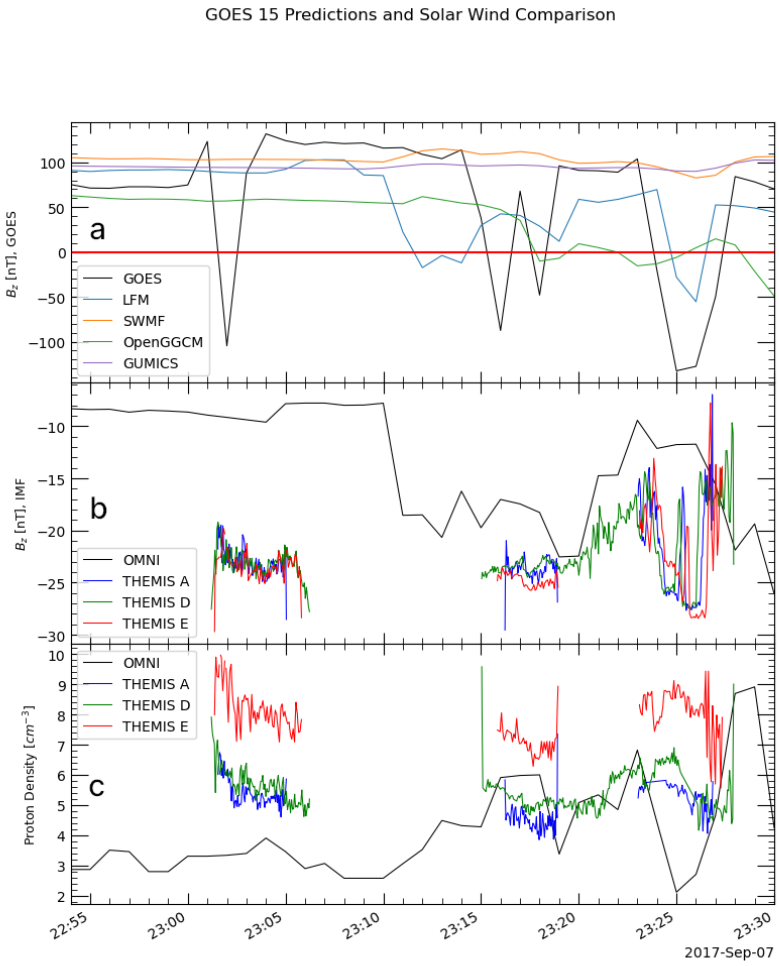

FIGURE 2.5: (a) GOES 15 observations and model predictions of B_z with (b) IMF B_z and (c) solar wind proton densities from OMNI and THEMIS A/D/E. THEMIS data are only plotted for the brief periods during which the spacecraft were in the solar wind. During this period the solar wind velocity (not shown here) changed drastically, so, as in previously discussed cases, there may be timing issues from the OMNI propagation.

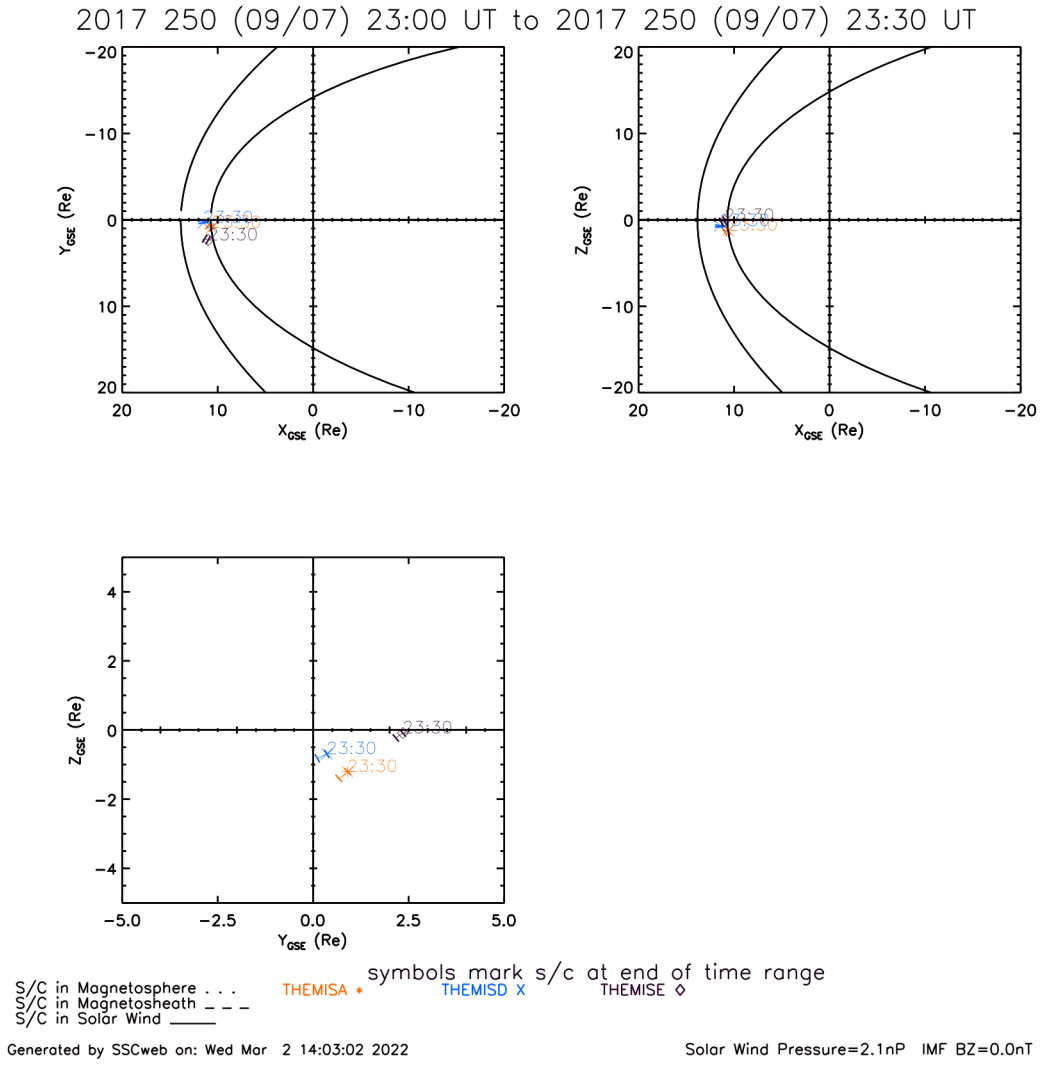

FIGURE 2.6: THEMIS A/D/E locations from 23:00 UT to 23:30 UT on 2017 September 7 (plot from SSCWeb).

2.5.2 Solar Wind Driver of Magnetopause Motion: IMF B_z vs. Density

Classification of the types of solar wind driver for the magnetopause crossings in each event leads to a further explanation of the false alarms and misses in the simulation results. The models seem to make good predictions when a sudden density increase drives the magnetopause inward, but perform poorly for events in which the magnetopause is eroded by the presence of a negative IMF B_z component. The predictions for 2011 September 26, shown in Figure 2.7, follow this pattern. After the initial false crossing in OpenGGCM due to use of the incorrect solar wind input right after 14:00 UT, both OpenGGCM and LFM predict a series of crossings before and after the real crossing at 16:40 UT. The false crossings between 15:40 and 17:00 UT could be due to the fact that the OMNI densities were higher than those observed by THEMIS B/C from 15:10 to roughly 16:00 UT, in a similar manner to the examples in Section 2.5.1, although there is also a period of southward IMF B_z at this time. On the other hand, during the times of the spurious crossings between 18:00 and 19:00 UT, the solar wind proton densities in both OMNI and THEMIS B and C are much lower than they were earlier in the event without much variation, while IMF B_z is strongly negative. Both models predict that the GOES satellites reenter the magnetosphere after the real crossings starting at 19:20 UT, a series of brief encounters with the boundary that were probably caused by the density increase in the solar wind at that time. The false crossings in LFM and OpenGGCM between 18:00 and 19:00 UT seem to be caused by the strong negative IMF B_z, since there is little change in the solar wind densities during this period.

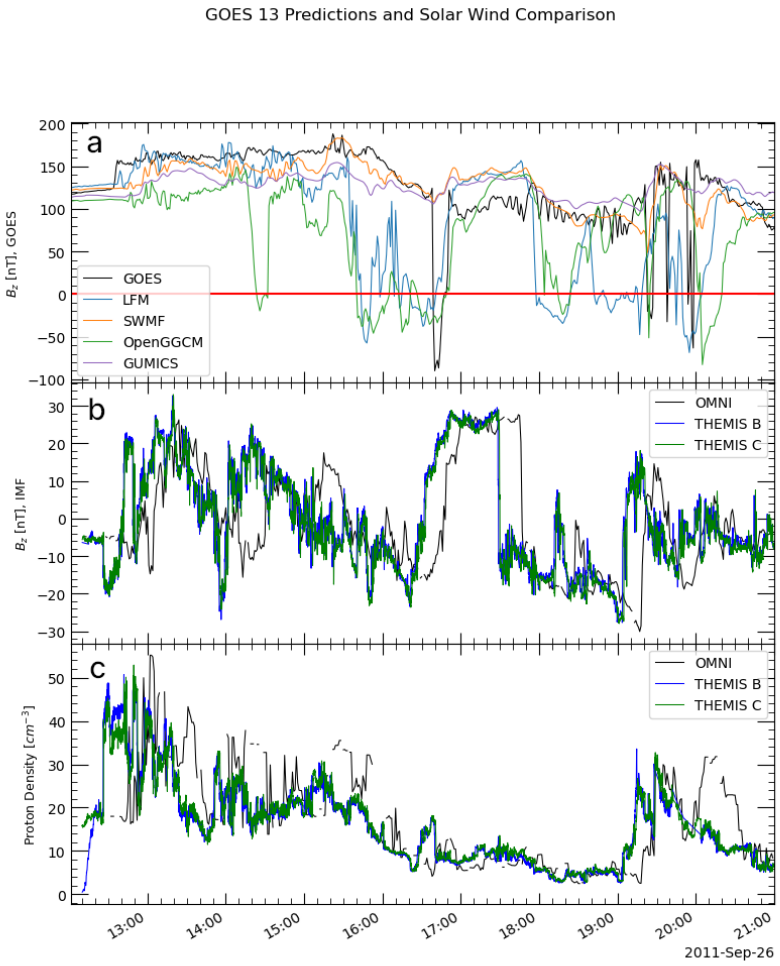

FIGURE 2.7: (a) GOES 13 observations and model predictions of B_z with (b) IMF B_z and (c) solar wind proton densities from OMNI and THEMIS B/C. LFM and OpenGGCM predict spurious magnetopause crossing during times when magnetopause motion is primarily driven by southward IMF B_z.

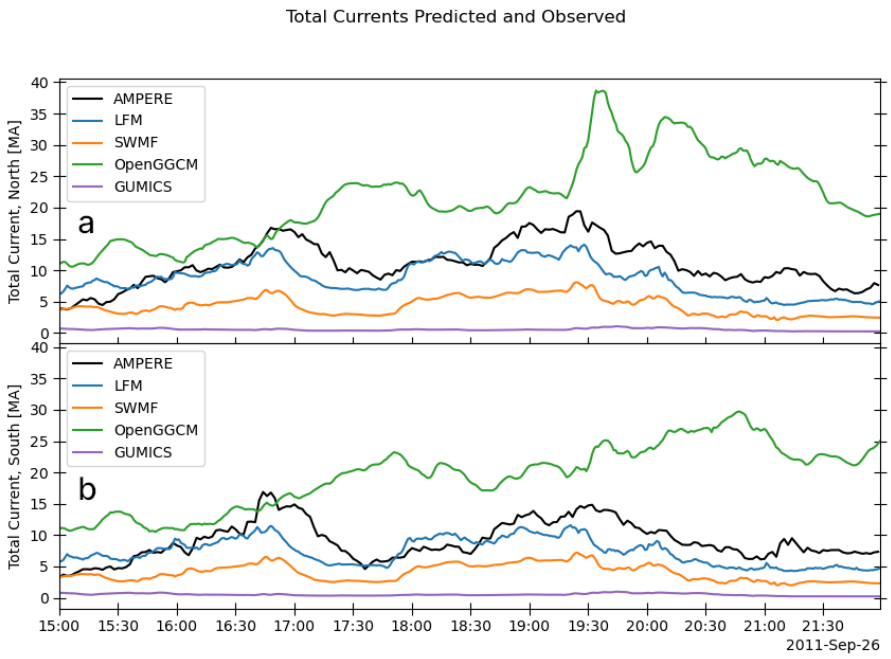

FIGURE 2.8: Total integrated field-aligned currents in the (a) northern and (b) southern hemispheres from AMPERE and as predicted by the MHD models for 2011 September 26.

The total integrated field-aligned currents from each model on 2011 September 26 are plotted in Figure 2.8 alongside the integrated currents from AMPERE. The two models that do not predict either real or spurious crossings, SWMF and GUMICS, have less current flowing into and out of the ionosphere than LFM or OpenGGCM, which have currents either similar to or greater than the AMPERE integrated FACs. This event occurred near equinox, so the currents in both hemispheres are of similar strength. At 16:40 UT, the time of the real GOES 13 crossing, the AMPERE currents increase but the currents from LFM and SWMF actually decrease, probably in response to the northward turning of OMNI IMF B_z at this time, and GOES 13 in the LFM predictions exits the magnetosheath early. The modeled currents from LFM and SWMF increase later right before 18:00 UT, when LFM and OpenGGCM predict more false crossings. OpenGGCM currents remain higher than and show little qualitative similarity to the AMPERE integrated currents throughout the whole event. From about 16:10 to 19:30 UT, OMNI and THEMIS B and C all agree reasonably well, so the false crossings between 18:00 and 19:00 UT cannot be explained by discrepancies in the solar wind input to the simulations. The patterns of real and modeled currents correspond well to the real and modeled GOES observations, but the models respond more to the IMF variations while the observations respond to changes in solar wind proton density.

The simulations of the geomagnetic storm of 2015 June 22 follow the same tendencies. All four models capture the magnetopause crossings by GOES 13 and 15 that lasted from right after 18:30 until about 20:00 UT. These crossing were driven by a sharp increase in the solar wind density from 10 cm^{-3} to 60

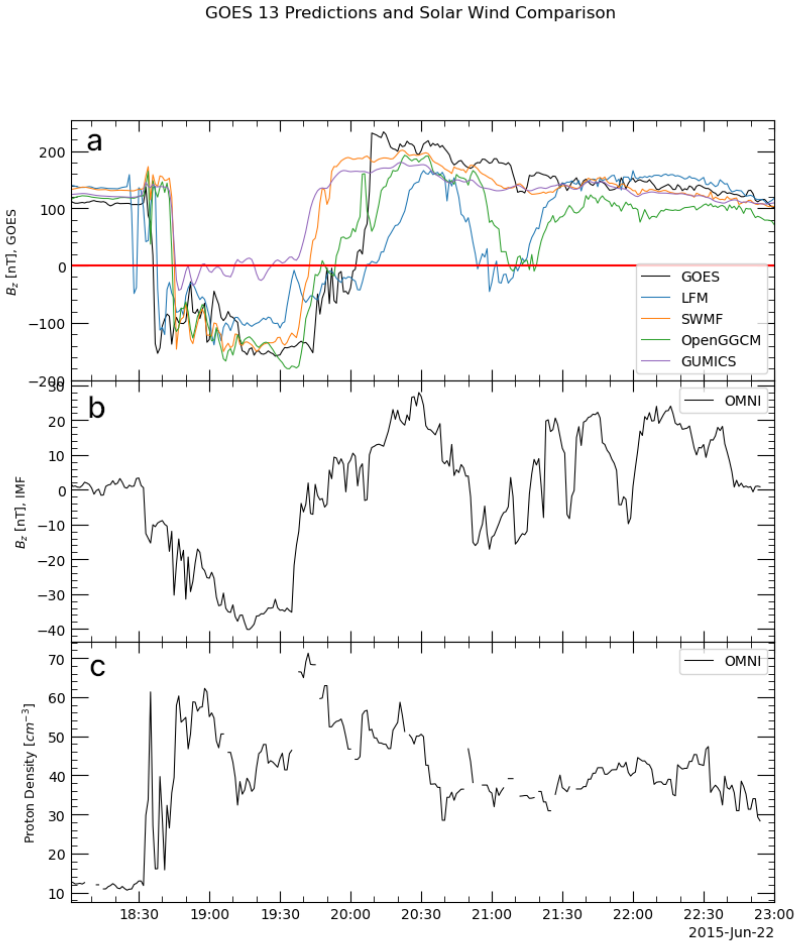

FIGURE 2.9: (a) GOES 13 predictions and observations of B_z, with (b) OMNI IMF B_z and (c) proton densities on 2015 June 22.

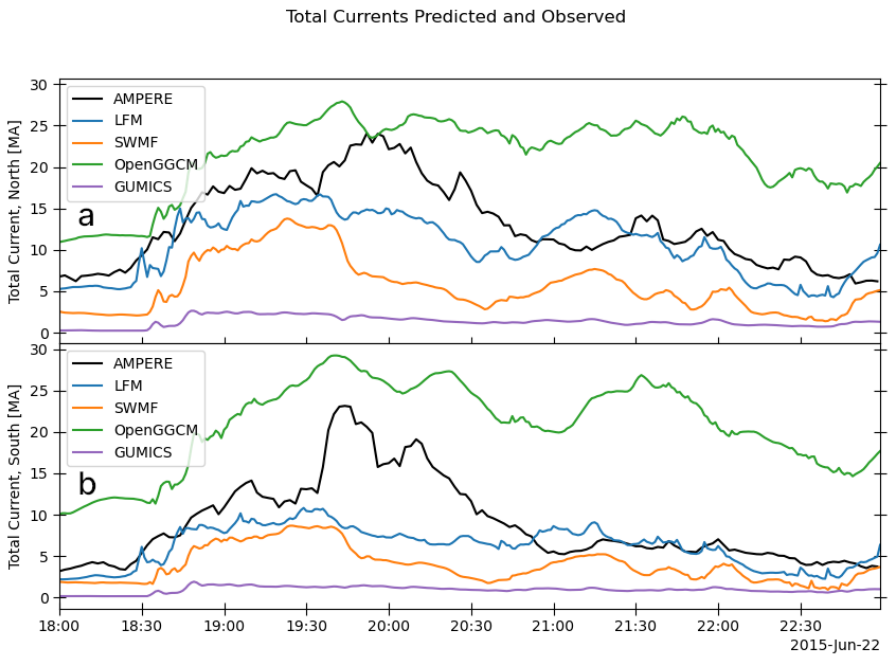

FIGURE 2.10: Total integrated field-aligned currents in the (a) northern and (b) southern hemispheres from AMPERE and as predicted by the MHD models for 2015 June 22.

cm^{-3} at 18:30 UT, accompanied by a southward turning of IMF B_z, which went from 0 nT to more than -15 nT, pushing the magnetopause all the way to geosynchronous orbit and beyond. Sustained high densities and increasingly stronger IMF B_z values that reached almost -40 nT kept GOES 13 and 15 in the magnetosheath until around 19:40 UT, when a northward turning of the IMF and a decrease in density to about 40 cm^{-3} allowed the magnetopause to move back outward again. This magnetopause motion is predicted reasonably well by the models, although the extent of the motion varies among the four simulations, as demonstrated by the differences in the timing of the predicted crossings. LFM and OpenGGCM perform the best during this part of the event, with SWMF close behind. However, around 21:00 UT, LFM and OpenGGCM predict a false crossing by GOES 13 (see Figure 2.9) in response to another change in IMF B_z at 20:50 UT, this time from 10 nT to -10 nT. There was a small jump in proton density that accompanied the 20:50 UT southward turning, but this variation was not significant compared to previous density increases and decreases. The integrated Birkeland currents for the event are shown in Figure 2.10. At 20:50 UT, the time of the reversal of IMF B_z, the currents in LFM and SWMF increase, with those in OpenGGCM increasing a few minutes later around 21:10 UT, while the AMPERE currents are decreasing, especially in the northern hemisphere. The currents in the models are responding more strongly to IMF B_z than the real currents did in this event.

All the predicted crossings not due to incorrect solar wind input in the other two events, 2011 August 5 and 2017 September 7, can be explained in the same

manner. Magnetopause motion driven primarily by increases of solar wind density tends to be modeled reasonably well, while strong southward IMF B_z values cause the models, in particular LFM and OpenGGCM, to overpredict the inward motion of the boundary. Moreover, the simulated integrated Birkeland currents during the false crossings do not match the integrated currents seen in the AMPERE dataset.

2.5.3 Adding a Ring Current Model

Running LFM and SWMF coupled to the Rice Convection Model adds the effect of ring current physics, which is particularly important during geomagnetic storms. For 2011 September 26, including the ring current greatly improves the LFM predictions and, to a lesser extent, those of SWMF, apart from the false crossings caused by discrepancies in the solar wind densities between 15:40 and 17:00 UT mentioned in Section 2.5.2. The total current flowing into and out of the ionosphere is shown in Figure 2.11, which compares the AMPERE integrated FACs with those predicted by LFM and SWMF, both with and without the ring current. The LFM run that included the ring current predicts the currents much better than the original run; as a result, the predictions of magnetopause crossings at the GOES locations are more accurate throughout the period shown in Figure 2.11. The ring current coupling helps SWMF as well, but throughout the event the predicted integrated field-aligned currents are much weaker than the real currents, especially in the northern hemisphere, and the model does not predict any magnetopause crossings.

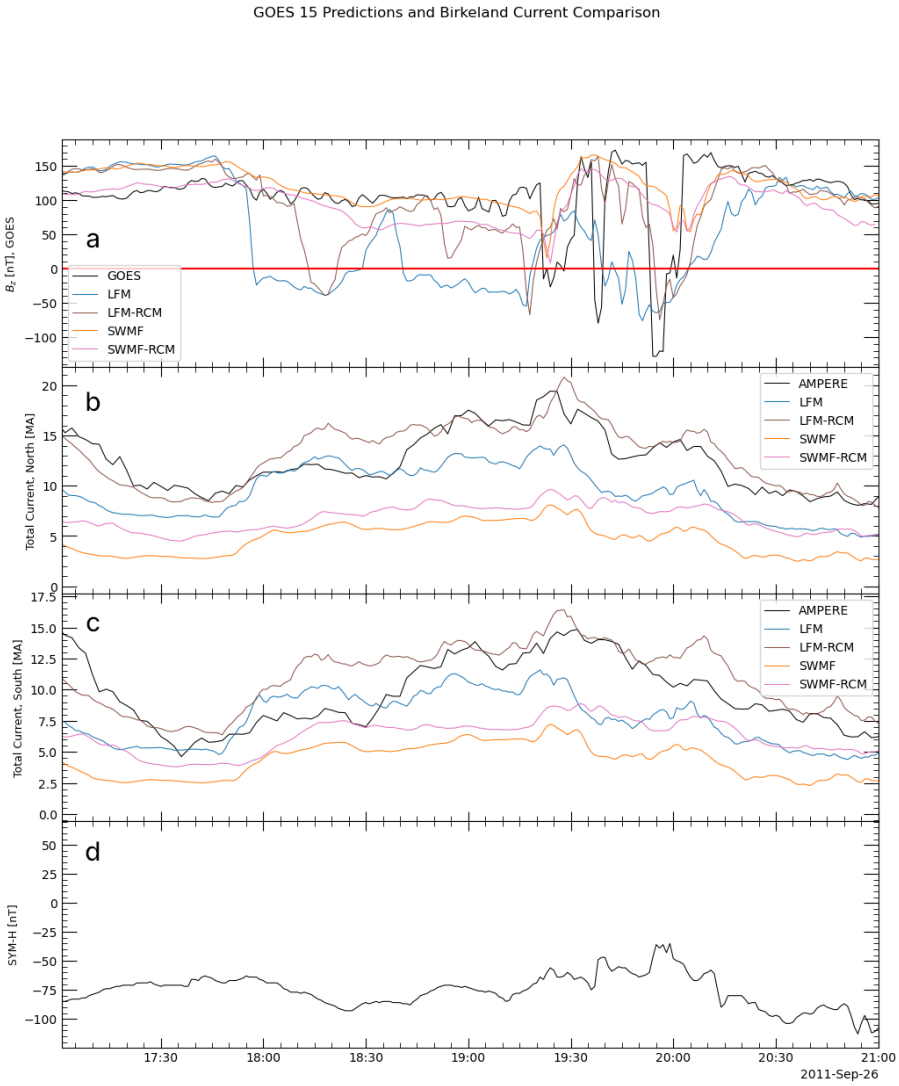

FIGURE 2.11: From top to bottom: (a) GOES 15 observations and the corresponding predictions of B_z from LFM and SWMF, with and without RCM; (b) total integrated FACs into the northern hemisphere from AMPERE and the models; (c) total integrated FACs into the southern hemisphere from AMPERE and the models; (d) real SYM-H during the 2011 September 26 event.

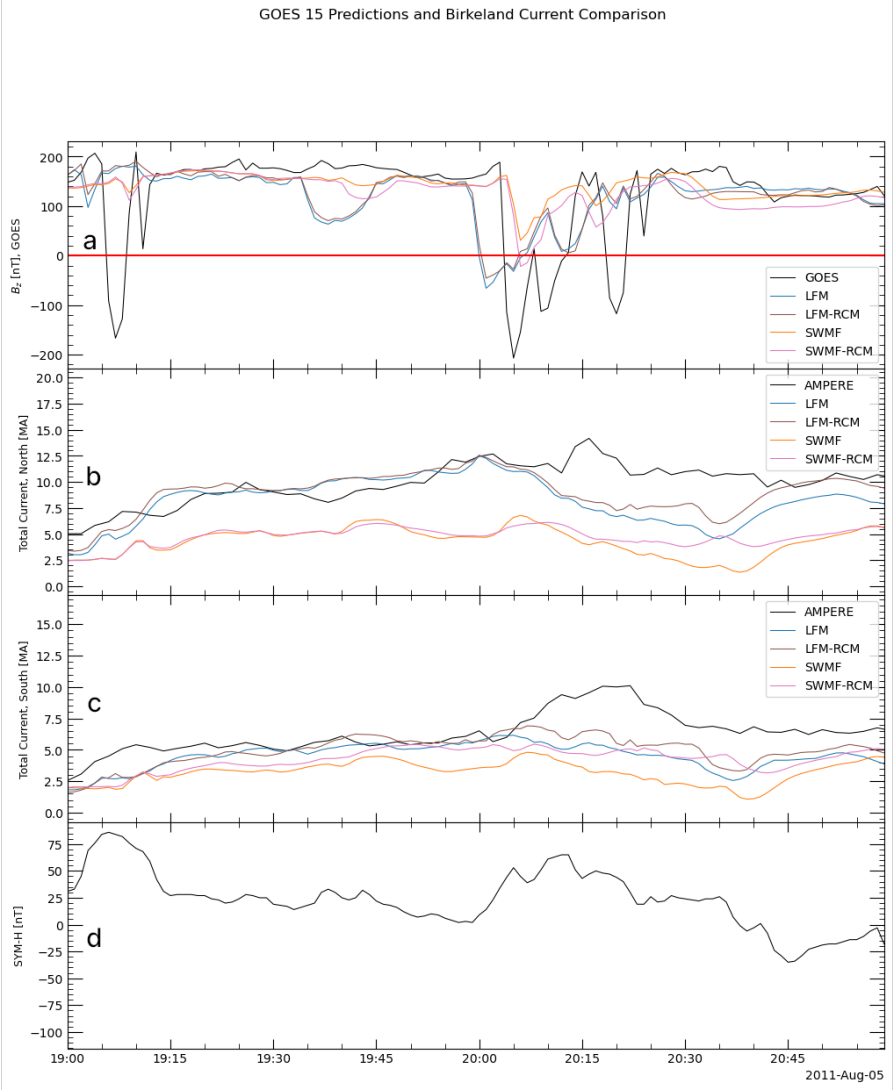

FIGURE 2.12: Same as Figure 2.11, but for 2011 August 5. The real ring current had not yet become strong during the time of the magnetopause crossings.

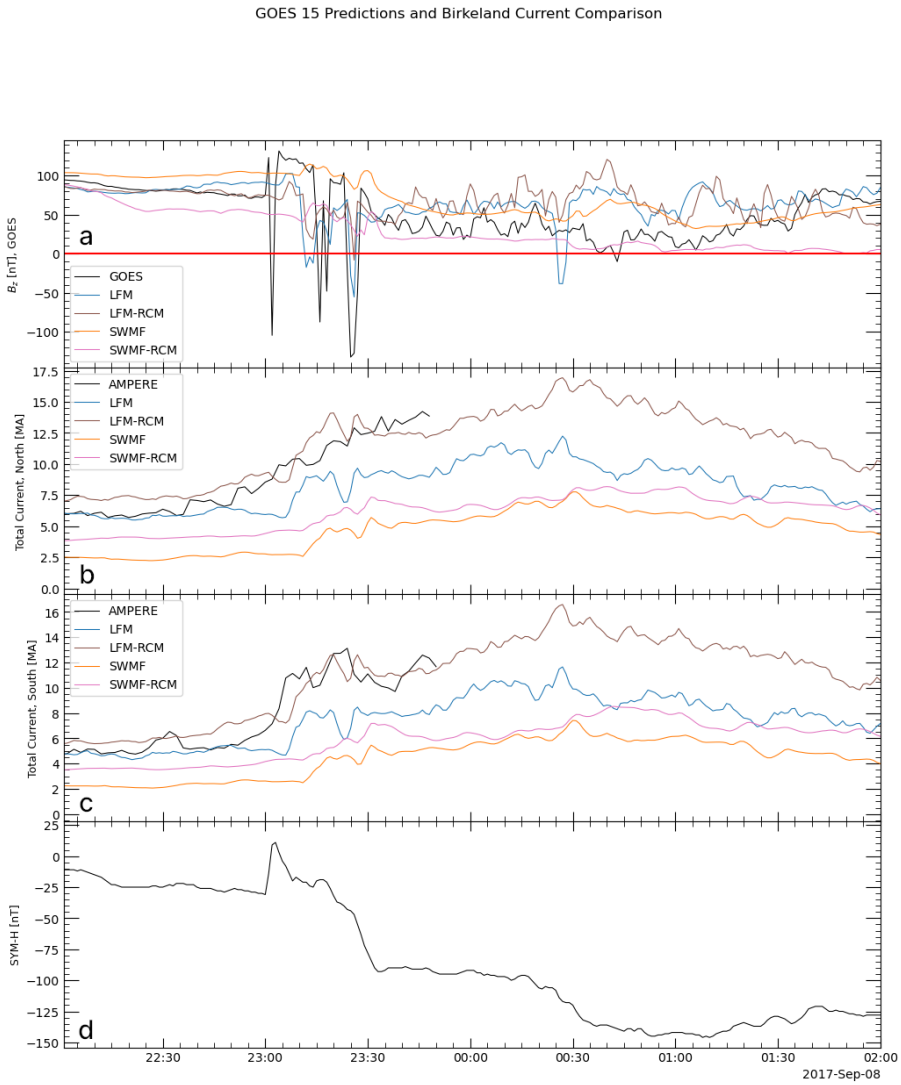

FIGURE 2.13: Same as Figure 2.11, but for 2017 September 7-8. AMPERE data (panels b and c) are not available for 2017 September 8. The real ring current had not yet become strong during the time of the magnetopause crossings.

The storm on 2011 August 5 responds similarly to the addition of the ring current. The LFM predictions improve at both of the two GOES locations and for the integrated Birkeland currents, although the simulation still underpredicts the periods of strongest current, i.e. between 20:00 and 20:45 UT. SWMF with the ring current predicts one of the GOES 15 crossings at 20:10 UT, which before it had missed, but the SWMF values for the integrated Birkeland currents, while stronger with RCM than without, are still in general significantly lower than the AMPERE values, especially in the northern hemisphere (see Figure 2.12). The effect of including ring current physics is not as pronounced during this event for either LFM or SWMF as it is during the 2011 September event; this is, however, expected because the period of interest for the August event is early in the storm, before any significant decrease in SYM-H and, hence, before a strong ring current had time to form in real life. The crossings during the 2017 September 7 storm also take place before the real SYM-H becomes strongly negative, so RCM has little effect on the predictions at the location of GOES 15 between 23:00 and 23:30 UT. The later spurious crossing in LFM, right before 00:30 and further into the storm than the real crossings, is removed, but SWMF still misses the real crossings altogether (Figure 2.13).

The results of the LFM-RCM and SWMF-RCM runs for the 2015 June 22 storm do not display the expected effect of the ring current. With some small improvements, the predictions at the GOES locations are largely similar to those from the runs without the ring current. The integrated Birkeland current magnitudes are somewhat improved, but the models still miss the peak in the southern hemisphere current around 20:00 UT. Additionally, adding RCM does not

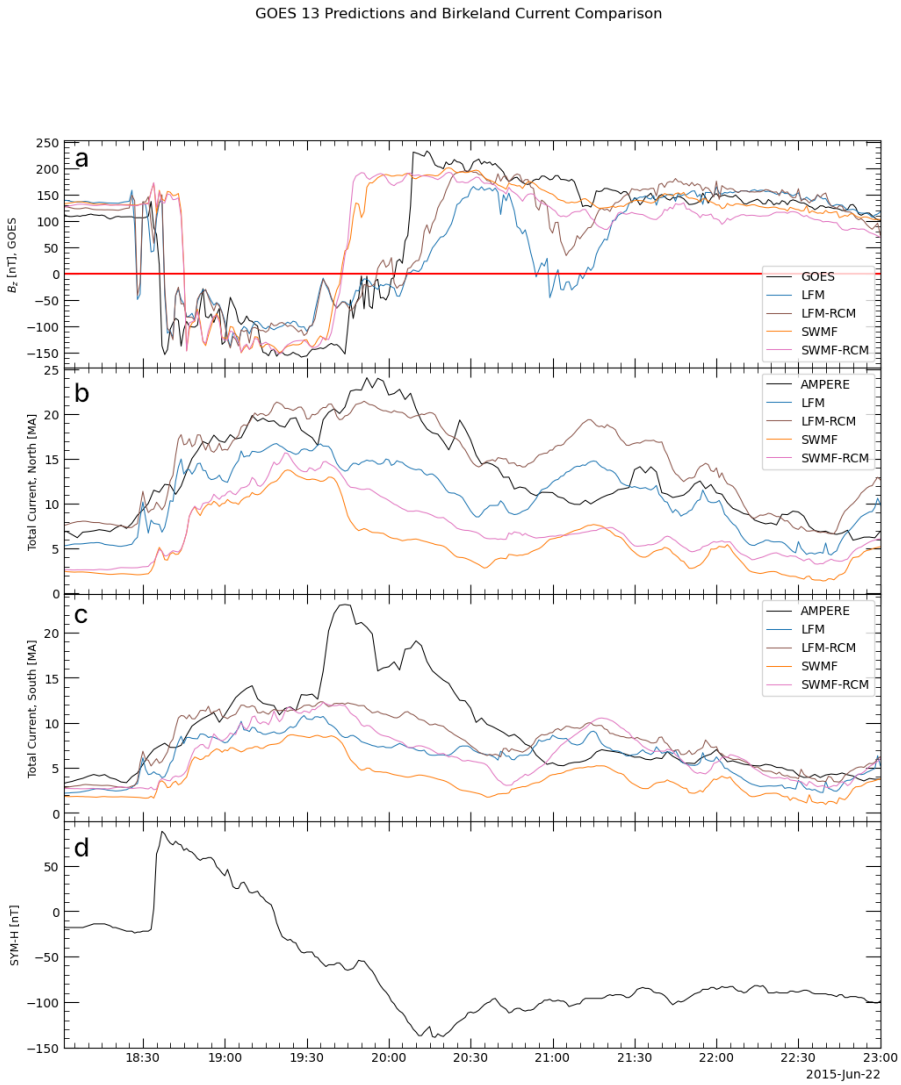

FIGURE 2.14: Same as Figure 2.11, but for GOES 13 on 2015 June 22. Although during the beginning of the real crossing the ring current is weak, as indicated by the positive SYM-H (panel d), it is strong by 19:30 UT.

remove the increase in the currents of both hemispheres predicted shortly after 21:00 UT and corresponding with spurious GOES crossings in LFM, although it does, barely, remove the crossing in GOES 13, as shown in Figure 2.14.

2.6 Discussion

The inhomogeneous nature of the solar wind (Borovsky, 2008) means that plasma features and IMF observed near L1 do not necessarily reach the magnetosphere. Even for events without multiple solar wind observations, discrepancies can sometimes be confirmed by means of fortuitously placed ground magnetometers. The first event discussed in Section A 2.5.1 is an example of such a situation. The H, Z, and F components of the Honolulu magnetometer, which was near local noon during the period of interest, responded to the density increases at 19:00 and at 20:00 UT with increases of their own, but record only a very small reaction to the 19:40 density pulse seen in the OMNI data (Figure 2.15), supporting the conclusion that the pulse either did not reach Earth or was much smaller than the one observed at L1. This is a well-known issue (Merkin et al., 2013), yet space weather forecasts must for the time being rely on point observations at L1 to characterize the solar wind. Since discrepancies large enough to significantly change predictions of magnetopause position exist in three out of four of the events here considered, it would be useful to have a quantitative idea of the probability that the solar wind in the OMNI dataset does not represent the solar wind that impacts the bow shock. A possible approach to such a study would compare OMNI data to observations from spacecraft like THEMIS B/C

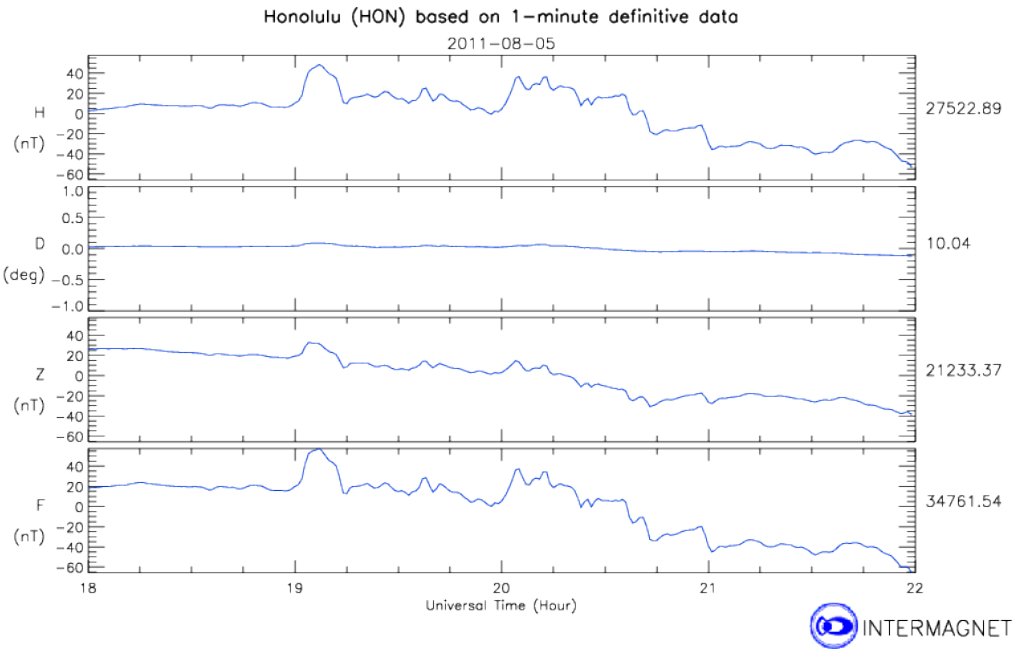

FIGURE 2.15: Magnetometer data from the Honolulu station. There is no real response to the 19:40 UT density pulse seen in OMNI, which suggests that the pulse did not reach Earth (plot from Intermagnet).

or Geotail, during periods when they are near the Earth-Sun line, to calculate the correlation of the two datasets.

Inaccuracies in the prediction of the integrated field-aligned currents reduce the models' reliability when the magnetopause moves because of erosion of Earth's magnetic field. The investigations of the response of the MHD codes to southward turnings in the IMF have here been restricted to the consideration of the effect of the ring current on the integrated Birkeland current predictions, but the nature of the modeled ionosphere must play a role as well. Further studies should consider the results of coupling more sophisticated ionosphere models to LFM and OpenGGCM or even of setting a range of constant Pedersen

conductances for repeated simulation runs.

Including ring current physics tends to improve storm-time predictions of magnetopause location, especially when the movements of the magnetopause is caused by erosion of Earth's magnetic field due to a strong southward IMF component, but coupling RCM to the MHD codes does not completely solve the problem. On the one hand, a significant IMF B_y component can cause interhemispheric asymmetries in the ionosphere which may not necessarily be reproduced in the models, since MHD models coupled to RCM only couple the northern hemisphere to the ring current (Pembroke et al., 2012; Zeeuw et al., 2004). Introducing IMF B_y changes the location of the ring current, moving it away from the equatorial plane either north or south, depending on the sign of B_y. If the models are not capturing all the B_y effects, the simulated ring current may not be in the correct location. Such an inaccuracy could particularly affect predictions in the +Y sector, where the asymmetric inflation of the ring current can influence the location of the magnetopause.

During the storm of 2015 June 22, after 19:35 UT, the IMF had a very strong positive B_y component for several hours, during which time LFM predicted false magnetopause crossings by both GOES 13 and 15 (Figure 2.16 Y). Adding the ring current to the LFM predictions removes the actual 21:00 UT crossing at GOES 13, but the simulated satellite still approaches the boundary too closely. At this time, GOES 13 was well into the afternoon sector, so the ring current should have had a greater influence on magnetopause location in the region through which the spacecraft was passing. It seems possible that the large IMF

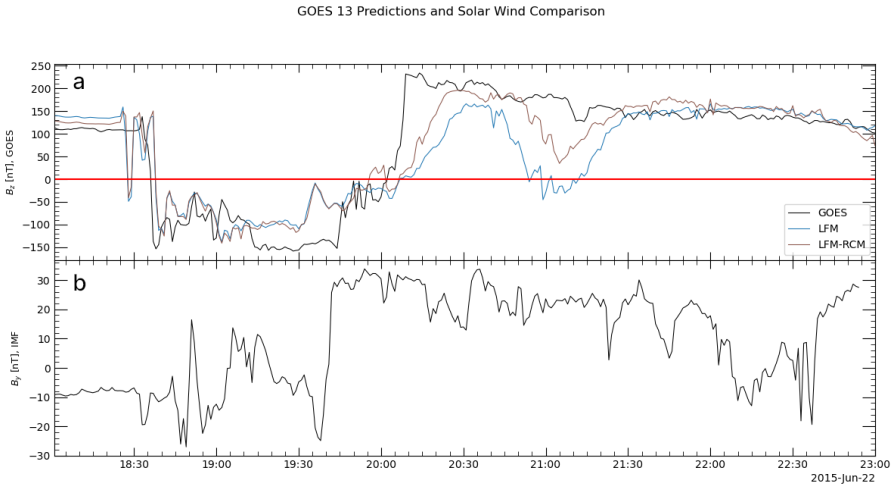

FIGURE 2.16: (a) GOES 13 observations of B_z and the corresponding predictions by LFM and LFM-RCM, on 2015 June 22, with (b) OMNI IMF B_y. During the time of the spurious crossing predicted by LFM, the IMF had a very strong, positive B_y component.

B_y at the time was causing effects in the real magnetosphere that were not reproduced in the simulation, perhaps resulting in a modeled ring current distribution that had some significant differences with reality.

2.7 Conclusions

In Part 1 of this study, eight events with strong solar wind conditions were selected and modeled with four different MHD codes. GOES 13 and 15 data were compared with simulation results at the GOES positions to analyze the ability of the models to predict magnetopause motion. Based on the results of the simulations, we calculated several different metrics for all four models. Taken

together, the various scores indicate that LFM and OpenGGCM tend to overpredict magnetopause motion, while the SWMF and GUMICS tend to underpredict. In Part 2 of this study, we considered four events during which the magnetopause moved in past geosynchronous orbit and was observed by at least one of the GOES satellites. There are two main causes of mistakes in the predictions. Firstly, the exact solar wind observed near the first Lagrange point does not always reach the magnetosphere, so using it as input for magnetosphere simulations can lead to false predictions of magnetopause motion. Secondly, although the models accurately predict the response of the magnetopause to changes in solar wind density, they sometimes struggle to calculate the Birkeland currents; this can lead to incorrect predictions of the erosion of Earth's magnetic field and the consequent motion of the magnetopause. The chances of correctly predicting magnetopause location during a storm are significantly improved by using a ring current model.

Chapter 3

Magnetopause Location During a Storm and a Quiet Period

3.1 Abstract

Magnetopause location is an important prediction of numerical simulations of the magnetosphere, yet the models can err, either under-predicting or over-predicting the motion of the boundary. This study compares results from two of the most widely used magnetohydrodynamic (MHD) models, the Lyon-Fedder-Mobarry (LFM) model and the Space Weather Modeling Framework (SWMF), to data from the GOES 13 and 15 satellites during the geomagnetic storm on June 22, 2015, and to THEMIS A, D, and E during a quiet period on January 31, 2013. The models reproduce the magnetopause crossings of the spacecraft during the storm, but they also predict spurious magnetopause motion after the crossings seen in the GOES data. We investigate the possible causes of the over-predictions during the storm and find the following. First, using different ionospheric conductance models does not significantly alter predictions of

magnetopause location. Second, coupling the Rice Convection Model (RCM) to the MHD codes improves the SWMF magnetopause predictions more than it does the LFM predictions. Third, SWMF produces a stronger ring current than LFM does, both with and without RCM and regardless of the LFM spatial resolution. During the non-storm event, LFM predicts the THEMIS magnetopause crossings due to southward interplanetary magnetic field better than the SWMF. Additionally, increasing the LFM spatial grid resolution improves the THEMIS predictions, while increasing the SWMF grid resolutions does not.

N.B. The text in this chapter has been taken entirely from Dredger et al. (2023c), which is in preparation and will soon be submitted. This chapter references the work in Chapter 2 but can be read on its own, as much of the scientific background and methodology are repeated here.

3.2 Introduction

The magnetopause is the boundary between the magnetosphere and the shocked solar wind in the magnetosheath. The location of the magnetopause is, to first order, determined by the balance of pressures from the magnetosphere and the magnetosheath; the former is dominated by magnetic pressure from Earth's magnetic field, which is much stronger than the turbulent interplanetary magnetic field (IMF) in the sheath, and the latter by pressure from the shocked solar wind plasma (Martyn, 1951). Since the position of the boundary depends on these pressures, it varies with solar wind conditions. As the IMF and the plasma parameters change, so does the overall pressure from the magnetosheath.

Under southward IMF, the magnetopause moves inward toward Earth in a process known as magnetopause erosion (Aubry et al., 1970). In the magnetosphere, large-scale currents can create fringe magnetic fields opposite to the terrestrial magnetic field, reducing the outward magnetic pressure and allowing the magnetopause to retreat Earthward. These currents include the Region 1 Birkeland or field-aligned currents (FACs) and the cross-tail current, which increase with large negative IMF B_z (Maltsev et al., 1996; Maltsev & Lyatsky, 1975; Sibeck et al., 1991; Wiltberger et al., 2003). The conductance of the polar ionosphere varies spatially and temporally with the number of charge carriers available, i.e. ionospheric plasma, and plays a major role in determining the strength of the Birkeland currents.

The ring current can also play a part in the location of the magnetopause during geomagnetic storms. As the plasma densities in the inner magnetosphere increase with ring current strength, they push the magnetopause outward, especially in the post-noon sector with the partial ring current. The toroidal geometry of the ring current creates a weak magnetic field outside itself in the direction of the terrestrial magnetic field, which strengthens the outward magnetic pressure on the magnetopause. The partial ring current is created as particles are lost to magnetopause shadowing, when the drift paths of ions in the inner magnetosphere intersect the magnetopause as it moves inward (Kang et al., 2018) and closes into the ionosphere with the Region 2 Birkeland currents. The asymmetry due to the partial ring current causes the post-noon magnetopause to be pushed out farther than the pre-noon magnetopause (Dmitriev et al., 2011). SYM-H is an index that measures the deviation of the magnetic field at Earth's surface from

its quiet time value, due in large part to the increased strength of the ring current during geomagnetic storms, using magnetometer stations around the world.

Numerical simulations of various kinds are used to predict magnetopause location, with physics-based codes generally outperforming empirical models. For operators of satellites in an orbit that can be either inside or outside the magnetopause, depending on conditions, predictions of magnetopause motion represent an important space weather product. Spacecraft attitude adjustment by means of magnetic torquing, for example, must take into account the differences in the magnetic field inside the magnetosphere and outside in the magnetosheath (Sibeck, 1995). Additionally, the ability of a model to accurately predict the location and shape of the magnetopause indicates, on some level, the extent to which the physics of the solar wind-magnetosphere interaction is represented in the code. An awareness of the strengths and weaknesses of the different codes is therefore vital to understanding the appropriateness of each model under various solar wind conditions. Previous work discussed in Chapter 2 found that, in general, magnetohydrodynamic (MHD) models tended to predict the position of the magnetopause better when the main driver of its motion was a density increase, while a southward IMF turning, unaccompanied by stronger solar wind plasma pressure, often resulted in an overprediction of magnetopause erosion, at least during geomagnetic storms. The same study also saw an overall improvement in the prediction of magnetopause location with the coupling of an inner magnetosphere model that adds ring current physics to the simulation.

This study builds on the work of Chapter 2 by further investigating one of the four storms considered in that paper, the storm of June 22-23, 2015, with

two different MHD models. We study the effects of changing the ionospheric conductance model on the prediction of Birkeland current magnitude and magnetopause location. We also consider in detail the results of coupling an inner magnetosphere model to both of the MHD codes during the June 2015 storm. Finally, as a counterexample to the investigation of the storm event, we compare the ability of the two models to predict the location of the magnetopause during a period of quiet solar wind and weak IMF. For both storms, we investigate the effect of changing the spatial grids of the MHD models on the predictions along the satellite tracks.

3.3 Methodology

The spacecraft providing the data for this study are the geosynchronously orbiting GOES 13 and 15, operated by NOAA, and three THEMIS satellites, A, D, and E. GOES 13 orbits Earth at 75° West, four hours local time ahead of GOES 15 at 135° West. Each set of GOES magnetometer data is given in a cylindrical coordinate system in which the z-component, labeled HP, roughly corresponds with the Z-component in geocentric solar ecliptic (GSE) coordinates. THEMIS (Time History of Events and Macroscale Interactions During Substorms) is a constellation of five spacecraft, two of which, B and C, have been moved to lunar orbit and comprise the THEMIS-ARTEMIS mission. The three spacecraft used in this study orbit Earth in an elliptical orbit that precesses from the dayside to the magnetotail and back again (Angelopoulos, 2008). THEMIS data is given in GSE coordinates.

We identify a magnetopause encounter in the satellite data as the moment when the magnetometer measures $B_z = 0$ nT in the ambient magnetic field, as the spacecraft passes from positive, near-dipolar values inside the magnetosphere to the turbulent, negative IMF B_z in the magnetosheath. This method, of course, only works for southward IMF conditions, like those during a geomagnetic storm. While it is possible that solar wind density alone can push the magnetopause in past geosynchronous orbit under northward IMF B_z, the density must be so strong that such a situation only occurred twice in the entire decade of 2010-2020 for a total of 30 minutes (Collado-Vega et al., 2023). In this paper we directly compare the observational satellite data with the model predictions along the satellite track, so the exact timing of the magnetopause crossings themselves is less important.

The solar wind data used to drive the MHD simulations come from OMNI, a dataset that takes measurements from several solar wind monitors and propagates them to a nominal bow shock position. During both events here considered, Wind was providing the observations to OMNI; Wind orbits the first Lagrangian point, about 200 R_E upstream of Earth. OMNI data are available as one- and five-minute averages and the one-minute averaged data were used in the model runs. Another dataset from the Active Magnetosphere and Planetary Electrodynamics Response Experiment (AMPERE) provides the Birkeland current measurements in this study. AMPERE uses the engineering magnetometer data from the Iridium satellite constellations to derive FACs (Anderson et al., 2014; Anderson et al., 2002).

The two MHD models employed in this study are the Lyon-Fedder-Mobarry

(LFM) model and the Space Weather Modeling Framework (SWMF) from University of Michigan, both very successful codes with a long history. All simulation runs were conducted at NASA's Community Coordinated Modeling Center (CCMC).

LFM solves the semiconservative MHD equations on a stretched spherical grid (Lyon et al., 2004). The single-fluid version implemented at the CCMC offers three different levels of resolution (r x theta x phi): 53x48x64, 106x48x64, or 106x96x128 cells. Unless otherwise specified, all LFM runs in this study have the lowest resolution, known as "double" resolution (e.g. Hogan et al., 2020; Pham et al., 2021; Pham et al., 2016). The ionospheric electrostatic potential is calculated by the builtin Magnetosphere-Ionosphere Coupler/Solver (MIX), a 2D shell around Earth at the MHD inner boundary (Merkin & Lyon, 2010). There are various options for conductance models including constant Pedersen and Hall conductances and a semi-empirical auroral conductance (Wiltberger et al., 2009). MIX can also couple LFM to the Thermosphere-Ionosphere-Electrodynamic General Circulation Model (TIEGCM), a first-principles model of the ionosphere-thermosphere system (Dickinson et al., 1981; Qian et al., 2014; Roble et al., 1988). LFM-MIX together with TIEGCM is called the Coupled Magnetosphere Ionosphere Thermosphere model, or CMIT (Liu et al., 2021; Wang et al., 2004; Wiltberger et al., 2004).

The SWMF executes and couples a set of models in different space physics domains (Tóth et al., 2005; Tóth et al., 2012). The MHD code employed in the SWMF is the Block-Adaptive-Tree-Solarwind-Roe-Upwind-Scheme (BATS-R-US), which solves the conservative MHD equations on an adaptive 3D grid to

simulate the global magnetosphere (Powell et al., 1999). Ionospheric electrodynamics are calculated by the Ridley Ionosphere Model (RIM) at about 110 km in altitude (Ridley et al., 2004; Ridley et al., 2001; Ridley & Liemohn, 2002). At the CCMC, there are several options given for the conductance model which are similar to those available for LFM: constant conductance and semi-empirical auroral conductance (Ridley et al., 2004). The grid used for most of the runs in this study is the overview grid with 1,007,616 cells, abbreviated as "1M" below, which is similar to the lower resolution of the two used in the version of the code at NOAA's Space Weather Prediction Center (SWPC). For the analysis of the non-storm event, we ran the SWMF with a high-resolution grid of 9,623,552 cells, abbreviated as "9M".

The Rice Convection Model (RCM) is a bounce-averaged drift kinetic model developed at Rice University and is widely used to simulate the inner magnetosphere, both as a standalone model and coupled to magnetosphere models to add the effect of the ring current (Toffoletto et al., 2003; Wolf et al., 1982). LFM can be coupled to RCM (Pembroke et al., 2012), although the version of LFM currently implemented at the CCMC does not allow the MHD code to be coupled to both RCM and TIE-GCM at the same time. The SWMF has also incorporated RCM into its Inner Magnetosphere (IM) module (Tóth et al., 2005; Tóth et al., 2012; Zeeuw et al., 2004).

3.4 Results

3.4.1 Description of 2015 June 22 Storm and GOES Magnetopause Crossings

On June 22, 2015, around 18:30 UT, the proton density measured at L1 suddenly increased from about 10 cm^{-3} to more than 60 cm^{-3}, accompanied by a steep increase in solar wind speed and intense IMF values. B_z remained strongly southward for almost an hour and a half and then went northward until around 21:00 UT, when it turned southward again. As B_z became positive, B_y reached more than 30 nT and stayed strongly positive for more than two hours. This was a moderate geomagnetic storm; SYM/H reached nearly -150 nT after the storm sudden commencement and did not recover until after the period under consideration in this study (see Figure 3.1). The density increase pushed the magnetopause towards Earth and over GOES 13 and 15, which were on the dayside at the time in the afternoon and morning sectors, respectively. Although proton densities remained high into the morning of June 23, the later southward turning of B_z did not cause any more magnetopause crossings at geosynchronous orbit, although both LFM and the SWMF predict false crossings at both GOES 13 and GOES 15 in response. By 21:00 UT, GOES 13 was far into the dusk sector and GOES 15 was near noon.

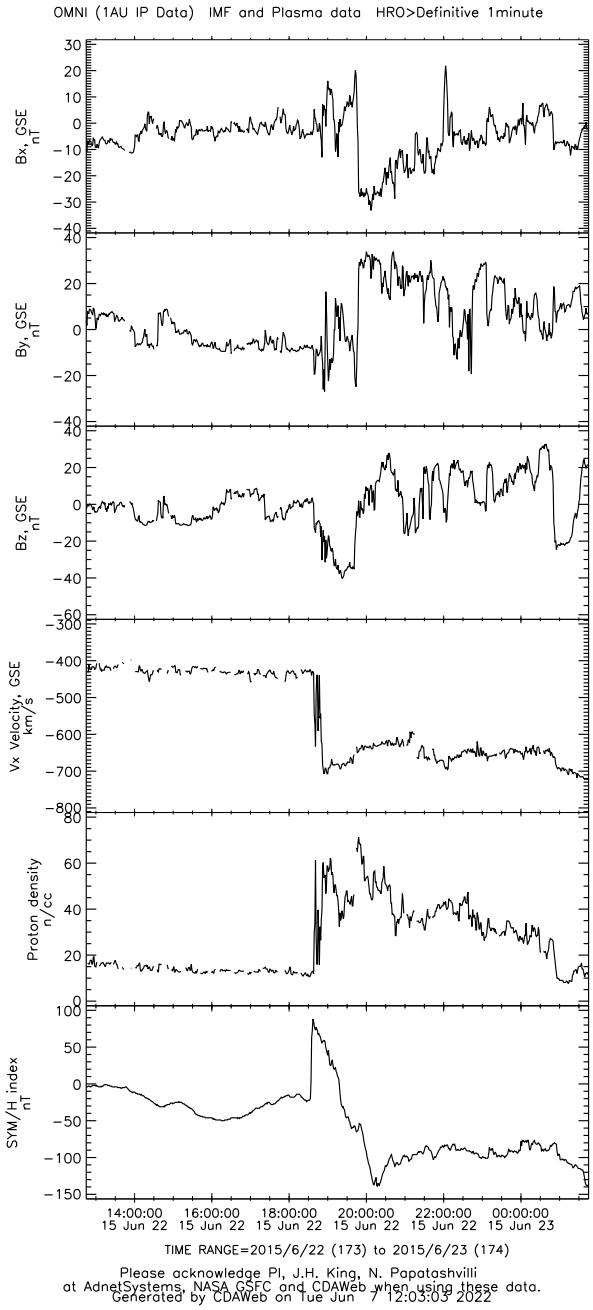

FIGURE 3.1: OMNI solar wind and SYM/H index for the duration of the MHD runs. (Plot from CDAWeb)

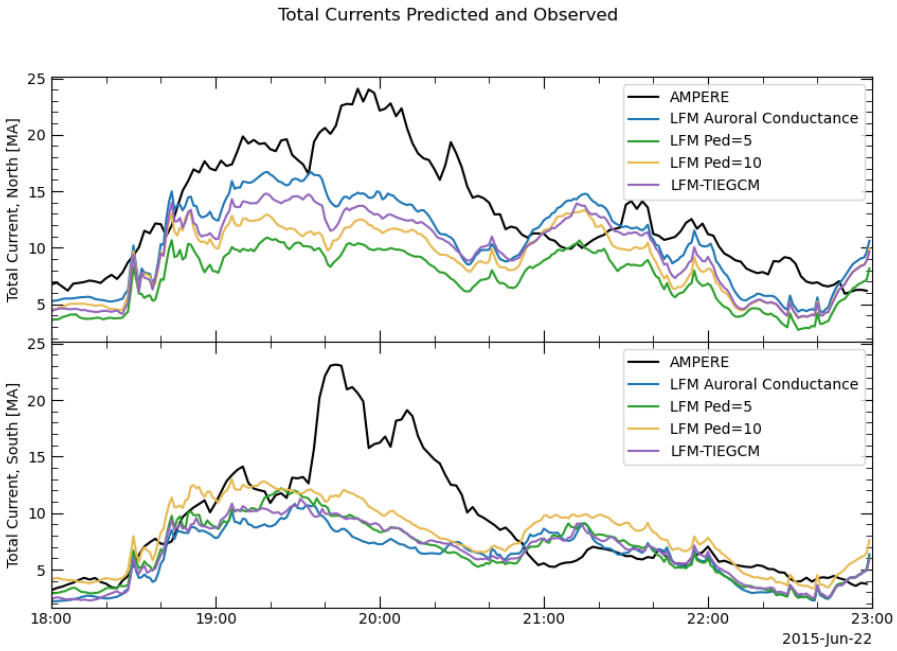

FIGURE 3.2: Total FACs in the northern and southern hemispheres, as predicted by LFM using several different ionospheric conductance models, compared with AMPERE. The predicted currents differ somewhat in magnitude but not in their temporal trends, including their prediction of an increase after 21:00 UT that is not reflected in the AMPERE currents.

3.4.2 The Effect of Ionospheric Conductance Models

The "original" runs by both MHD models use the semi-empirical auroral conductance option to calculate ionospheric conductances during the event. To investigate the cause of the spurious magnetopause crossings, the models were rerun with different conductance models.

Figure 3.2 shows the total Birkeland currents in the northern and southern hemispheres for the auroral conductance run, runs with constant Pedersen conductance of 5 and 10 S and Hall conductance set to zero, and LFM coupled to TIEGCM, all compared with the total currents from the AMPERE dataset. All of the runs fall short of the real current values, especially in the south, and all predict an increase after 21:00 UT that does not exist in the AMPERE data. The predicted currents do differ in magnitude in the north, with the auroral conductance calculation being the highest and TIEGCM close behind. All the runs completely fail to capture the peak of the current in the southern hemisphere. In the magnetosphere, the four runs predict a spurious magnetopause crossing at GOES 15, contemporary with the false increase in the total Birkeland currents. As shown in Figure 3.3, despite the difference of magnitude among the predicted currents, the predicted GOES 15 observations from all four LFM runs are almost exactly the same.

Although the SWMF does not predict spurious magnetopause crossings, the simulated GOES 15 sees two decreases in B_z around 21:00 UT and 22:00 UT that are not reflected in the real data, indicating that the magnetopause approaches the modeled satellite too closely at those times. Repeating the conductance experiment with the SWMF gives results similar to LFM. Figures 3.4 and 3.5 show

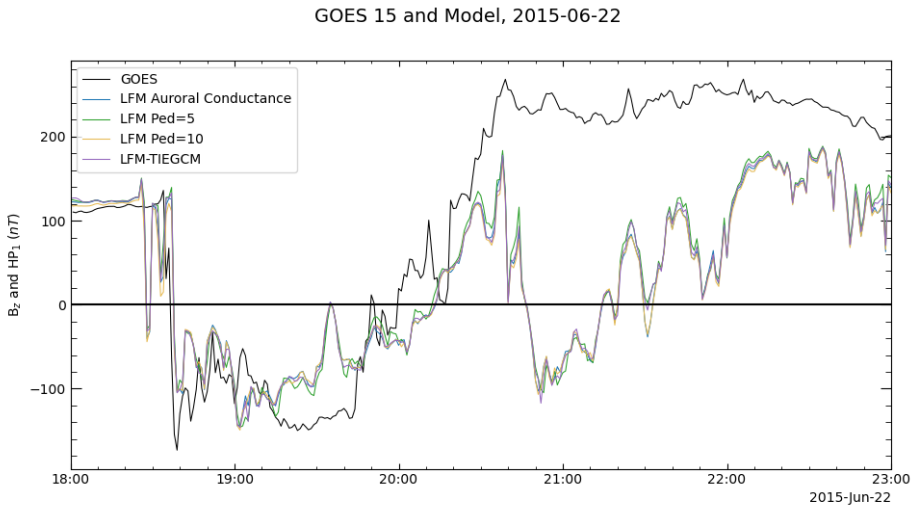

FIGURE 3.3: GOES 15 data and predictions by LFM using several different conductance models. The predictions are virtually identical among the four runs.

the total FAC and GOES 15 predictions from the SWMF with auroral conductances and with three values of Pedersen conductance, 2, 5 and 10 S. Like the corresponding LFM predictions, the currents vary in magnitude, but changing the conductance model does not change the overall shape of the lines in Figure 3.4. The four runs have virtually the same predictions at the location of GOES 15, even for the very low constant conductance run. Changing the conductance model in both LFM and the SWMF seems to have almost no effect on the predictions of magnetopause motion.

3.4.3 Results of Including RCM

Because the 2015 June 22 magnetopause crossings take place under storm-time conditions, it is reasonable to include an inner magnetosphere model such as RCM, in order to better represent the effect of the ring current. Chapter 2 presents

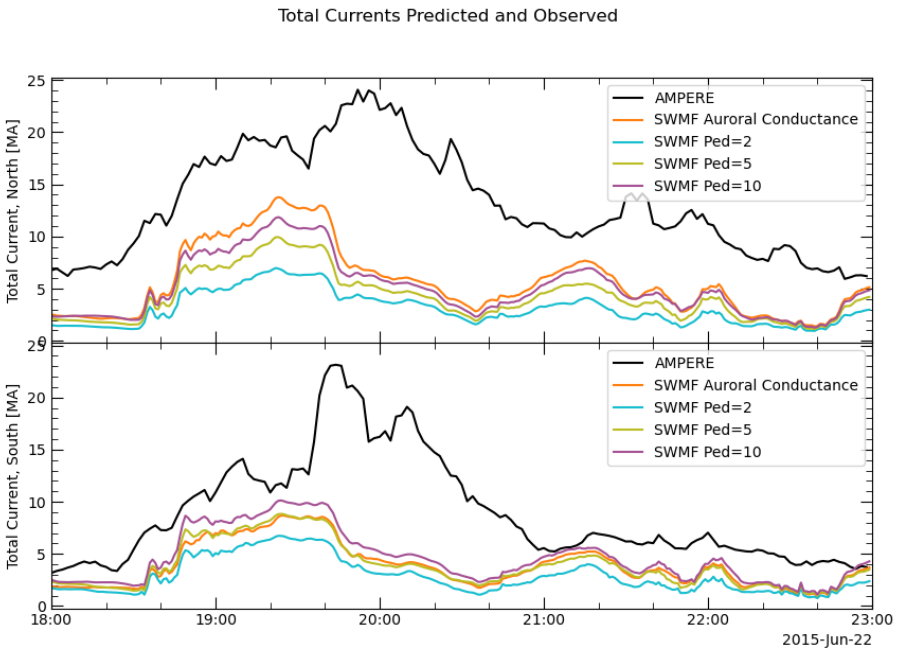

FIGURE 3.4: Total FACs in the northern and southern hemispheres, as predicted by the SWMF using several different ionospheric conductance models, compared with AMPERE. Similar to the currents in the LFM runs shown in Figure 3.2, the predicted currents differ somewhat in magnitude but not in their temporal trends, including their prediction of an increase after 21:00 UT that is not reflected in the AMPERE currents.

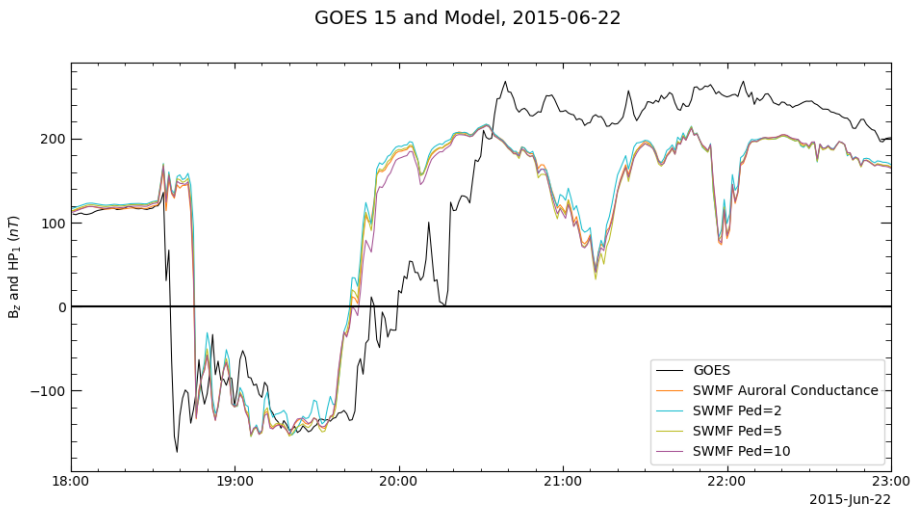

FIGURE 3.5: GOES 15 data and predictions by SWMF using three different conductance models. Once again, the predictions are virtually identical among the three runs.

the results of doing so on the Birkeland currents and GOES 13 predictions in Figure 2.14. We here summarize those results for convenience. The study in Chapter 2 found that, for LFM with RCM, the magnitude of the total FAC is improved, although the model still underpredicts the peak in the southern current, while the simulated GOES 13 no longer crosses the magnetopause. The addition of RCM does not, however, remove the spurious peak in the current at 21:00 UT, and GOES 13 still approaches the magnetopause too closely. For the SWMF with RCM, the FAC magnitudes are improved but still fall short of the AMPERE currents. In the southern hemisphere especially, the 21:00 UT false current increase is still prominent. Neither SWMF run predicted any spurious crossing of the magnetopause at GOES 13 (see Chapter 2).

Figure 3.6 shows the predictions of LFM and LFM with RCM at the GOES 15

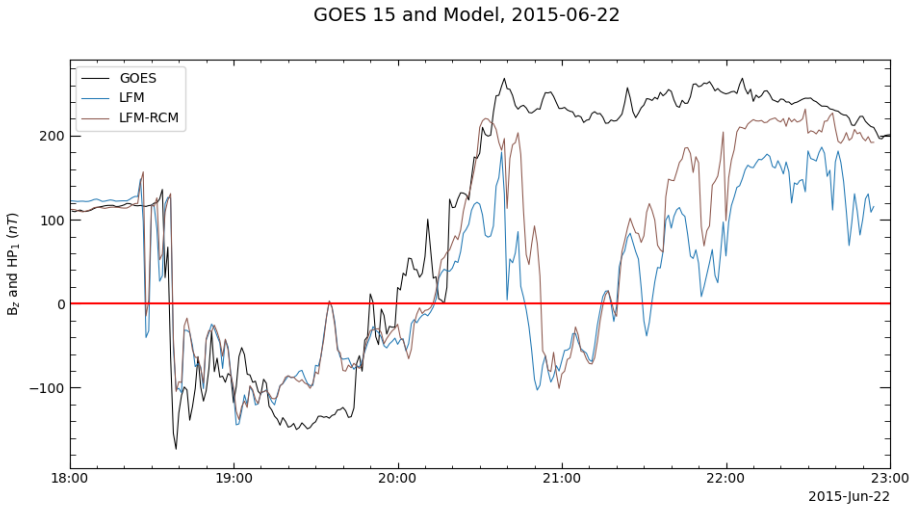

FIGURE 3.6: GOES 15 data and predictions by LFM both with and without RCM. The inclusion of RCM improves the predictions somewhat during the spurious crossings but still leaves significant differences between the real data and the predicted data.

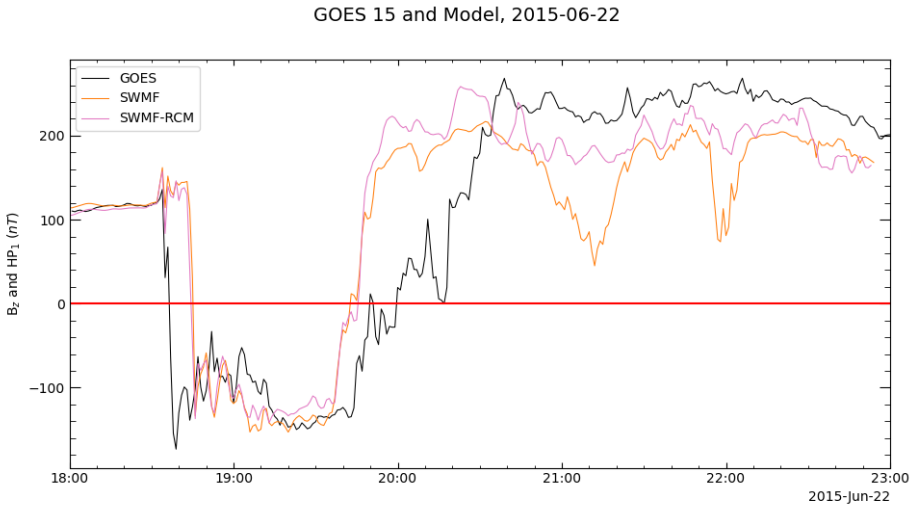

FIGURE 3.7: GOES 15 data and predictions by SWMF both with and without RCM. The inclusion of RCM removes the two false dips in B_z at 21:00 and 22:00 UT.

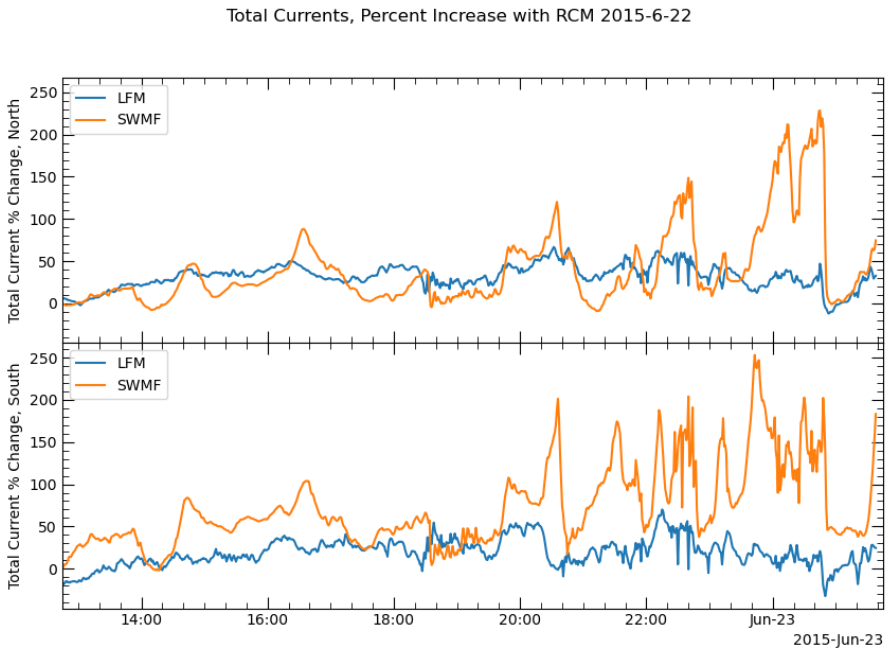

FIGURE 3.8: Percent change in total field-aligned currents between the basic MHD run and the run with the RCM coupling, for both LFM and SWMF, in the northern and southern hemispheres.

location, compared with the real GOES data. Including RCM improves the predictions slightly but does not remove the spurious crossing at 21:00 UT. SWMF with RCM also improves on the GOES 15 predictions, as seen in Figure 3.7. The original SWMF run did not predict any spurious magnetopause crossings at GOES 15, but it did predict two magnetopause approaches, as shown by the two decreases in predicted B_z at 21:00 and 22:00 UT. Those two false dips in B_z are removed in the RCM run.

The addition of the RCM coupling increased the total FACs for both models, but the percent change for the SWMF run was much more significant than for LFM. Figure 3.8 shows the percent change in total FACs in both the northern and

southern hemisphere for the two models. LFM-RCM reaches a 50% increase at times throughout the run, while SWMF with RCM shows increases of more than 200% from the basic MHD run. The SWMF FAC increase is most prominent in the southern hemisphere.

The best way to compare the strength of the ring current calculated by LFM and SWMF with RCM would be to compare a predicted SYM-H index from both models; LFM, however, does not include this as an output at the CCMC. In order, therefore, to perform this comparison, we take the strength of B_z at X = 3.5 R_E, Y = Z = 0 R_E, a value which scales with ring current strength since Earth's magnetic field points northward at that location. The results are shown in Figure 3.9. The decrease in B_z starting around 18:30 UT corresponds to the intense IMF that reached the magnetosphere at the same time. We can see that the SWMF responds more quickly to the change in solar wind conditions than does LFM, while also predicting a bigger decrease in B_z. The difference between the two MHD runs and their corresponding RCM runs is much greater for the SWMF than for LFM, especially during the big B_z dip.

The spatial resolution of the simulation grid for the LFM runs shown in Figure 3.9 is significantly lower than that of the SWMF runs to which they are compared. The size of LFM cells near geosynchronous orbit for the double resolution runs is about 0.4 R_E in each direction, while that of the corresponding SWMF cells for the 1M resolution is 0.25 R_E. The larger LFM grid cells could be causing the model to calculate weaker pressure gradients in the inner magnetosphere, and thus a weaker ring current. To investigate this possibility, the LFM runs were repeated at the two higher resolutions available at the CCMC

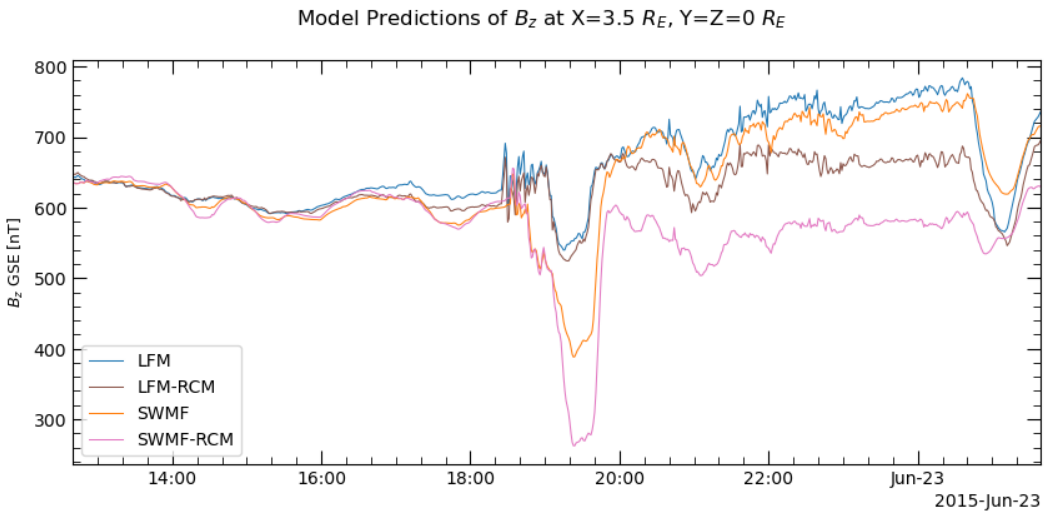

FIGURE 3.9: B_z at X = 3.5 R_E along the Earth-Sun line for LFM and SWMF, both with and without RCM, providing a comparison of ring current strength among the various simulation runs. Both SWMF runs calculate a stronger ring current than LFM; the difference between LFM and LFM with RCM is much less than the difference between the SWMF with and without RCM.

and those results were compared with the original LFM-RCM and corresponding SWMF runs. Figure 3.10 shows that even as the LFM resolution is increased, the calculated strength of B_z at X = 3.5 R_E changes very little. When RCM is included in the SWMF, the predicted ring current is much stronger than it is for LFM coupled to RCM.

Increasing the spatial resolution of the LFM grid also has very little effect on the predictions of B_z at the GOES 15 location. Figure 3.11 shows the data and predictions from the three LFM-RCM runs along the GOES 15 track. There are no significant differences between the three runs: GOES 15 still crosses the magnetopause shortly before 21:00 UT, when the real satellite was far from the boundary.

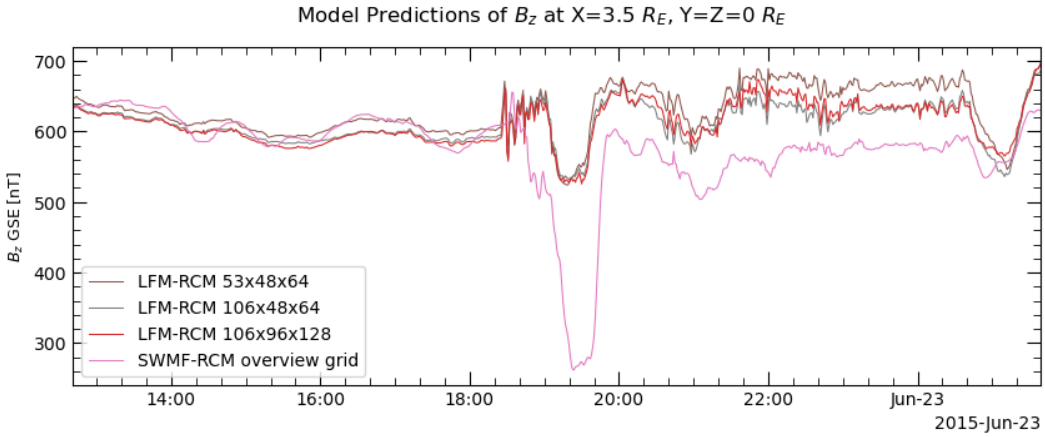

FIGURE 3.10: B_z at X = 3.5 R_E along the Earth-Sun line for LFM-RCM at three different resolutions and SWMF with RCM, providing a comparison of ring current strength among the various simulation runs. Even as the spatial resolution of the LFM grid approaches that of the SWMF run, the LFM predictions of B_z do not change by much and remain much higher than the SWMF predictions.

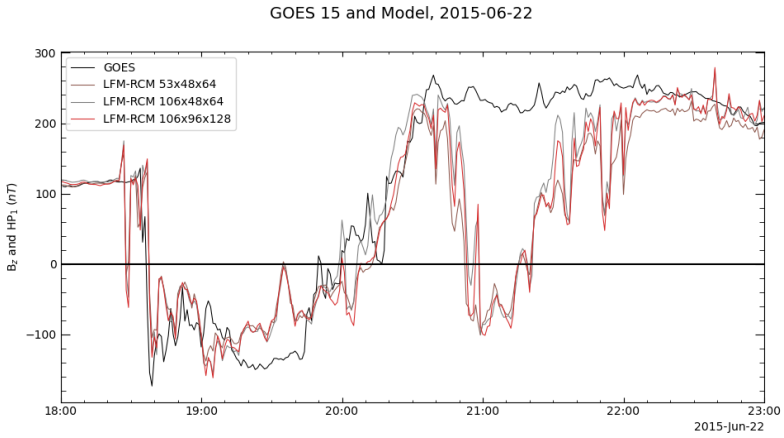

FIGURE 3.11: GOES 15 data and predictions from LFM-RCM at three different resolutions. Increasing the spatial resolution of the LFM grid does not substantially change the predictions along the GOES 15 track for this event.

3.4.4 Comparing LFM and SWMF During Quiet Time

The investigation of the 2015 June 22 event raises issues regarding the models' prediction abilities during storms, but conclusions drawn from an analysis of a storm do not necessarily apply for non-storm events, due to the significant differences between the state of the magnetosphere during storm time and during quiet time. It is therefore instructive to compare LFM and SWMF predictions for January 31, 2013, a period of weak IMF and slow solar wind. Since the magnetopause only moves as far inward as geosynchronous orbit during intense geomagnetic conditions, we use THEMIS A, D, and E, whose orbits allow them to encounter the magnetopause much farther sunward of Earth than GOES can. During the second half of January 31, all three spacecraft crossed the magnetopause more than once, although at different times. The THEMIS D and E crossings are not considered here because they occurred during a period of northward IMF B_z, so the modeled crossing times are difficult to determine. We therefore restrict this discussion to the A crossing.

The IMF B_z turned southward around 20:55 UT and remained southward for over an hour. The solar wind proton densities were moderate, remaining between 9 and 10 cm^{-3} during the same hour without any significant sudden increases (see Figure 3.12). In response to the southward turning of the IMF, even though B_z was weak, the magnetopause moved inward near the location of THEMIS A, resulting in several magnetopause crossings by the spacecraft between 21:15 and 22:05 UT. Figure 3.12 shows the THEMIS A observations of B_z and proton density from 20:30 to 22:30 UT with the predictions by LFM and the SWMF, at two different resolutions for each model. Comparing the lower

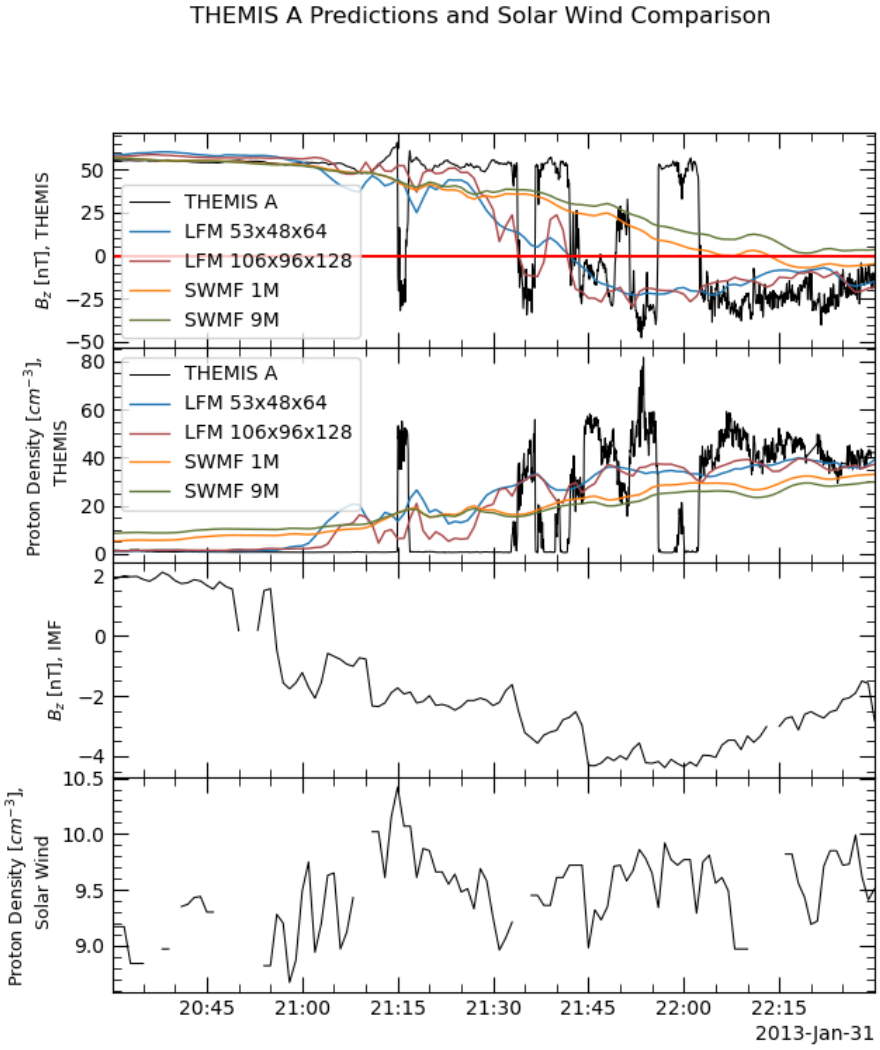

FIGURE 3.12: THEMIS A observations and predictions with contemporary solar wind conditions. From top to bottom: THEMIS A B_z and proton densities, as observed by the spacecraft and predicted by LFM and SWMF at two different resolutions each; IMF B_z and solar wind proton density during the THEMIS A magnetopause crossings.

resolution runs of the two models, we see that LFM predicts an earlier encounter with the magnetopause, at about 21:40 UT, than the SWMF does at 22:05 UT.

The total FACs are plotted in Figure 3.13 for two resolutions of LFM and of the SWMF, with the AMPERE data for reference. The integrated FACs from AMPERE are less than 1 MA throughout the event, apart from brief increases like the one in the northern hemisphere at 17:00 UT. Neither LFM nor the SWMF reproduce those increases. The LFM FACs are consistently stronger than those from SWMF for all resolutions. In response to the southward turning of the IMF after 20:45 UT, the total FACs in both hemispheres increase as IMF B_z remains negative, during which time the magnetopause moved inward over the position of THEMIS A.

Although increasing the spatial resolution of the MHD grid did not affect the GOES 15 LFM predictions for the 22 June 2015 event, changing the LFM grid from double (53x48x64) resolution to quad (106x96x128) resolution improves the THEMIS A predictions. In the quad resolution run, the model captures the crossings around 21:35 UT that it had previously missed. The total FACS predicted by LFM at quad resolution are stronger than those predicted by the double resolution run and also stronger than the AMPERE FACS. On the other hand, increasing from 1M to 9M cells does not significantly change the SWMF predictions for either the THEMIS A location or the integrated FACs.

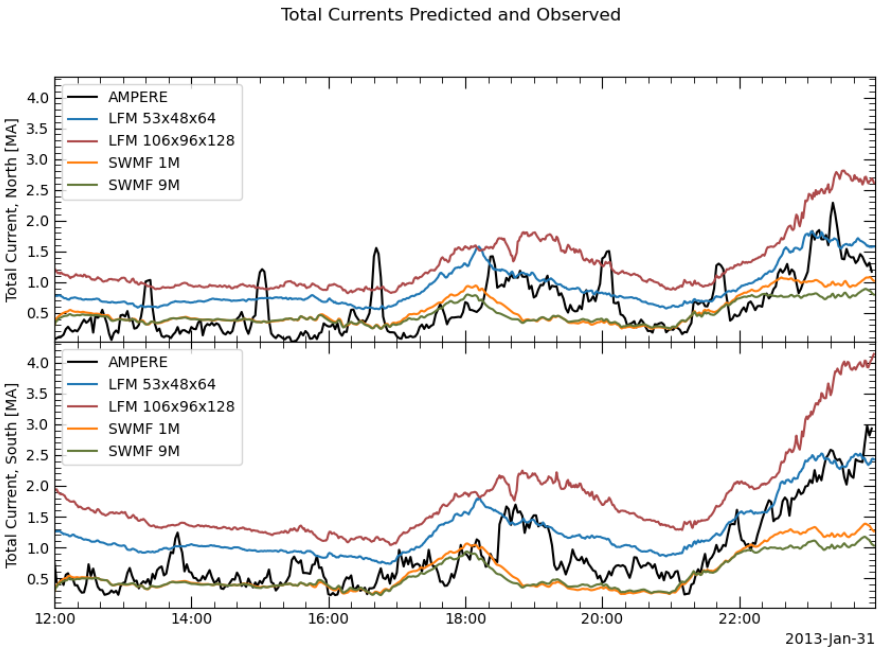

FIGURE 3.13: AMPERE integrated field-aligned currents for the northern and southern hemisphere, with the predictions from LFM and the SWMF at two different resolutions. The LFM currents for both runs are significantly higher than those from the SWMF.

3.5 Discussion

For the storm on 2015 June 22, LFM predicts a false magnetopause crossing by GOES 15 and the SWMF predicts two close magnetopause approaches that are not reflected in the real observations. LFM and the SWMF were run with several different ionospheric conductance models, including auroral conductances and several different values of constant conductance. However, changing the method by which the conductance is calculated does not seem to significantly affect the predictions along the GOES 15 track, although it does have some small effect on the magnitude of the integrated Birkeland currents. Of more interest are the improvements to the predictions when the MHD models are coupled to RCM. LFM shows small improvements in the GOES 15 predictions but is overall not strongly affected by the RCM coupling. The GOES 15 predictions from the SWMF, on the other, show significant improvement, since the magnetopause approaches around 21:00 and 22:00 UT are essentially removed. In the ionosphere, the integrated FACs from the SWMF have a greater percent increase than those from LFM, although the LFM currents have a greater overall magnitude (see Figure 2.14).

The discrepancy between the responses of the two sets of predictions can be explained the findings shown in Figure 3.9. The strength of the ring current calculated by the SWMF with RCM is much greater than that of LFM-RCM. The ring current's connection with the Region 2 FACs means that the SWMF with RCM sees a greater fractional increase in the total FACs than LFM does. The stronger ring current pushes the magnetopause outward and leaves GOES 15 inside the magnetosphere, where it was observed to be. For this storm, at least,

the SWMF better predicts the location of the magnetopause than does LFM, most likely because of the difference in the intensity of the calculated ring current between the two models.

During the THEMIS A magnetopause crossings on January 31, 2013, the LFM predictions along the THEMIS A track more closely match the observations than the SWMF predictions do. Considering for a moment only the lower resolution runs of both models, we see that LFM predicts a magnetosheath entry a few minutes before 21:45 UT, which corresponds to a real boundary crossing, while the SWMF does not predict that THEMIS encounters the magnetopause until 22:05 UT. The integrated Birkeland currents predicted by LFM are stronger than those from the SWMF, which seems to have resulted in more dayside magnetopause erosion in the LFM results. The primary driver of magnetopause motion during this period was the IMF B_z, since the solar wind density was not changing significantly. The SWMF also predicts lower FAC values than LFM does during the 2015 June 22 storm (see Figures 3.2 and 3.4), although the analysis of the predicted FACs for that event is complicated by the effects of the ring current on the Region 2 FACs.

Unlike the storm event, increasing the spatial resolution of the LFM grid for the simulation of the 2013 January 31 event makes a significant difference in the predictions along the spacecraft track. The quad resolution run predicts the inward and then outward motion of the magnetopause over the THEMIS A position at 21:35 UT, improving over the double resolution predictions at that time, although still missing several other brief crossings. The predicted total FACs also increase in magnitude. The SWMF predictions, however, hardly differ

at all between the 1M run and the 9M run, both at THEMIS and for the total FACs. A primary reason for the change in the LFM THEMIS predictions but not in the SWMF predictions is most likely the difference in grid structure for the two models. When LFM resolution is increased, the spatial resolution changes globally, affecting all cells on the grid; at THEMIS A, the cell size goes from 0.3 R_E x 0.57 R_E x 0.5 R_E (approximately) at double resolution to 0.1 R_E x 0.4 R_E x 0.35 R_E at quad resolution. For the SWMF, on the other hand, the MHD grid is block-adaptive, so naïvely changing the resolution of the grid does not always result in a different cell size in the region of interest. In this case, the cell size at THEMIS A is 0.5 R_E x 0.5 R_E x 0.5 R_E for both the 1M cell run and the 9M cell run, although the cell size changes in other regions of the magnetosphere. Users of the SWMF who may not be familiar with the grid structure should be aware of this when conducting research with the CCMC's Runs-on-Request tool.

The discrepancy between the effect of increasing LFM grid resolution during the June 2015 storm and the January 2013 event may stem from the fact that the solar wind conditions for the two events differ greatly in intensity. If solar wind densities are so strong that the real magnetopause is pushed in all the way past geosynchronous orbit, a situation which is somewhat uncommon, the MHD models will almost certainly predict that the magnetopause moves very far inward towards Earth. The THEMIS crossings here considered, on the other hand, take place during weak solar wind and IMF conditions, and the boundary is not being driven in suddenly by high densities. Rather, the magnetopause remains within a handful of R_E of the spacecraft for at least an hour, so any small motions back and forth are observed by THEMIS. Under such circumstances,

smaller cell size becomes more essential for capturing magnetopause motion than during one great push of the boundary across the position of the spacecraft. It thus seems likely that higher LFM grid resolution is more important, at least from the point of view of predicting magnetopause motion, for studying events with weak or moderate conditions than for intense storms, especially those with high solar wind densities.

3.6 Conclusions

In this study we have investigated the performance of two MHD models, LFM and SWMF, and their ability to predict magnetopause motion by comparing simulation results along a satellite track to the observations of a real satellite that crossed the magnetopause. We considered two events, one a storm on 2015 June 22 and another a quiet period on 2013 January 31. During the 2015 storm, GOES 15 crossed the magnetopause and both LFM and the SWMF predict spurious magnetopause approaches to the GOES 15 position. Coupling an inner magnetosphere model, RCM, to the MHD models improves the GOES track predictions more noticeably for the SWMF than for LFM, while changing the ionospheric conductance model hardly affected the GOES predictions at all for either model. The SWMF calculates a stronger ring current than LFM does, both with and without the RCM coupling, and including RCM gives the SWMF a greater fractional increase in the total field-aligned currents than LFM. During the non-storm event, LFM better captures the observed magnetopause motion at the location of THEMIS A and calculates stronger total FACS than the SWMF does.

Increasing the spatial resolution of the LFM grid has little effect on the GOES predictions during the storm but noticeably improves the predictions along the THEMIS A track. Overall, with respect to prediction of magnetopause motion, LFM outperforms the SWMF during the quiet time event, while the SWMF is more accurate during the intense geomagnetic storm.

Chapter 4

A Case Study of Bow Shock Current Closure

4.1 Abstract

On the bow shock in front of Earth's magnetosphere flows a current due to the curl of the interplanetary magnetic field across the shock. The closure of this current remains uncertain; it is unknown whether the bow shock current closes with the Chapman-Ferraro current system on the magnetopause, along magnetic field lines into the ionosphere, through the magnetosheath, or some combination thereof. We present simultaneous observations from MMS, AMPERE, and DMSP during a period of strong B_y, weakly negative B_z, and very small B_x. This IMF orientation should lead to a bow shock current flowing mostly south to north on the shock. AMPERE shows a current poleward of the Region 1 and Region 2 Birkeland currents flowing into the northern polar cap and out of the south, the correct polarity for bow shock current to be closing along open field lines. A southern DMSP F18 flyover confirms that this current is poleward of

the convection reversal boundary. Additionally, we investigate the bow shock current closure for the above-mentioned solar wind conditions using an MHD simulation of the event. We compare the magnitude of the modeled bow shock current due to the IMF B_y component to the magnitude of the modeled high-latitude current that corresponds to the real current observed in AMPERE and by DMSP. In the simulation, the current poleward of the Region 1 currents is about 37% as large as the bow shock I_z in the northern ionosphere and 60% in the south. We conclude that the evidence points to at least a partial closure of the bow shock current through the ionosphere.

N.B. The material in this chapter is taken entirely from Dredger et al. (2023), which has been published in the journal Frontiers in Astronomy and Space Sciences.

4.2 Introduction

When the supersonic and super-Alfvénic solar wind encounters the earth's magnetic field, it abruptly slows and becomes subsonic, creating the bow shock. Both the solar wind plasma and the interplanetary magnetic field are compressed across the shock. This compression of the magnetic field is associated with a curl of $\vec{B}$ and therefore, by Ampere's law, a current flows on the shock (see Section 1.3 in Chapter 1 for more details).

Because of the difference in density between the solar wind plasma and the plasma in the magnetosheath, a pressure gradient force points away from the bow shock back into the solar wind. This force does work on the incoming solar wind, converting flow energy into thermal energy. The current due to the

compression of the IMF also plays a part in extracting energy from the solar wind flow. The bow shock is always a dynamo or generator, meaning that $\vec{J} \cdot \vec{E} < 0$. Although the direction of the bow shock current clearly depends on the orientation of the incoming IMF, the current is always oriented in such a way relative to electric field in the frame of the shock so that mechanical energy is always extracted from the solar wind and converted into magnetic energy (Lopez et al., 2011).

The bow shock can also at times be the primary location in the system where force is exerted against the solar wind (Siscoe et al., 2002) and energy is extracted from the solar wind flow. As discussed by Lopez et al. (2010), when the magnetosonic Mach number is high, the pressure gradient force dominates and solar wind energy at the shock is primarily converted to thermal energy; on the other hand, when the Mach number is low, the $\vec{J} \times \vec{B}$ force dominates, and the energy extracted from the solar wind flow is dominated by the magnetic energy downstream of the shock. In this low Mach number regime, the $\vec{J} \times \vec{B}$ force exerted on the shocked solar wind in the magnetosheath by the interior portion of the Chapman-Ferraro current on closed field lines is balanced by an oppositely directed force from the exterior Chapman-Ferraro current on open field lines. Since under such conditions there is no net outward force at the magneotopause, the force on the solar wind must be mainly provided by the $\vec{J} \times \vec{B}$ force associated with the bow shock current (Lopez & Gonzalez, 2017).

The location of the primary force on the solar wind has consequences for energy transfer throughout the geospace system. Magnetopause reconnection and other load processes require energy to proceed. Lopez et al. (2011) found that

for conditions of low Mach number and strongly negative B_z the dynamo that can exist at high latitudes near the cusps disappears. Yet reconnection occurs at the magnetopause for strong southward IMF, which is a load. During low Mach number conditions, then, the bow shock is the main dynamo in the system and must be the energy source for magnetospheric processes (Lopez & Gonzalez, 2017; Siebert & Siscoe, 2002). This conclusion is supported by the work of Tang et al. (2012), who found that for strong IMF B_z the high latitude magnetopause current decreased while the bow shock current increased.

Poynting flux associated with the bow shock current carries energy away from the shock, so the closure of this current relates to the system of loads and generators in the magnetosphere (Lopez, 2018). The magnetopause is an obvious place for the bow shock current to close, but various studies have used global MHD simulations to investigate the question and found that the Chapman-Ferraro current is most likely not the only current in the system which can close bow shock current. Lopez et al. (2011) presented evidence that current in the magnetosheath with Region 1 polarity was connected to the bow shock, supporting the argument made by Siscoe et al. (2002) that the Region 1 field-aligned or Birkeland currents are partially closed by the bow shock current, which was first suggested by Fedder et al. (1997). A study by Guo et al. (2008) showed that under strong southward IMF a significant fraction of the Region 1 field-aligned currents (FACs) could originate from the bow shock. Tang et al. (2009) found that the bow shock current could also contribute to the cross-tail current and power nightside reconnection. In addition to these modeling studies, analysis of MMS

(Magnetosphere Multiscale) bow shock crossings by Hamrin et al. (2018) presented observational evidence consistent with closure of the bow shock current across the magnetosheath.

Except for Hamrin et al. (2018), there remains a significant lack of observational studies relating to bow shock current closure. Modeling has suggested a connection between current at the bow shock and current in the ionosphere, but the nature of this possible closure path has been virtually unexplored using real data. This paper presents a set of observations consistent with closure of bow shock current into the ionosphere on open field lines, for a single event. MMS crossings of the bow shock provide direct measurement of the shock current itself during a time of strong negative B_y and weakly negative B_z. During this period, AMPERE data show unipolar field-aligned currents, of the right polarity to close the observed bow shock current, while supporting observations from a DMSP flyover in the south pole confirm the existence of Birkeland current poleward of the open-closed boundary. Results from a simulation of the event using the Lyon-Fedder-Mobarry (LFM) global MHD model (Lyon et al., 2004) tell the same story. In the simulation, the unipolar, high-latitude Birkeland current corresponding to the current seen in the AMPERE observations is 37% to 60% as large as the current on the modeled bow shock. Taken together, these data and model results give evidence that the bow shock current could be closing through the magnetosheath and also in part through the polar ionosphere.

4.3 Methods

4.3.1 Data

The following is a brief description of the datasets used in this study. Solar wind data was compiled from ACE and from THEMIS C (Angelopoulos, 2008). ACE (Advanced Composition Explorer) orbits the first Lagrange point and provides solar wind observations. The ACE IMF data are provided by the Magnetic Field Experiment (MAG), another pair of fluxgate magnetometers (Smith et al., 1998)), and the plasma data are from the Solar Wind Electron, Proton, and Alpha Monitor (SWEPAM) (McComas et al., 1998), two electrostatic analyzers measuring ions and electrons separately. THEMIS C is one of the two spacecraft in the ARTEMIS mission and orbits the moon; magnetic field data are taken by the Fluxgate Magnetometer (FGM) (Auster et al., 2008), while plasma data come from the Electrostatic Analyzer (ESA) instrument (McFadden et al., 2008). Wind is another upstream solar wind monitor and has orbited at the L1 point since 2004; magnetic field data come from the Magnetic Field Instrument (MFI), a pair of fluxgate magnetometers (Lepping et al., 1995), and plasma data from the Solar Wind Experiment (SWE) instrument, an electron ion spectrometer (Ogilvie et al., 1995). We considered the Wind data but did not use it, as described later.

The MMS (Magnetosphere Multiscale) mission is a constellation of four spacecraft on an elliptical orbit around Earth designed to study magnetic reconnection (Burch et al., 2016). MMS magnetic and electric field data were observed by the suite of instruments on the FIELDS investigation (Torbert et al., 2016) and ion

moments are from the Fast Plasma Investigation (Pollock et al., 2016). Field-aligned currents are from AMPERE (Active Magnetosphere and Planetary Electrodynamics Response Experiment), a data product from Johns Hopkins University Applied Physics Laboratory that derives ionospheric currents using the magnetic perturbation data from the Iridium communications satellite constellations (Anderson et al., 2014). DMSP (Defense Meteorological Satellite Program) satellites fly on separate polar orbits and provide the Department of Defense with environmental information (Redmann, 1985). This study utilizes data from the plasma driftmeter to determine where the reversal of ionospheric convection from sunward to antisunward occurs, magnetometer data to indicate the location of Birkeland currents, and precipitating particle data from the SSJ/4 instrument to determine the location of the open-closed field line boundary. Detailed information about the spacecraft and instruments may be found at the websites for the missions listed in the Acknowledgements where the data sources are specified.

4.3.2 The Lyon-Fedder-Mobarry Model

The MHD model used in this study was the Lyon-Fedder-Mobarry (LFM) global MHD model (Lyon et al., 2004), and the version of LFM used in this study was LFM-MIX (Magnetosphere-Ionosphere Coupler Solver) (Merkin & Lyon, 2010) coupled to the Thermosphere-Ionosphere-Electrodynamics General Circulation Model (TIEGCM). TIEGCM is a first-principles model of the ionosphere-thermosphere system (Dickinson et al., 1981; Qian et al., 2014; Roble et al., 1988).

LFM solves the ideal MHD equations on a logically orthogonal, distorted spherical meshed grid. There is a higher density of grid points in areas of special interest, such as where the magnetopause and bow shock are typically located. The grid point separation in these areas is about 0.25 R_E. In the areas of the distant magnetotail and upstream of the bow shock, where the solar wind enters the grid space, the grid separation is about 1.25 R_E. The grid space extends from $-30R_E < X < 350R_E$ (in GSE) and is cylindrically wrapped to $Y, Z < 130R_E$. The run in this study had a spatial resolution of 106x96x128 cells, known as "quad" resolution (e.g. Liu et al., 2021). At the inner boundary, MIX calculates the field-aligned currents from the curl of B and maps them to ionospheric altitudes, where the height-integrated electrostatic equation is solved for the ionospheric potential. The ionospheric electric field is then mapped back to the MHD grid to provide a boundary condition for Faraday's Law and for the perpendicular velocity. The MIX grid for this run is $1^\circ \times 1^\circ$ in magnetic coordinates and the TIEGCM grid is $5^\circ \times 5^\circ$ in latitude and longitude. The simulation run was completed at NASA's Community Coordinated Modeling Center (CCMC).

4.4 Observations

4.4.1 Solar Wind Conditions During the Event

The OMNI data in the period of interest, namely, 11:00 UT to 14:00 UT on November 13, 2015, was taken from Wind observations, but these data have significant gaps at important times. For this reason, we considered the event with reference

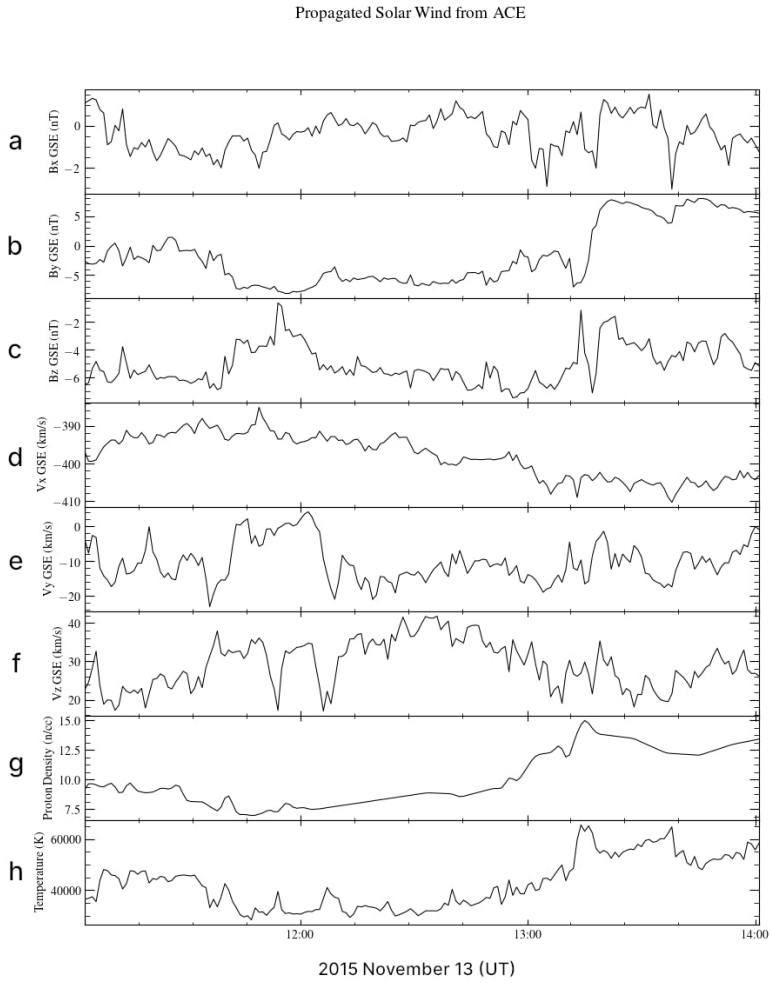

FIGURE 4.1: Combined ACE and THEMIS C data, propagated forward 62 minutes to the nominal bow shock. All data shown here are from ACE except the proton densities, which are from THEMIS C and have been time-shifted to correspond with the ACE data. The period of interest is from about 11:45 UT to shortly before 13:00. Panels a-c show the X, Y, and Z components in GSE coordinates of the IMF. Panels d-f show the X, Y, and Z components in GSE coordinates of the solar wind bulk velocity. Panel g shows the solar wind proton density and panel h shows the solar wind ion temperature. (Data provided at https://cdaweb.gsfc.nasa.gov/)

to ACE observations, which were more complete except for a total lack of proton density measurements. ACE and Wind were around 80 R_E apart in X, less than 40 R_E apart in Y, and roughly 8 R_E apart in Z. The exact location of ACE was (236.3, 35.3, 11.6) R_E. THEMIS C was relatively close to the Earth-sun line during this period, at (56.6, 18.3, 4.6) R_E. Based on a comparison between ACE and THEMIS magnetic field data, THEMIS C seemed to be seeing the same solar wind that ACE saw but approximately 48 minutes later. We determined that the delay was 48 minutes between the two sets of observations using the average solar wind velocity and the distance between the two spacecraft; we then confirmed that initial estimation by comparing plots of the two datasets. We were therefore able to replace the missing ACE densities (between 0950 UT and 1300 UT) with those observed by THEMIS C (time-shifted by 48 minutes), after which we propagated the combined dataset forward 62 minutes, to line up with available OMNI data. The resulting combined solar wind data time series is shown in Figure 4.1 and this solar wind time series, which was used to drive the LFM simulation at the CCMC, can be replicated using the information provided here and the archived ACE and THEMIS C data.

The coordinates used in this paper for all the spacecraft, with the exception of DMSP-F18, are Geocentric Solar Ecliptic (GSE) coordinates, where the X-axis points from Earth to the sun, the Y-axis is in the ecliptic plane, and the Z-axis is perpendicular to both, pointing northward. The solar wind conditions for the event are shown in Figure 4.1. Between 11:45 and 13:15 UT on November 13, 2015, IMF B_x was close to zero, while B_z was weakly negative. B_y was between -5 nT and -8 nT but was overall pretty steady during this period. Solar wind

velocities were steady, as were the temperature and pressure. The fact that B_y dominated the IMF during the event means that the bow shock current should have been flowing mostly south to north, as determined by the curl of $\vec{B}$ across the shock.

4.4.2 MMS Observations of the Bow Shock

Figure 4.2 shows MMS data from 12:53:00 to 12:55:30 UT, near the end of the period described above. Shortly before 12:51 UT (not shown), the MMS constellation crossed the bow shock into the magnetosheath, where it remained for roughly three and a half minutes before crossing back into the solar wind right after 12:54 UT, as shown. This encounter with the shock occurred at (X,Y,Z) = (9.7, 5.2, -0.9) R_E, relatively close to the nose. The compression of the magnetic field (panels b, c, d), the decrease in the ion density (panel f), and the increase in the ion velocity (panel g) across the shock are consistent with the data from ACE at the observed magnetosonic Mach number (panel h). This agreement means that the solar wind data we infer from ACE and THEMIS C are indeed the real conditions directly upstream of the bow shock, a fact that becomes crucial when we simulate the event with an MHD model using these data as input. Panel e of Figure 4.2 shows the current density components integrated along the spacecraft path; the dominant component is J_z with some contribution from J_y. These currents were calculated using the curlometer; for more information on this technique, see Dunlop et al. (2021). Thus, MMS observed a tilted south to north current as the spacecraft crossed the bow shock.

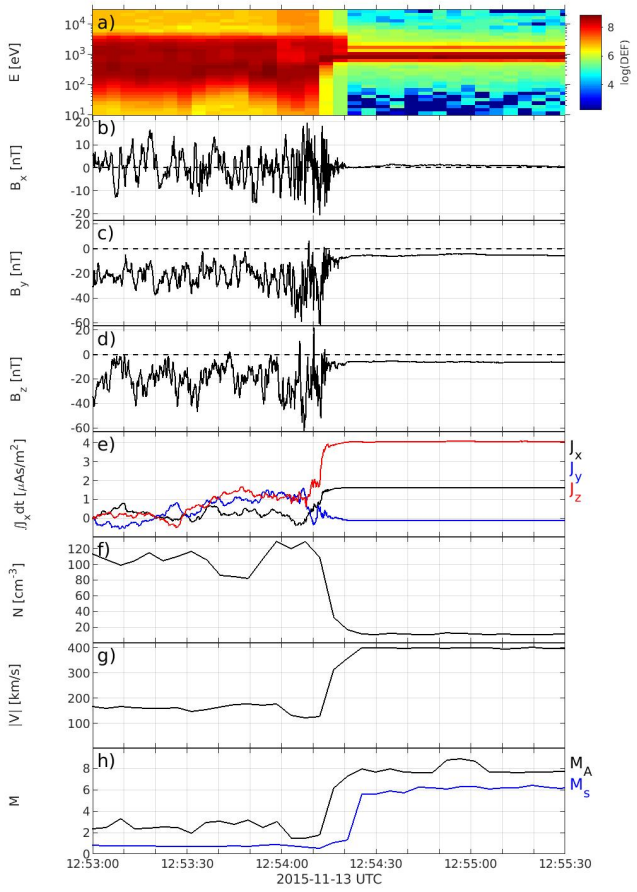

FIGURE 4.2: MMS observations of the bow shock. The spacecraft encountered the shock between 12:54:10 and 12:54:20 UT. (a) Ion energy-time spectrogram, (b-d) magnetic field components in GSE coordinates, (e) GSE components of J, each integrated with respect to time, (f) ion density, (g) the magnitude of the ion velocity, and (f) the Alvén (M_A) and magnetosonic (M_s) Mach numbers.

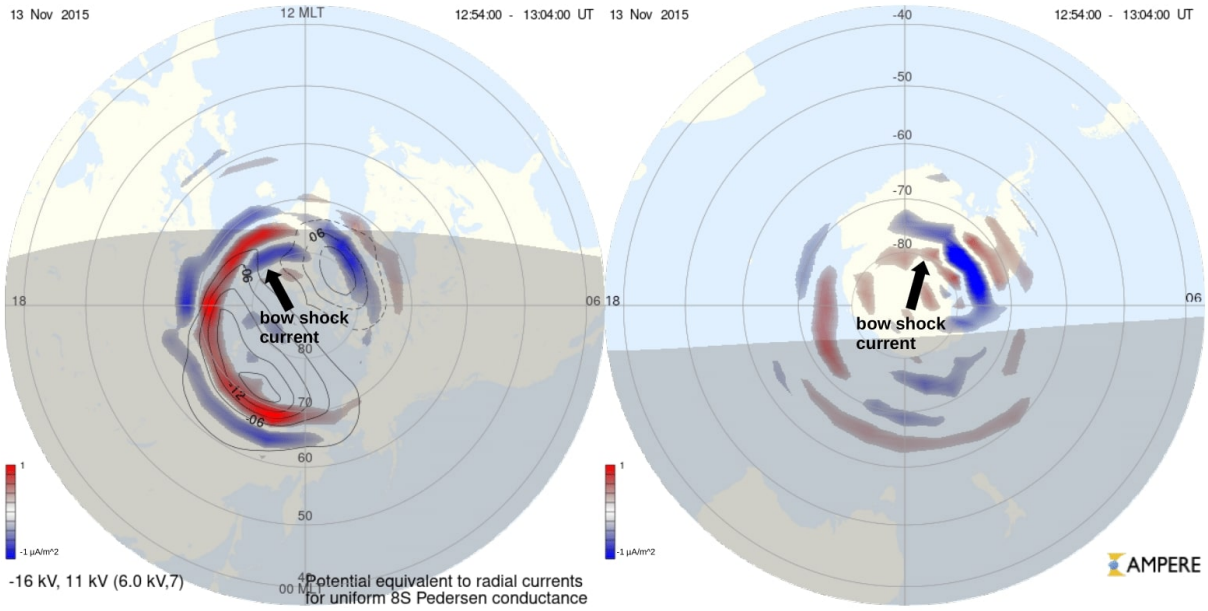

FIGURE 4.3: AMPERE derived Birkeland currents. The northern hemisphere is on the left and the southern hemisphere is on the right. In both hemispheres, red currents are coming out of the ionosphere and blue currents are going in. The southern hemisphere plot uses a "glass-Earth" projection. We see high latitude unipolar current (indicated) in the afternoon sector in the north and in the morning sector in the south, both with the right polarity to be bow shock current closing into the ionosphere. Potential contours are not available for the southern hemisphere on this day. (Plots from http://ampere.jhuapl.edu/)

4.4.3 AMPERE and DMSP Observations of Field-Aligned Currents

The AMPERE-derived Birkeland currents are shown in Figure 4.3; red indicates current coming out of the ionosphere (upward) and blue current is flowing into the ionosphere (downward). The projection is known as "glass-Earth", so that the view in both cases is from the perspective of an observer above the north

pole; the southern polar cap view is as if the observer were looking through a transparent Earth. In each view noon is at the top of the figure, dawn to the right, and dusk to the left. We can see the Region 1 current flowing into the ionosphere (blue) in the dawn sector and out (red) in the dusk sector, while at lower latitudes are the Region 2 currents, of opposite polarity to Region 1. The convection pattern is rotated towards the afternoon, consistent with the negative IMF B_y (Heppner & Maynard, 1987). At the time of MMS's encounter with the bow shock, AMPERE data show a unipolar current region poleward of the Region 1 Birkeland current patterns in both northern and southern hemispheres, with the northern hemisphere current primarily in the postnoon sector and the southern hemisphere current in the prenoon sector, again consistent with the overall convection pattern for negative IMF B_y (Heppner & Maynard, 1987). This current flows into the northern polar cap and out of the south at high latitudes. These FACs are of the right polarity – downward (blue) in the north and upward (red) in the south – to close the south-north bow shock current observed by MMS, if those currents are on open field lines. It seems likely that if currents originating outside the magnetosphere, like the bow shock current, do connect to the Birkeland currents, they would close along open field lines, which reach out into the magnetosheath, rather than closed field lines. The critical point, then, is to find the position of these Birkeland currents relative to the open-closed field line boundary.

For this event, we can determine the location of the open-closed boundary at least in one hemisphere by means of ion driftmeter data from DMSP. During the period in which MMS crossed the bow shock, F18 was making an overpass of the

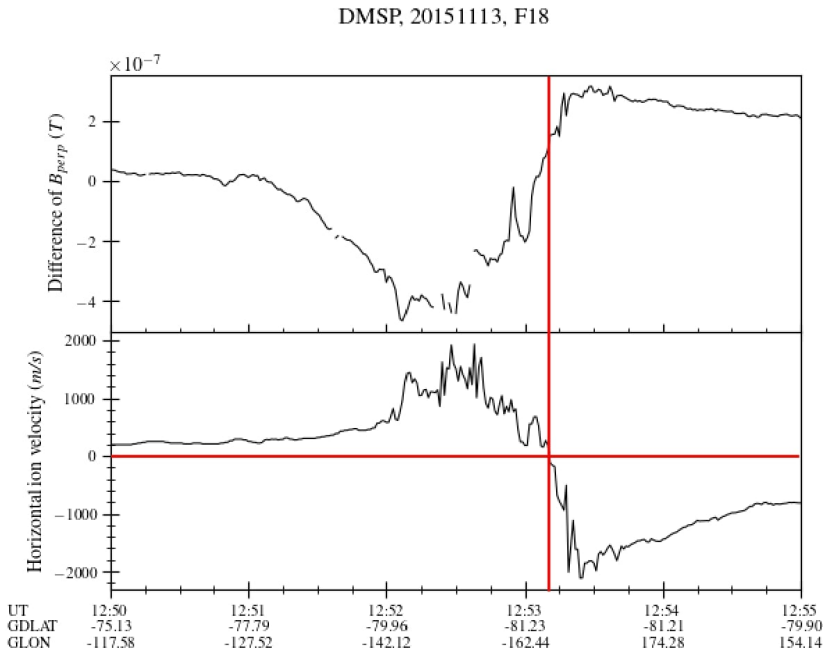

FIGURE 4.4: F18 observations: difference of B_{perp} and horizontal ion drift velocities. After the ion velocities turn negative shortly after 12:53 UT, marking the convection reversal boundary, we see some magnetic field perturbations, indicative of current flowing on open field lines. F18 is here moving poleward. (Data provided at http://cedar.openmadrigal.org/list/)

southern polar cap and flew right through the high latitude upward current seen by AMPERE and discussed above. The top panel of Figure 4.4 shows the difference between the observed magnetic field and the International Geomagnetic Reference Field (IGRF) model perpendicular to the flight track of F18, which gives an estimate of the magnetic perturbation resulting from Birkeland currents (Alken et al., 2021). The bottom panel is a plot of the horizontal ion drift velocities, from which we can determine the convection reversal boundary by noting where the plasma velocities turn negative. Negative velocities correspond to open field lines being dragged toward the nightside and the plasma flowing with them, whereas positive velocities are associated with closed field lines and plasma moving toward the dayside, as expected for the magnetospheric convection pattern. By this reasoning, we can say that F18 encountered the open-closed boundary a few seconds after 12:53, flying poleward. From the magnetic field perturbations observed after the satellite passes through the boundary, we infer that part of the upward current through which F18 flew was flowing on open field lines. The particle precipitation data in Figure 4.5 shows a clear auroral oval with an open polar cap, consistent with southward IMF. Just after 12:52 we see an intense downward flux of low energy electrons that corresponds to an upward Birkeland current. We identify this downward electron flux as an upward current because electrons are the main current carriers for Birkeland currents, since ions are much heavier and therefore slower to respond to electromagnetic forces. Additionally, the particle detectors on DMSP satellites only look upward, so they cannot measure any upward-moving ions that might contribute to a downward current. We do see some precipitating ions, but after F18

crosses the open-closed boundary at 12:53 the ions disappear. Only a distinct electron population remains; the spectrum of this population, shown in Figure 4.6, can be compared to the spectrum shown in Figure 1 in Newell et al. (1996), which is identified as an accelerated electron distribution. The spectrum shown here is not as sharply peaked as the spectrum in Newell et al. (1996), with much weaker acceleration and therefore much weaker field-aligned potential, but the two spectra have similar characteristics otherwise. This is therefore the signature of electrons carrying an upward current, with a field-aligned potential accelerating the electrons downward to the velocity required to carry the current, which in this case was on open field lines. In short, the DMSP observations confirm that in the southern hemisphere there was current at the location seen by AMPERE and of the same orientation, poleward of the convection reversal boundary and therefore on open field lines.

4.5 Results from the MHD Simulation

As mentioned above, we are confident, because of the MMS observations right outside the bow shock, that the solar wind conditions seen by ACE/THEMIS C, propagated forward to a nominal shock position, accurately represent the real conditions at the bow shock during the event and thus are the correct input to the simulation for the event. We used the propagated ACE/THEMIS C dataset described in Section 4.4.1 to drive LFM at quad resolution. The model more or less correctly predicts the location of the bow shock at the time of the crossing by MMS, since the satellite's location during real crossing at 12:54 UT was only

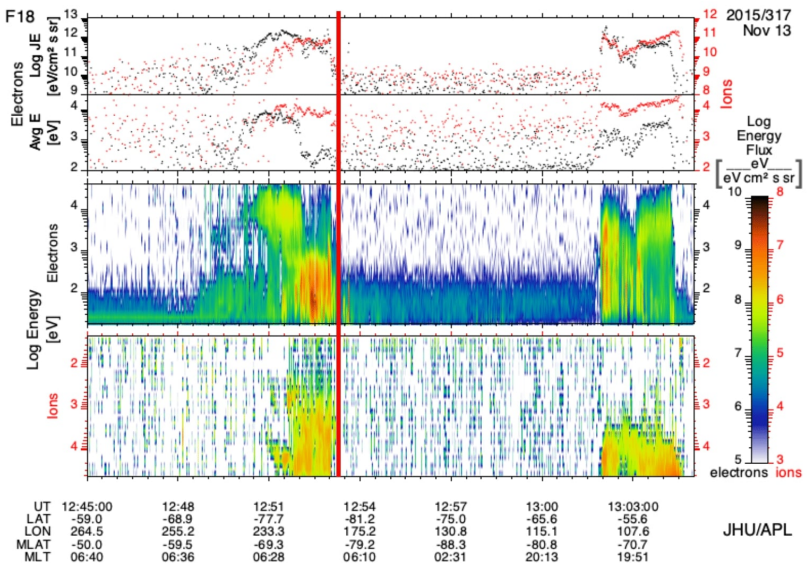

FIGURE 4.5: F18 particle precipitation data over the southern polar cap. The red line indicates when the spacecraft crossed the convection reversal boundary at 12:53 UT. (Plot from http://sd-www.jhuapl.edu/Aurora/spectrogram/)

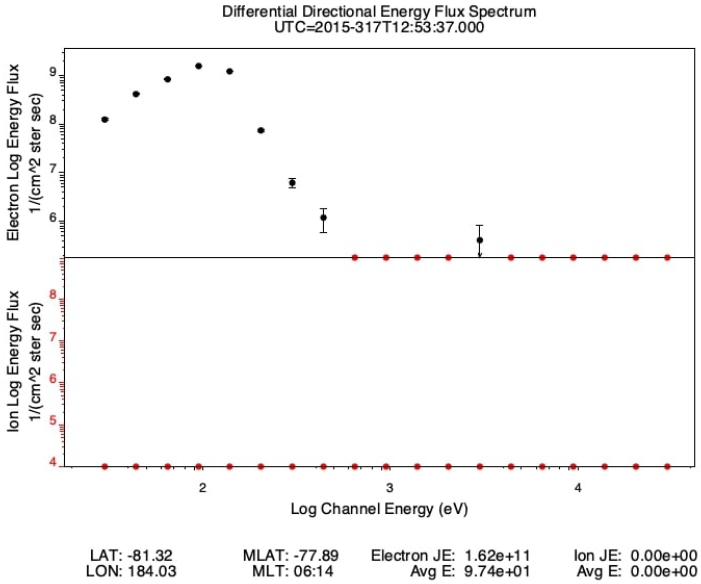

FIGURE 4.6: Spectrum of the particle precipitation seen at 12:53:37 in Figure 6. The accelerated Maxwellian seen in the electron spectrum indicates electrons being pushed upward in a current. (Plot from http://sd-www.jhuapl.edu/Aurora/spectrogram/)

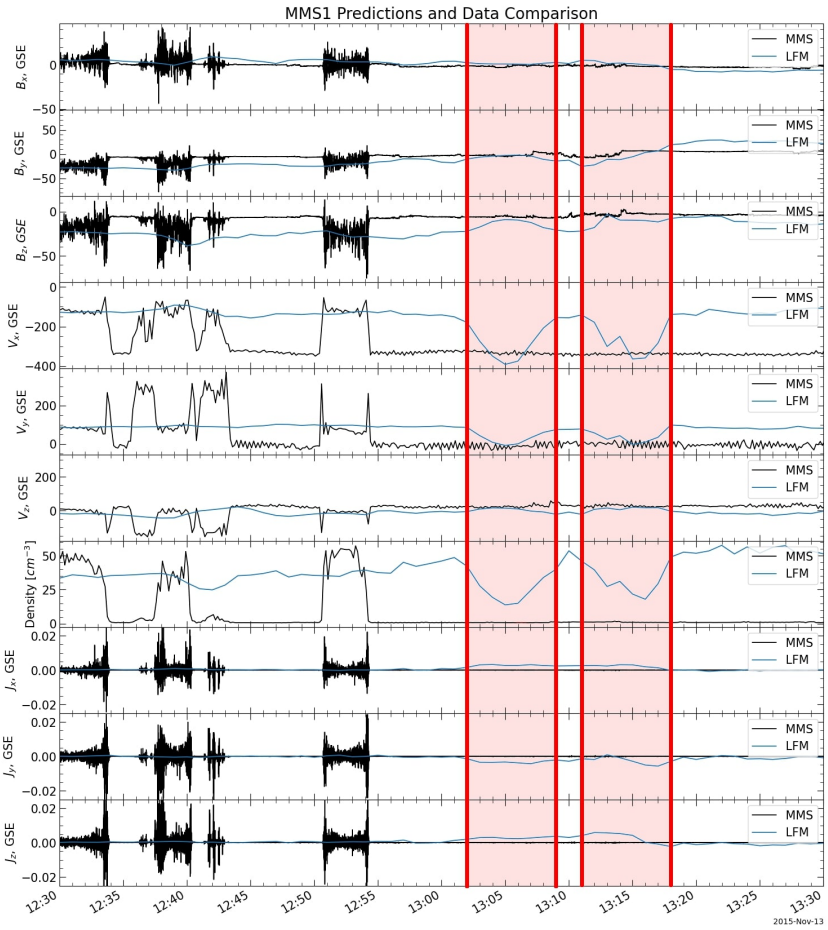

FIGURE 4.7: MMS1 data (black) and LFM output along the MMS1 track (blue) for the hour around the crossing time on 2015 November 13. Although the modeled satellite did not encounter the bow shock exactly at 12:54 UT or during the earlier crossings shown, the modeled bow shock was near the MMS position, as shown by several predicted encounters with the boundary (marked in red) around 13:05 and 13:15 UT. The periods spent out in the solar wind are shaded red. From the top, the plotted quantities are the magnetic field components B_x, B_y, B_z, proton bulk velocity components V_x, V_y, V_z, the proton number density, and the components of the current J_x, J_y, and J_z. Vector quantities are in GSE coordinates. The current from LFM is in $\frac{\mu A}{m^2}$ and the current from MMS is in $\frac{nA}{m^2} \times 10^{-6}$ (see explanation in text).

about 0.1 R_E from its location during the modeled crossing at 13:01 UT, less than the separation of the grid points in this region. Figure 4.7 shows the modeled conditions along the MMS1 track for the hour around the time of the event; the closeness of the MMS constellation, compared to the LFM spatial resolution in the magnetosheath, means that we can choose any of the four spacecraft to compare to the simulation. Although the model output in Figure 4.7 is of a lower temporal resolution than the actual data, i.e. every minute as opposed to seconds, we can see that the simulated bow shock passes over the satellite shortly after 13:00 UT; both magnetic field and plasma parameters change rapidly from magnetosheath values to values corresponding to the solar wind input conditions at the time. The predicted B_y and B_z approach the IMF values reported in the OMNI data at that time, while V_x decreases to -400 km/s and V_y, along with V_z, decreases to nearly zero. Correspondingly, the proton density decreases by more than half as the simulated MMS1 satellite encounters the bow shock. The modeled crossing is about seven minutes after the real crossing. In addition, before the 12:54 UT crossing MMS encountered the bow shock a handful of times in quick succession, which are not predicted by the model. However, the simulated boundary is near the MMS position at the time of the crossing under consideration, since the modeled satellite measures very similar magnetosheath values to the real MMS observations, except for the current. Any minor discrepancies could be a result of local disturbances on the bow shock, the physics of which are not necessarily included in the MHD simulation. The discrepancies could also be a result of uncertainties in solar wind timing and the spatial resolution of LFM versus the actual thickness of the bow shock. In the magnetosphere

domain the temporal resolution of LFM is on the order of a second, although the code typically writes the MHD variables to a data file with a one-minute cadence. The MMS data used for this study are fast survey mode data, and the resolutions are 16 s^{-1} (magnetic field) and 32 s^{-1} (electric field) (Torbert et al., 2016); ion data are taken at 4.5 s per sample (Pollock et al., 2016). Because of the high temporal resolution of the model, small discrepancies between the data and the model are better attributed to the spatial resolution of the MHD code than to the temporal resolution. Broadly speaking, however, the bow shock was in the right position at the right time in the simulation output.

Although the directly measureable quantities such as $\vec{B}$ and $\vec{V}$ in the simulation match the corresponding MMS quantities reasonably well, the current in LFM is significantly smaller than the current in the MMS dataset. This can be explained by the fact that $\vec{J}$, the current per unit area, is a derived quantity, determined from an approximation of Ampere's law in both MMS data and LFM calculations, which necessarily involves a term like $\frac{\Delta B}{\Delta R}$, where R is the distance between either two spacecraft or two points in the simulation. Because of the much higher spatial resolution in the MMS current calculation than in LFM, MMS $\vec{J}$ is often of much greater magnitude than the simulated $\vec{J}$. However, the total current at the bow shock, which is determined by the compression of the magnetic field across the shock, is very similar for both observations and simulation, as can be seen in Figures 4.1, 4.2, and 4.7. There can also be noise and processes such as physical waves contributing to the measured ΔB that are not actually associated with currents, yet they can contribute to the calculation of $\vec{J}$. The calculation methods additionally assume a linear change in $\vec{B}$ between

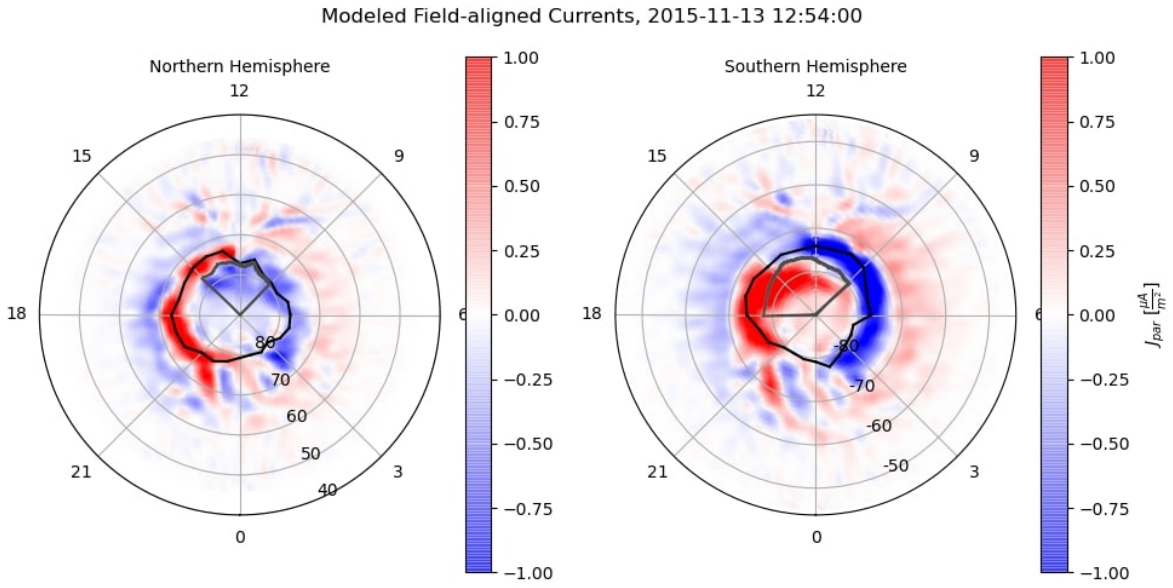

FIGURE 4.8: MIX currents for the time of the MMS crossing. Red current is flowing out of the ionosphere and blue is flowing in. The southern hemisphere is once again in a "glass-Earth" projection. The black tracings indicate the polar cap boundary and the regions circled in grey contain the currents possibly closing the bow shock. The model broadly reproduces the AMPERE-derived currents.

the two spacecraft, which may not be true. For the very small ΔR in the case of MMS, errors in the estimate of ΔR can have a large impact on the calculation of the current. For these and additional caveats associated with the calculation of $\vec{J}$, the magnitude difference between the MMS current and the LFM current is not surprising and it is more instructive to compare the variations of the two parameters than their magnitudes.

The simulated field-aligned currents from MIX are shown in Figure 4.8; red currents are upward and blue currents are downward (matching AMPERE).

Like the AMPERE images, dawn is on the right in both hemispheres. The simulated FACs are generally similar to observations, including the tilt in the patterns due to IMF B_y; in particular, the model produces FACs at high latitude, resembling those seen by AMPERE in Figure 4.3, that are flowing along open field lines. The modeled currents are similar in magnitude, though a bit larger than the AMPERE-derived currents, but it is known that MIX tends to overestimate the cross polar cap potential, which would explain this discrepancy (Wiltberger et al., 2012). The scale sizes of some FAC features are much smaller than the MIX resolution, so the currents in the MIX plots appear smoother than those in the AMPERE plots.

Figure 4.8 also shows the polar cap boundaries for both hemispheres as calculated by the model. The high latitude upward current in the southern hemisphere on the dawn side, indicated by the arrow in Figure 4.3, is flowing on open field lines, both in DMSP observations and in the simulation results. Moreover, the AMPERE plot for the northern hemisphere includes the potential contours from the MIX model, using real data and run separately from the MHD code; it can be seen that the northern counterpart of the southern hemisphere current discussed above was in a region of antisunward plasma flow, poleward of the convection reversal boundary. Therefore, the global simulation of the event and the observations are in agreement that the high latitude Birkeland current with polarity consistent with bow shock current closure was flowing on open field lines.

To more quantitatively compare the current on open field lines in the ionosphere and the south-north current flowing on the bow shock, we integrated the

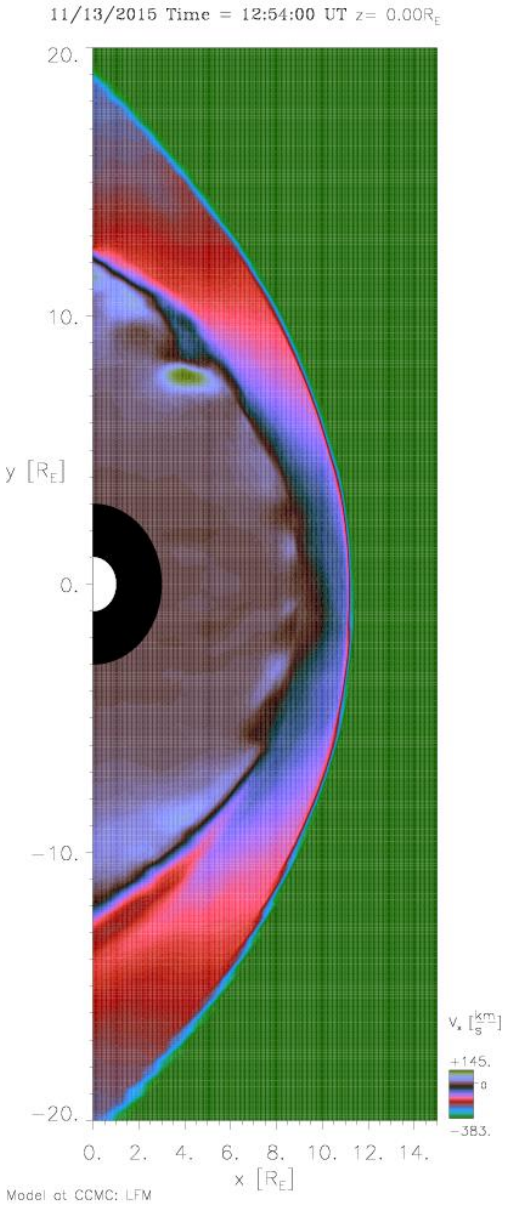

FIGURE 4.9: The equatorial plane in the LFM simulation at 12:54 UT, colored by the X component of the ion velocity. The bow shock was identified by eye using a plot like this for the integration of the J_z on the bow shock described in Section 4.5. (Plot generated by the CCMC)

modeled currents in both locations. If the bow shock current is closing at least partially into the ionosphere, the integrated current on open field lines which we identify as possible bow shock current should be less than or equal to the integrated Z-component of the current density on the bow shock in the equatorial plane. Identifying the bow shock in the LFM output by eye in a plot of the equatorial plane (eg. Figure 4.9), using the discontinuity in the solar wind density across the shock, we find that the dayside bow shock current flowing from south to north in the simulation is 2.3 $\pm$0.4 MA. This value was calculated by taking the value of the current per square meter in each grid cell identified as containing the bow shock, for X $>$ 0 R_E in the equatorial plane; these values were multiplied by the area of the X-Y face of the cell and then summed. Since identifying the bow shock by eye introduces some uncertainty, the process was repeated with slightly different selections of cells and the results were averaged. In Figure 4.8, the areas in each polar cap enclosed by the grey contours represent the regions of possible bow shock current, based on overlap with the Region 1/Region 2 current pattern. The integrated current in the northern region is 0.84 $\pm$ 0.08 MA and in the southern region 1.4 $\pm$ 0.2 MA. In the southern hemisphere, part of the upward current on open field lines was omitted from the calculation as it seemed to belong more properly to the Region 1 FACs, assuming a more or less regular "banana shape" for the Region 1 current, so the southern hemisphere value represents in some sense a lower limit for that calculation. Conversely, the downward current on open field lines is more difficult to separate into Region 1 current and possible bow shock current, so the northern hemisphere value is more of an upper limit. For both cases the identification of

possible bow shock current in the ionosphere and, consequently, the calculated values are certainly not exact, yet we have provided them here as estimates. The integration of the current in the northern (southern) hemisphere was performed multiple times, including once with all of the dayside blue (red) current inside the polar cap boundary, and the results were averaged. The uncertainties stated above are the standard deviations for each set of calculations. Regardless of the uncertainties, in both the northern and the southern hemisphere, the integrated currents on open field lines are a fraction of the estimated south-north current on the bow shock.

4.6 Discussion and Conclusions

In this paper, we have presented a set of coordinated observations of the bow shock and low altitude Birkeland currents on November 13, 2015, during a period when the IMF was dominated by the B_y component. The MMS data show the primarily south-to-north current at the bow shock, while DMSP and Ampere show upward Birkeland current in the southern hemisphere at high latitudes in the MMS local time sector. Moreover, the DMSP data show that some of the Birkeland current was flowing in the polar cap on open field lines, and as such would connect to currents in the magnetosheath. These observations are consistent with the hypothesis that, in this case, some of the bow shock current was closing across the magnetosheath into the ionosphere.

The event has been simulated with the LFM global magnetosphere model. The simulation puts the bow shock in the right place at essentially the right

time. The Birkeland current pattern in the simulation is generally similar to the pattern derived by AMPERE, particularly with respect to the high latitude Birkeland current that is of the correct polarity to close part of the bow shock current. Moreover, the model results indicate that some of this Birkeland current is on open field lines, poleward of the Region 1 currents. Given observations of the predicted bow shock current, a Birkeland current on open field lines of the correct polarity and magnitude to close the bow shock current at least partially, and support from a global MHD simulation showing the same results, we believe that the evidence is strongly in favor of the closure through the polar cap ionosphere of at least part of the bow shock current.

Many questions remain about bow shock current closure. If the bow shock current is closing in part through the ionosphere with the Birkeland currents, where does it cross the magnetosheath? Does it flow back towards the nightside first, or does it begin to flow along open field lines on or close to the dayside? The relationship of the bow shock current with the Chapman-Ferraro current, and what role the magnetopause plays or does not play in bow shock current closure, should also be investigated. It is probable that the nature of this closure depends largely on prevailing conditions. The IMF clock angle dictates the direction of the bow shock current and thus clearly regulates its closure. The magnetosonic Mach number may be particularly important, since it affects the location of the primary force exerted on the solar wind and the main dynamo in the system. In addition, ionospheric conductance must influence the ability of the bow shock current to close into the polar cap. The fraction of the bow shock current that closes into the ionosphere could also vary, depending on the state

of the magnetosphere. Further study is needed to examine the interconnected system of currents, conductance, and solar wind conditions.

Chapter 5

Discussion and Future Work

5.1 Magnetopause Motion Studies

Although Chapters 2 and 3 present valuable findings about the capabilities of MHD models, the studies are based on a handful of events and therefore the conclusions may be limited, perhaps applicable only to the conditions of the particular time periods considered. More statistical studies could be undertaken, expanding the parameter space and confirming the results. The primary obstacle to this kind of study is a lack of observational coverage for events of interest. The eight storms in Collado-Vega et al. (2023) were chosen because they were the only magnetopause crossing events in recent years with at least one of the two GOES satellites on the dayside during the storm. Theoretically, as long as there are solar wind observations available, any storm in history can be simulated, and the GOES program has had satellites in orbit since the 1970s. In fact, Rufenach et al. (1989) conducted an observational study of 64 magnetopause crossings at geosynchronous orbit, using data from then-operational GOES 2, 5, and 6. The OMNI dataset has one-minute data, needed to drive the simulations,

from 1981 onward. It is thus possible that there are significant storms from the 1980s, 1990s, or 2000s with GOES dayside observations that could also be simulated and for which the metrics described in Chapter 2 could be calculated.

The situation becomes more complicated for expanding the work of Chapter 3. Investigating the applicability of L1 observations to near-Earth space for particular events requires alternate solar wind data like those presented from THEMIS or other missions. Such backup observations are not always available, even in recent years. Other aspects of the studies in Chapters 2 and 3 rely on the AMPERE dataset for the Birkeland currents, but AMPERE only includes data since April 2010. The more parts of the system we want to consider, the more limited the selection of events becomes.

As mentioned previously, the analysis of how well MHD codes can predict magnetopause location has importance for spacecraft operations. Stepping away for a moment from studies of the magnetopause, it is crucial for both operations and research to understand just how reliable the L1 observations are as a representative of the solar wind that impacts the Earth's magnetosphere. Ongoing work in the UTA space physics group will quantify, using THEMIS B and C observations, the probability that the solar wind measured by ACE and Wind at L1 corresponds to the solar wind measured closer to the bow shock.

GOES is not, however, the only mission that can observe magnetopause crossings. The advantange of using GOES for this kind of study is that it orbits close to Earth, so the conditions that would push the boundary far enough inward that GOES would observe it must be very strong. THEMIS or MMS, on

the other hand, also can cross the magnetopause when the apogee of their elliptical orbits lies on the dayside. If we expand the study to less intense conditions, we can include observations of the magnetopause from THEMIS or MMS. This would build on the work in the second half of Chapter 3, which compares the performance of two models with respect to magnetopause motion during quiet time. There are many more observed magnetopause crossings besides those during large storms, including for northward IMF, although these can be more challenging to analyze.

Another way to expand the list of suitable events is simply to wait a few years. The solar cycle at the time of writing is already promising to hold much more solar activity than the last cycle, especially as solar maximum approaches. It would not be surprising if we soon were to have a number of interesting storms that would drive the magnetopause in past THEMIS, MMS, or even geosynchronous orbit.

Other limitations to the work presented come from the models themselves. We have here focused on the models as they exist currently at the CCMC in a sort of "operational" role, available to be used by researchers who may or may not be familiar with the details of the codes and their various strengths and weaknesses. These publicly available versions, however, are not the most recent versions of the models, since development continues for all of these codes. Even considering the versions at the CCMC, newer versions of the SWMF and OpenGGCM have been made available since the original simulation runs in Collado-Vega et al. (2023) were performed.

Not all of the couplings or grid options at the CCMC have been fully explored by the studies discusses here, opportunities which would be appropriate for followup studies delving further into the capabilities of a particular model. Such follow-up studies, however, might be better conducted with the most recent, "cutting-edge" versions of the individual codes. The SWMF in particular can be coupled to a wider variety of inner magnetosphere and ionosphere models, with, for example, more realistic ring current calculations (e.g. Fok et al., 2001) or physics-based conductances (Mukhopadhyay et al., 2022). Multi-fluid versions of the SWMF and of LFM also exist, which could provide interesting comparisons with the single-fluid versions. Finally, LFM itself will eventually be replaced by its successor, the Multiscale Atmosphere-Geospace Environment model (MAGE), a rewrite of LFM with numerous improvements (Zhang et al., 2019). How many of LFM's strengths and weaknesses have been passed on to MAGE and what is unique to the new code remains to be fully explored. Certainly, there are plenty of opportunities to expand the research here presented by simply investigating with the many other options for the various existing modeling tools.

Most of the results discussed in this work have been qualitative, comparing trends and searching for cause and effect. The analysis which leads to the metrics calculated in Chapter 1, however, takes an obviously quantitative approach. These metrics have been presented without any strict discussion of uncertainties, which may seem unusual. The lack of formal error propagation in the analysis is due in large part to the nature of a series of dichotomous forecasts of rare events, like magnetopause crossings. The contingency table can easily

be altered simply by increasing or decreasing the number of times we ask the question "is the spacecraft in the magnetosheath?" This renders any attempt to use Poisson statistics essentially meaningless, since the total number of forecasts can be easily changed by extending the time period for which we calculate the metrics by several hours before the particular storm under consideration, but without really improving the analysis.

Additionally, it is at this time impossible to properly take into account uncertainties due to the solar wind propagation from the upstream monitors, simply because we do not have a quantitative understanding of these uncertainties. This project, a very necessary and somewhat complicated one, is currently being undertaken by members of the UTA space physics group. When the community has a sufficiently comprehensive grasp of the solar wind uncertainty, it will be possible to better support model predictions of specific quantities, such as magnetopause position, with formal error analysis. For the present, neglecting the uncertainties due to solar wind input, we do know that the thickness of the magnetopause is much smaller than the size of the grid in the relevant region, another possible source of uncertainty here. The motions of the boundary which we here consider, from its usual position inward past geosynchronous orbit, also cover several RE, a distance much larger than the grid spacing. We are thus confident in our results from the point of view of the uncertainties we do understand.

Finally, we may point out that the purpose of this type of analysis is performed for the purposes of presenting a user of the models with a quantitative measure of their accuracy. We here have intended to study the performance of

the models when they use the standard solar wind input available, a method which we have shown is fraught with uncertainty due to the spatially inhomogeneous nature of the solar wind. A user of the model in an operational context is simply interested in the likelihood of the model to make a false prediction, whereas uncertainties are more apropos to a scientific investigation of space weather phenomena. We therefore consider that we are justified in neglecting a discussion of the uncertainties in our analysis, because of both the nature of the metrics calculated and the scope of the study itself.

5.2 The Bow Shock Current

The event study presented in Chapter 4 demonstrates, with evidence from both observations and modeling, that bow shock current closure into the ionosphere is possible under solar wind conditions with a significant IMF B_y component. Whether or not the bow shock current does indeed close along open field lines into the polar cap is difficult to establish definitively within a short period of time, due to the large region of space spanned by the bow shock, the turbulence of the magnetosheath, and the changing state of the magnetosphere for varying IMF conditions. Visualization of MHD model results permits the tracing of current streamlines throughout the geospace system, so, in theory, one could simply trace the current from the bow shock to see where it closes. The primary issue with this method has to do with the way that the path of the streamlines is calculated. Current can diverge from one grid cell to another, but the streamline algorithm must choose only one direction. In this way, significant current

pathways can be missed, so a negative result from streamline studies would be inconclusive. An alternate approach would pursue the problem of bow shock current closure by conducting groundwork studies to answer questions that will either support or rule out the possibility of closure into the polar cap. Several such studies are discussed below.

The first two studies, which would be relatively brief, follow on from the result of Chapter 4 to assess how frequently the current on open field lines in the polar cap is less than or equal to the north-south current flowing on the bow shock. The ratio of open FACs to bow shock current must be less than or equal to 1 if the bow shock current closes at all into the ionosphere. One could choose 15-20 real events under predominantly east-west IMF (B_y-dominated) conditions, when the bow shock current will flow primarily in the north-south direction, with relatively high Mach number like the event in Chapter 4; for these events, one would use the AMPERE dataset and measurements from upstream solar wind monitors to measure the amount of high-latitude current in the polar cap and compare it to the north-south bow shock current estimated from the nominal solar wind conditions. The results of this study would put limits on how plausible the FAC-closure argument is, using real observations. For the second study, one could use an MHD model to investigate how the ratio of open FACs to bow shock current varies with IMF clock angle, performing similar calculations to those in Chapter 4.

The purpose of the third study would be to investigate the ratio of Poynting flux associated with the high latitude FACs and the bow shock current. This project would have several parts, but at the center of the study is the use of

an MHD model to calculate the modeled Poynting flux along the tracks of the DMSP satellites. First one would use the method described in Knipp et al. (2021) to calculate the measured Poynting flux from DMSP along the satellite track for real events and compare these to the results of the same calculation from the model; this would establish how well the model calculates the Poynting flux in the ionosphere. Next, one would calculate the energy being extracted from the solar wind at the bow shock in the model and compare it to the amount of Poynting flux on open field lines in the ionosphere. The ratio of ionospheric Poynting flux to energy extracted from the solar wind should be very small, as the vast majority of the solar wind energy does not enter the magnetosphere, being used instead to reaccelerate the shocked solar wind in the magnetosheath back up to supersonic speeds farther downstream. One would then search for causal links between variations in the incoming solar wind conditions and any increases or decreases in the ionospheric Poynting flux. This can be done primarily by answering the following questions: (a) does changing the solar wind parameters affect both the ionospheric Poynting flux and the energy extracted at the bow shock in the same way, and (b) if so, is there a consistent timing between the changes in the two locations? If both questions can be answered in the affirmative, the argument relating the high latitude field-aligned currents and the solar wind driving at the bow shock will stand on strong ground, since it would enable us to rule out processes interior to the magnetosphere as the cause of variations in the current on open field lines.

The results of these studies would be significant steps forward in filling the knowledge gap regarding this understudied yet very important part of the

geospace system. On the observational side, ongoing work in the UTA physics group, the preliminary results of which were recently presented at the 2022 AGU Fall Meeting, has found from a statistical study of MMS magnetosheath observations that under low Mach number and southward IMF, the majority of the magnetosheath current has Region 1 polarity. This result supports the findings of Lopez et al. (2011) which presented evidence, also using MHD simulations, that the currents in the magnetosheath with Region 1 polarity are connected to the bow shock.

5.3 Conclusion

Many factors contribute to the ability of MHD models to accurately predict the location of the magnetopause. The models do well under certain solar wind drivers but fall short for others. Each model has its own strengths and weaknesses. Various avenues of investigation remain after the work presented in Chapters 2 and 3, including exploration of the many available couplings and options for running the MHD codes.

An event study has demonstrated that the bow shock current may close into the polar cap on open field lines with Region 1 polarity. The closure of the bow shock current remains an open question that is challenging to answer definitively, but groundwork studies using both observations and simulations offer a path forward.

Bibliography

Alken, P., Thébault, E., Beggan, C. D., Amit, H., Aubert, J., Baerenzung, J., Bondar, T. N., Brown, W. J., Califf, S., Chambodut, A., Chulliat, A., Cox, G. A., Finlay, C. C., Fournier, A., Gillet, N., Grayver, A., Hammer, M. D., Holschneider, M., Huder, L., … Zhou, B. (2021). International Geomagnetic Reference Field: the thirteenth generation. *Earth, Planets and Space*, *73*(1), Article 49, 49. https://doi.org/10.1186/s40623-020-01288-x

Anderson, B. J., Korth, H., Waters, C. L., Green, D. L., Merkin, V. G., Barnes, R. J., & Dyrud, L. P. (2014). Development of large-scale birkeland currents determined from the active magnetosphere and planetary electrodynamics response experiment. *Geophysical Research Letters*, *41*(9), 3017–3025. https://doi.org/https://doi.org/10.1002/2014GL059941

Anderson, B. J., Takahashi, K., Kamei, T., Waters, C. L., & Toth, B. A. (2002). Birkeland current system key parameters derived from iridium observations: Method and initial validation results. *Journal of Geophysical Research: Space Physics*, *107*(A6), SMP 11-1-SMP 11–13. https://doi.org/https://doi.org/10.1029/2001JA000080

Angelopoulos, V. (2008). The themis mission. *Space Science Reviews*, *141*(1-4), 5.

Aubry, M. P., Russell, C. T., & Kivelson, M. G. (1970). Inward motion of the magnetopause before a substorm. *Journal of Geophysical Research (1896-1977)*, *75*(34), 7018–7031. https://doi.org/https://doi.org/10.1029/JA075i034p07018

Auster, H., Glassmeier, K., Magnes, W., Aydogar, O., Baumjohann, W., Constantinescu, O., Fischer, D., Fornacon, K.-H., Georgescu, E., Harvey, P., Hillenmaier, O., Kroth, R., Ludlam, M., Narita, Y., Nakamura, R., Okrafka, K., Plaschke, F., Richter, I., Leinweber, H., & Wiedemann, M. (2008). The themis fluxgate magnetometer. *Space Science Review, v.141, 235-264 (2008)*, *141*. https://doi.org/10.1007/s11214-008-9365-9

Axford, W. I., & Hines, C. O. (1961). A unifying theory of high-latitude geophysical phenomena and geomagnetic storms. *Canadian Journal of Physics*, *39*(10), 1433–1464. https://doi.org/10.1139/p61-172

Bhattarai, S. K., Lopez, R. E., Bruntz, R., Lyon, J. G., & Wiltberger, M. (2012). Simulation of the polar cap potential during periods with northward interplanetary magnetic field. *Journal of Geophysical Research: Space Physics*, *117*(A4). https://doi.org/https://doi.org/10.1029/2011JA017143

Bonde, R. E. F., Lopez, R. E., & Wang, J. Y. (2018). The effect of imf fluctuations on the subsolar magnetopause position: A study using a global mhd model. *Journal of Geophysical Research: Space Physics*, *123*(4), 2598–2604. https://doi.org/10.1002/2018JA025203

Borovsky, J. E. (2008). Flux tube texture of the solar wind: Strands of the magnetic carpet at 1 au? *Journal of Geophysical Research: Space Physics*, *113*(A8). https://doi.org/https://doi.org/10.1029/2007JA012684

Burch, J. L., Moore, T. E., Torbert, R. B., & Giles, B. L. (2016). Magnetospheric Multiscale Overview and Science Objectives. *Space Science Reviews*, *199*(1-4), 5–21. https://doi.org/10.1007/s11214-015-0164-9

Cramer, W., Raeder, J., Toffoletto, F., Gilson, M., & Hu, B. (2017). Plasma sheet injections into the inner magnetosphere: Two-way coupled openggcm-rcm model results: Openggcm-rcm plasma sheet injections. *Journal of Geophysical Research: Space Physics*, *122*. https://doi.org/10.1002/2017JA024104

Crooker, N. U. (1992). Reverse convection. *Journal of Geophysical Research: Space Physics*, *97*(A12), 19363–19372. https://doi.org/https://doi.org/10.1029/92JA01532

Dickinson, R. E., Ridley, E. C., & Roble, R. G. (1981). A three-dimensional general circulation model of the thermosphere. *Journal of Geophysical Research: Space Physics*, *86*(A3), 1499–1512. https://doi.org/https://doi.org/10.1029/JA086iA03p01499

Dmitriev, A., Suvorova, A., & Chao, J. (2011). A predictive model of geosynchronous magnetopause crossings. *Journal of Geophysical Research: Space Physics*, *116*. https://doi.org/10.1029/2010JA016208

Dredger, P. M., Lopez, R. E., & Hamrin, M. (2023). A case study in support of closure of bow shock current through the ionosphere utilizing multi-point observations and simulation. *Frontiers in Astronomy and Space Sciences*, *10*. https://doi.org/10.3389/fspas.2023.1098388

Dungey, J. W. (1961). Interplanetary magnetic field and the auroral zones. *Physical Review Letters*, *6*(2), 47.

Dunlop, M. W., Dong, X.-C., Wang, T.-Y., Eastwood, J. P., Robert, P., Haaland, S., Yang, Y.-Y., Escoubet, P., Rong, Z.-J., Shen, C., Fu, H.-S., & De Keyser, J. (2021). Curlometer technique and applications [e2021JA029538 2021JA029538]. *Journal of Geophysical Research: Space Physics*, *126*(11), e2021JA029538. https://doi.org/https://doi.org/10.1029/2021JA029538

Ebihara, Y. (2019). Simulation study of near-earth space disturbances: 1. magnetic storms. *Progress in Earth and Planetary Science*, *6*(16). https://doi.org/https://doi.org/10.1186/s40645-019-0264-3

Fedder, J. A., Slinker, S. P., Lyon, J. G., Russell, C. T., Fenrich, F. R., & Luhmann, J. G. (1997). A first comparison of polar magnetic field measurements and magnetohydrodynamic simulation results for field-aligned currents. *Geophysical Research Letters*, *24*(20), 2491–2494. https://doi.org/https://doi-org.cuucar.idm.oclc.org/10.1029/97GL02608

Fedder, J. A., Lyon, J. G., Slinker, S. P., & Mobarry, C. (1995). Topological structure of the magnetotail as a function of interplanetary magnetic field direction. *Journal of Geophysical Research: Space Physics*, *100*(A3), 3613–3621.

Fok, M.-C., Wolf, R., Spiro, R., & Moore, T. (2001). Comprehensive computational model of earth's ring current. *Journal of Geophysical Research: Space Physics*, *106*(A5), 8417–8424.

Fok, M.-C. (2020). Cross-regional coupling. In *Ring current investigations* (pp. 225–244). Elsevier.

Ganushkina, N. Y., Liemohn, M., & Dubyagin, S. (2018). Current systems in the earth's magnetosphere. *Reviews of Geophysics*, *56*(2), 309–332.

Ganushkina, N. Y., Liemohn, M. W., Dubyagin, S., Daglis, I., Dandouras, I., De Zeeuw, D., Ebihara, Y., Ilie, R., Katus, R., Kubyshkina, M., et al. (2015). Defining and resolving current systems in geospace. *Annales Geophysicae*, *33*(11), 1369–1402.

Guo, X. C., Wang, C., Hu, Y. Q., & Kan, J. R. (2008). Bow shock contributions to region 1 field-aligned current: A new result from global mhd simulations. *Geophysical Research Letters*, *35*(3). https://doi.org/10.1029/2007GL032713

Hamrin, M., Gunell, H., Lindkvist, J., Lindqvist, P.-A., Ergun, R. E., & Giles, B. L. (2018). Bow shock generator current systems: Mms observations of possible current closure. *Journal of Geophysical Research: Space Physics*, *123*(1), 242–258. https://doi.org/10.1002/2017JA024826

Heppner, J., & Maynard, N. (1987). Empirical high-latitude electric field models. *Journal of Geophysical Research: Space Physics*, *92*(A5), 4467–4489.

Hogan, B., Lotko, W., & Pham, K. (2020). Alfvénic thermospheric upwelling in a global geospace model [e2020JA028059 2020JA028059]. *Journal of Geophysical Research: Space Physics*, *125*(12), e2020JA028059. https://doi.org/https://doi.org/10.1029/2020JA028059

Hughes, W. (1995). The magnetopause, magnetotail and magnetic reconnection. *Introduction to space physics*, 227–287.

Hundhausen, A. (1968). Direct observations of solar-wind particles. *Space Science Reviews*, *8*(5-6), 690–749.

Janhunen, P., Palmroth, M., Laitinen, T., Honkonen, I., Juusola, L., Facsko, G., & Pulkkinen, T. (2012). The gumics-4 global mhd magnetosphere-ionosphere

coupling simulation. *Journal of Atmospheric and Solar - Terrestrial Physics*, *80*, 48–59. https://doi.org/10.1016/j.jastp.2012.03.006

Kang, S.-B., Fok, M.-C., Komar, C., Glocer, A., Li, W., & Buzulukova, N. (2018). An energetic electron flux dropout due to magnetopause shadowing on 1 june 2013. *Journal of Geophysical Research: Space Physics*, *123*(2), 1178–1190. https://doi.org/https://doi.org/10.1002/2017JA024879

Kivelson, M. G., & Russell, C. T. (1995). Introduction to space physics. *Introduction to Space Physics*, 586.

Knipp, D., Kilcommons, L., Hairston, M., & Coley, W. R. (2021). Hemispheric asymmetries in poynting flux derived from dmsp spacecraft. *Geophysical Research Letters*, *48*(17), e2021GL094781.

Lepping, R. P., Acũna, M. H., Burlaga, L. F., Farrell, W. M., Slavin, J. A., Schatten, K. H., Mariani, F., Ness, N. F., Neubauer, F. M., Whang, Y. C., Byrnes, J. B., Kennon, R. S., Panetta, P. V., Scheifele, J., & Worley, E. M. (1995). The Wind Magnetic Field Investigation. *Space Science Reviews*, *71*(1-4), 207–229. https://doi.org/10.1007/BF00751330

Li, W., Raeder, J., Dorelli, J., Øieroset, M., & Phan, T. D. (2005). Plasma sheet formation during long period of northward imf. *Geophysical Research Letters*, *32*(12). https://doi.org/https://doi.org/10.1029/2004GL021524

Liemohn, M. W., Ridley, A. J., Gallagher, D. L., Ober, D. M., & Kozyra, J. U. (2004). Dependence of plasmaspheric morphology on the electric field description during the recovery phase of the 17 april 2002 magnetic storm. *Journal of Geophysical Research: Space Physics*, *109*(A3).

Liu, J., Wang, W., Qian, L., Lotko, W., Burns, A. G., Pham, K., Lu, G., Solomon, S. C., Liu, L., Wan, W., Anderson, B. J., Coster, A., & Wilder, F. (2021). Solar flare effects in the Earth's magnetosphere. *Nature Physics*, *17*(7), 807–812. https://doi.org/10.1038/s41567-021-01203-5

Lopez, R. E. (2018). The bow shock current system. In *Electric currents in geospace and beyond* (pp. 477–496). American Geophysical Union (AGU). https://doi.org/https://doi.org/10.1002/9781119324522.ch28

Lopez, R. E., Bruntz, R., Mitchell, E. J., Wiltberger, M., Lyon, J. G., & Merkin, V. G. (2010). Role of magnetosheath force balance in regulating the dayside reconnection potential. *Journal of Geophysical Research: Space Physics*, *115*(A12). https://doi.org/10.1029/2009JA014597

Lopez, R. E., & Gonzalez, W. D. (2017). Magnetospheric balance of solar wind dynamic pressure. *Geophysical Research Letters*, *44*(7), 2991–2999. https://doi.org/10.1002/2017GL072817

Lopez, R. E., Hernandez, S., Wiltberger, M., Huang, C. .-., Kepko, E. L., Spence, H., Goodrich, C. C., & Lyon, J. G. (2007). Predicting magnetopause crossings at geosynchronous orbit during the Halloween storms. *Space Weather*, *5*(1), Article 01005, 01005. https://doi.org/10.1029/2006SW000222

Lopez, R. E., Merkin, V. G., & Lyon, J. G. (2011). The role of the bow shock in solar wind-magnetosphere coupling. *Annales Geophysicae*, *29*(6), 1129–1135. https://doi.org/10.5194/angeo-29-1129-2011

Lyon, J., Fedder, J., & Mobarry, C. (2004). The lyon-fedder-mobarry (lfm) global mhd magnetosphere simulation code. *Journal of Atmospheric and Solar-Terrestrial Physics*, *66*, 1333–1350. https://doi.org/10.1016/j.jastp.2004.03.020

Maltsev, Y. P., Arykov, A. A., Belova, E. G., Gvozdevsky, B. B., & Safargaleev, V. V. (1996). Magnetic flux redistribution in the storm time magnetosphere. *Journal of Geophysical Research: Space Physics*, *101*(A4), 7697–7704. https://doi.org/https://doi.org/10.1029/95JA03709

Maltsev, Y. P., & Lyatsky, W. B. (1975). Field-aligned currents and erosion of the dayside magnetosphere. *Planetary and Space Science*, *23*, 1257–1260.

Martyn, D. F. (1951). The theory of magnetic storms and auroras. *Nature*, *167*, 92–94.

McComas, D. J., Bame, S. J., Barker, P., Feldman, W. C., Phillips, J. L., Riley, P., & Griffee, J. (1998). Solar Wind Electron Proton Alpha Monitor (SWEPAM) for the Advanced Composition Explorer. *Space Science Reviews*, *86*, 563–612. https://doi.org/10.1023/A:1005040232597

McFadden, J., Carlson, C., Larson, D., Ludlam, M., Abiad, R., Elliott, B., Turin, P., Marckwordt, M., & Angelopoulos, V. (2008). The themis esa plasma instrument and in-flight calibration. *Space Science Reviews*, *141*, 277–302. https://doi.org/10.1007/s11214-008-9440-2

Merkin, V. G., Anderson, B. J., Lyon, J. G., Korth, H., Wiltberger, M., & Motoba, T. (2013). Global evolution of Birkeland currents on 10 min timescales: MHD simulations and observations. *Journal of Geophysical Research (Space Physics)*, *118*(8), 4977–4997. https://doi.org/10.1002/jgra.50466

Merkin, V. G., & Lyon, J. G. (2010). Effects of the low-latitude ionospheric boundary condition on the global magnetosphere. *Journal of Geophysical Research: Space Physics*, *115*(A10). https://doi.org/https://doi.org/10.1029/2010JA015461

Moore, T. E., Fok, M.-C., Chandler, M. O., Chappell, C. R., Christon, S. P., Delcourt, D. C., Fedder, J., Huddleston, M., Liemohn, M., Peterson, W. K., & Slinker, S. (2005). Plasma sheet and (nonstorm) ring current formation from solar and polar wind sources. *Journal of Geophysical Research: Space Physics*, *110*(A2). https://doi.org/https://doi.org/10.1029/2004JA010563

Mukhopadhyay, A., Welling, D., Liemohn, M., Ridley, A., Burleigh, M., Wu, C., Zou, S., Connor, H., Vandegriff, E., Dredger, P., et al. (2022). Global driving of auroral precipitation: 1. balance of sources. *Journal of Geophysical Research: Space Physics*, *127*(7), e2022JA030323.

Mukhopadhyay, A., Welling, D. T., Liemohn, M. W., Ridley, A. J., Chakraborty, S., & Anderson, B. J. (2020). Conductance model for extreme events: Impact of auroral conductance on space weather forecasts [e2020SW002551 10.1029/2020SW002551]. *Space Weather*, *18*(11), e2020SW002551. https://doi.org/https://doi.org/10.1029/2020SW002551

NASA CDAWeb Development Team. (2019). CDAWeb: Coordinated Data Analysis Web.

Newell, P. T., Lyons, K. M., & Meng, C.-I. (1996). A large survey of electron acceleration events. *Journal of Geophysical Research: Space Physics*, *101*(A2), 2599–2614. https://doi.org/https://doi.org/10.1029/95JA03147

Ogilvie, K. W., Chornay, D. J., Fritzenreiter, R. J., Hunsaker, F., Keller, J., Lobell, J., Miller, G., Scudder, J. D., Sittler, J., E. C., Torbert, R. B., Bodet, D., Needell, G., Lazarus, A. J., Steinberg, J. T., Tappan, J. H., Mavretic, A., & Gergin, E. (1995). SWE, A Comprehensive Plasma Instrument for the Wind Spacecraft. *Space Science Reviews*, *71*(1-4), 55–77. https://doi.org/10.1007/BF00751326

Papitashvili, N., & King, J. (2020). Omni 1-min data [data set]. *NASA Space*, *758*.

Parker, E. (1965). Dynamical theory of the solar wind. *Space Science Reviews*, *4*(5-6), 666–708.

Parker, E. N. (1958). Dynamics of the interplanetary gas and magnetic fields. *Astrophysical Journal, vol. 128, p. 664*, *128*, 664.

Pembroke, A., Toffoletto, F., Sazykin, S., Wiltberger, M., Lyon, J., Merkin, V., & Schmitt, P. (2012). Initial results from a dynamic coupled magnetosphere-ionosphere-ring current model. *Journal of Geophysical Research: Space Physics*, *117*(A2). https://doi.org/https://doi.org/10.1029/2011JA016979

Pham, K. H., Lotko, W., Varney, R. H., Zhang, B., & Liu, J. (2021). Thermospheric impact on the magnetosphere through ionospheric outflow [e2020JA028656 2020JA028656]. *Journal of Geophysical Research: Space Physics*, *126*(2), e2020JA028656. https://doi.org/https://doi.org/10.1029/2020JA028656

Pham, K. H., Lopez, R. E., & Bruntz, R. (2016). The effect of a brief northward turning in imf bz on solar wind-magnetosphere coupling in a global mhd simulation. *Journal of Geophysical Research: Space Physics*, *121*(5), 4291–4299. https://doi.org/https://doi.org/10.1002/2015JA021982

Pollock, C., Moore, T., Jacques, A., Burch, J., Gliese, U., Saito, Y., Omoto, T., Avanov, L., Barrie, A., Coffey, V., Dorelli, J., Gershman, D., Giles, B., Rosnack, T., Salo, C., Yokota, S., Adrian, M., Aoustin, C., Auletti, C., ... Zeuch, M. (2016). Fast Plasma Investigation for Magnetospheric Multiscale. *Space Science Reviews*, *199*(1-4), 331–406. https://doi.org/10.1007/s11214-016-0245-4

Powell, K. G., Roe, P. L., Linde, T. J., Gombosi, T. I., & De Zeeuw, D. L. (1999). A solution-adaptive upwind scheme for ideal magnetohydrodynamics. *Journal of Computational Physics*, *154*(2), 284–309. https://doi.org/https://doi.org/10.1006/jcph.1999.6299

Qian, L., Burns, A. G., Emery, B. A., Foster, B., Lu, G., Maute, A., Richmond, A. D., Roble, R. G., Solomon, S. C., & Wang, W. (2014). The ncar tie-gcm. In *Modeling the ionosphere–thermosphere system* (pp. 73–83). American Geophysical Union (AGU). https://doi.org/https://doi.org/10.1002/9781118704417.ch7

Raeder, J., Larson, D., Li, W., Kepko, E. L., & Fuller-Rowell, T. (2008). Openggcm simulations for the themis mission. *Space Science Reviews*, *141*(1), 535–555.

Raeder, J., Larson, D., Li, W., Kepko, E. L., & Fuller-Rowell, T. (2009). Openggcm simulations for the themis mission. *The THEMIS Mission*, 535–555.

Raeder, J., McPherron, R., Frank, L., Kokubun, S., Lu, G., Mukai, T., Paterson, W., Sigwarth, J., Singer, H., & Slavin, J. (2001). Global simulation of the geospace environment modeling substorm challenge event. *Journal of Geophysical Research: Space Physics*, *106*(A1), 381–395.

Redmann, J. (1985). An overview of the mission sensor systems of the dmsp satellites. *23rd Aerospace Sciences Meeting*, 240.

Ridley, A., Gombosi, T., & Dezeeuw, D. (2004). Ionospheric control of the magnetosphere: conductance. *Annales Geophysicae*, *22*(2), 567–584. https://doi.org/10.5194/angeo-22-567-2004

Ridley, A. J., De Zeeuw, D. L., Gombosi, T. I., & Powell, K. G. (2001). Using steady state mhd results to predict the global state of the magnetosphere-ionosphere system. *Journal of Geophysical Research: Space Physics*, *106*(A12), 30067–30076. https://doi.org/https://doi.org/10.1029/2000JA002233

Ridley, A. J., & Liemohn, M. W. (2002). A model-derived storm time asymmetric ring current driven electric field description. *Journal of Geophysical Research: Space Physics*, *107*(A8), SMP 2-1-SMP 2–12. https://doi.org/https://doi.org/10.1029/2001JA000051

Roble, R. G., Ridley, E. C., Richmond, A. D., & Dickinson, R. E. (1988). A coupled thermosphere/ionosphere general circulation model. *Geophysical Research Letters*, *15*(12), 1325–1328. https://doi.org/https://doi.org/10.1029/GL015i012p01325

Rufenach, C. L., Martin Jr, R., & Sauer, H. (1989). A study of geosynchronous magnetopause crossings. *Journal of Geophysical Research: Space Physics*, *94*(A11), 15125–15134.

Russell, C., Anderson, B., Baumjohann, W., Bromund, K., Dearborn, D., Fischer, D., Le, G., Leinweber, H., Leneman, D., Magnes, W., et al. (2016). The magnetospheric multiscale magnetometers. *Space Science Reviews*, *199*, 189–256.

Shou, Y., Tenishev, V., Chen, Y., Toth, G., & Ganushkina, N. (2021). Magneto-hydrodynamic with adaptively embedded particle-in-cell model: Mhd-aepic. *Journal of Computational Physics*, *446*, 110656. https://doi.org/https://doi.org/10.1016/j.jcp.2021.110656

Sibeck, D. G., Lopez, R. E., & Roelof, E. C. (1991). Solar wind control of the magnetopause shape, location, and motion. *Journal of Geophysical Research*, *96*(A4), 5489–5495. https://doi.org/10.1029/90JA02464

Sibeck, D. G. (1995). Demarcating the magnetopause boundary. *Reviews of Geophysics*, *33*(S1), 651–655.

Siebert, K. D., & Siscoe, G. L. (2002). Dynamo circuits for magnetopause reconnection. *Journal of Geophysical Research: Space Physics*, *107*(A7), SMP 6-1-SMP 6–5. https://doi.org/10.1029/2001JA000237

Siscoe, G. L., Crooker, N. U., & Siebert, K. D. (2002). Transpolar potential saturation: Roles of region 1 current system and solar wind ram pressure. *Journal of Geophysical Research: Space Physics*, *107*(A10), SMP 21-1-SMP 21–8. https://doi.org/10.1029/2001JA009176

Smith, C. W., L'Heureux, J., Ness, N. F., Acuña, M. H., Burlaga, L. F., & Scheifele, J. (1998). The ACE Magnetic Fields Experiment. *Space Science Reviews*, *86*, 613–632. https://doi.org/10.1023/A:1005092216668

Smith, M. F., & Lockwood, M. (1996). Earth's magnetospheric cusps. *Reviews of Geophysics*, *34*(2), 233–260. https://doi.org/https://doi.org/10.1029/96RG00893

Song, P., Gombosi, T., DeZeeuw, D., Powell, K., & Groth, C. (2000). A model of solar wind–magnetosphere–ionosphere coupling for due northward

imf. *Planetary and Space Science*, *48*(1), 29–39. https://doi.org/https://doi.org/10.1016/S0032-0633(99)00065-3

Spreiter, J. R., Summers, A. L., & Alksne, A. Y. (1966). Hydromagnetic flow around the magnetosphere. *Planetary and Space Science*, *14*(3), 223–253.

Sugiura, M. (1963). *Hourly values of equatorial dst for the igy* (tech. rep.).

Tang, B. B., Guo, X. C., Wang, C., Hu, Y. Q., & Kan, J. R. (2009). Bow shock and magnetopause contributions to the cross-tail current from global mhd simulations. *Journal of Geophysical Research: Space Physics*, *114*(A8). https://doi.org/10.1029/2009JA014325

Tang, B. B., Wang, C., & Guo, X. C. (2012). Bow shock and magnetopause contributions to the magnetospheric current system: Hints from the cluster observations. *Journal of Geophysical Research: Space Physics*, *117*(A1). https://doi.org/https://doi.org/10.1029/2011JA016681

Toffoletto, F., Sazykin, S., Spiro, R., & Wolf, R. (2003). Inner magnetospheric modeling with the rice convection model. *Space Science Reviews*, *107*, 175–196. https://doi.org/10.1023/A:1025532008047

Torbert, R. B., Russell, C. T., Magnes, W., Ergun, R. E., Lindqvist, P. .-., Le Contel, O., Vaith, H., Macri, J., Myers, S., Rau, D., Needell, J., King, B., Granoff, M., Chutter, M., Dors, I., Olsson, G., Khotyaintsev, Y. V., Eriksson, A., Kletzing, C. A., … Lappalainen, K. (2016). The FIELDS Instrument Suite on MMS: Scientific Objectives, Measurements, and Data Products. *Space Science Reviews*, *199*(1-4), 105–135. https://doi.org/10.1007/s11214-014-0109-8

Tóth, G. (2000). The $\nabla\cdot$ b= 0 constraint in shock-capturing magnetohydrodynamics codes. *Journal of Computational Physics*, *161*(2), 605–652.

Tóth, G., Sokolov, I. V., Gombosi, T. I., Chesney, D. R., Clauer, C. R., De Zeeuw, D. L., Hansen, K. C., Kane, K. J., Manchester, W. B., Oehmke, R. C., Powell, K. G., Ridley, A. J., Roussev, I. I., Stout, Q. F., Volberg, O., Wolf, R. A., Sazykin, S., Chan, A., Yu, B., & Kóta, J. (2005). Space weather modeling framework: A new tool for the space science community. *Journal of Geophysical Research: Space Physics*, *110*(A12). https://doi.org/https://doi.org/10.1029/2005JA011126

Tóth, G., van der Holst, B., Sokolov, I. V., De Zeeuw, D. L., Gombosi, T. I., Fang, F., Manchester, W. B., Meng, X., Najib, D., Powell, K. G., Stout, Q. F., Glocer, A., Ma, Y.-J., & Opher, M. (2012). Adaptive numerical algorithms in space weather modeling. *Journal of Computational Physics*, *231*(3), 870–903. https://doi.org/10.1016/j.jcp.2011.02.006

Vasyliūnas, V. M. (2011). Physics of magnetospheric variability. *Space science reviews*, *158*, 91–118.

Wang, W., Wiltberger, M., Burns, A., Solomon, S., Killeen, T., Maruyama, N., & Lyon, J. (2004). Initial results from the coupled magnetosphere–ionosphere–thermosphere model: Thermosphere–ionosphere responses [Towards an Integrated Model of the Space Weather System]. *Journal of Atmospheric and Solar-Terrestrial Physics*, *66*(15), 1425–1441. https://doi.org/https://doi.org/10.1016/j.jastp.2004.04.008

Welling, D. (2019). Magnetohydrodynamic models of b and their use in gic estimates. *Geomagnetically induced currents from the sun to the power grid*, 43–65.

Wiltberger, M., Lopez, R., & Lyon, J. (2003). Magnetopause erosion: A global view from mhd simulation. *Journal of Geophysical Research: Space Physics*, *108*(A6).

Wiltberger, M., Lotko, W., Lyon, J. G., Damiano, P., & Merkin, V. (2010). Influence of cusp o+ outflow on magnetotail dynamics in a multifluid mhd model of the magnetosphere. *Journal of Geophysical Research: Space Physics*, *115*(A10). https://doi.org/https://doi.org/10.1029/2010JA015579

Wiltberger, M., Qian, L., Huang, C.-L., Wang, W., Lopez, R. E., Burns, A. G., Solomon, S. C., Deng, Y., & Huang, Y. (2012). Cmit study of cr2060 and 2068 comparing l1 and mas solar wind drivers [Corotating Interaction Regions from Sun to Earth: Modeling their formation, evolution and geoeffectiveness]. *Journal of Atmospheric and Solar-Terrestrial Physics*, *83*, 39–50. https://doi.org/https://doi.org/10.1016/j.jastp.2012.01.005

Wiltberger, M., Wang, W., Burns, A., Solomon, S., Lyon, J., & Goodrich, C. (2004). Initial results from the coupled magnetosphere ionosphere thermosphere model: Magnetospheric and ionospheric responses [Towards an Integrated Model of the Space Weather System]. *Journal of Atmospheric and Solar-Terrestrial Physics*, *66*(15), 1411–1423. https://doi.org/https://doi.org/10.1016/j.jastp.2004.03.026

Wiltberger, M., Weigel, R. S., Lotko, W., & Fedder, J. A. (2009). Modeling seasonal variations of auroral particle precipitation in a global-scale magnetosphere-ionosphere simulation. *Journal of Geophysical Research: Space Physics*, *114*(A1). https://doi.org/https://doi.org/10.1029/2008JA013108

Wolf, R. A., Harel, M., Spiro, R. W., Voigt, G.-H., Reiff, P. H., & Chen, C.-K. (1982). Computer simulation of inner magnetospheric dynamics for the magnetic storm of july 29, 1977. *Journal of Geophysical Research: Space Physics*, *87*(A8), 5949–5962. https://doi.org/https://doi.org/10.1029/JA087iA08p05949

Zeeuw, D., Sazykin, S., Wolf, R., Gombosi, T., Ridley, A., & Toth, G. (2004). Coupling of a global mhd code and an inner magnetosphere model: Initial results. *Journal of Geophysical Research: Space Physics*, *109*. https://doi.org/10.1029/2003JA010366

Zhang, B., Sorathia, K. A., Lyon, J. G., Merkin, V. G., Garretson, J. S., & Wiltberger, M. (2019). Gamera: A three-dimensional finite-volume mhd solver for non-orthogonal curvilinear geometries. *The Astrophysical Journal Supplement Series*, *244*(1), 20.